Computational modelling of what matters for uterine vascular network function

Stephanie Leighton

Supervised by

Alys Clark

Jo James

A thesis submitted in fulfilment of the requirements for the degree of Master of Engineering in Bioengineering, the University of Auckland, 2022.

Table of Contents

Table of Figures

Table of Tables

Abstract

During pregnancy, maternal uterine vasculature adapts to supply the developing fetus with sufficient oxygen and nutrients for growth. In pregnancy conditions such as FGR and preeclampsia, the system is unable to make the necessary changes, leading to adverse health conditions for both the mother and the growing baby. During pregnancy, the vessels outwardly remodel reducing system resistance (along with an increase in maternal cardiac output), allowing for increased flow and the vascular reactivity behaviour of uterine vessels adapts. Detecting these vascular changes is difficult using Doppler ultrasound, with waveforms being a clinical indicator of downstream resistance. Additionally, animal models such as rats can inform the understanding of human physiology. Computational modelling was implemented in this study to link anatomical observations to physiological function.

Firstly, static models spanning the first half of pregnancy were improved with novel anatomical data for vessel geometries and plug characteristics. The transformation of the uterine vasculature is dependent on placentation because placental trophoblast cells invade the spiral arteries (feed blood to the placenta) initially forming plugs to flow and transforming these vessels into funnels. The degradation of trophoblast plugs was considered with the inclusion of flow descriptions through clear channels with porous surrounds. A sensitivity analysis quantified the impact of individual parameters on the overall network function. The channels as modelled here supports that they are the dominant pathway for flow and the porous surrounds act as bottlenecks. Plugs reduce shear conditions in the upstream radial and arcuate arteries, while the uterine artery only depend on vessel lumen.

Secondly, models of vascular reactivity (passive, active and shear responses) derived for rat radial arteries were parameterised for human vessels and incorporated into network models of uterine circulation at the radial artery levels (identified as key modulators of flow). Pregnancy adapts radial vessels to tolerate a higher flow rate before constricting, which is important for maintaining blood flow through to the placenta. In the network models, the passive response follows the trend of increasing vessel diameter with increasing pressure. When the active response is added, the myogenic response adds a constriction response, dampening the passive increase in diameter.

Acknowledgements

I would like to express my immense thanks to my supervisors Dr Alys Clark and Dr Jo James for all their help over the course of this project. Their generosity of time, insightful ideas and deep knowledge of their field has been inspiring. I have learnt so much from you both. Your support and encouragement truly helped to get this project completed.

I would like to extend my appreciation for Dr Hanna Allerkamp for her willingness to share her knowledge and be a source of inspiration. I have been fortunate to be a part of the female reproduction team at ABI. Our weekly team meetings and comradery have been a great support.

Finally, to my family and friends who have continued to support me in all my endeavours. To my dearest sister, Natasha, thank you for being my rock. Dad, thank you for always encouraging me. And lastly to my late Mother who passed away earlier this year, you mean the world to me. I know you would have been proud.

Chapter 1 – Motivation

Over the course of a pregnancy, the developing fetus only has access to oxygen and the nutrients required for growth through the utero-placental circulatory system. The complex network of blood vessels in the uterus transforms to accommodate a 15-fold increase in flow over the course of pregnancy. This transformation results from local and systemic endocrine, paracrine, and haemodynamic changes that enable a steady supply of oxygenated blood to be delivered to the placenta and thus the growing baby. A well-functioning utero-placental circulatory system is vital for pregnancy success, but this dynamic process is difficult to study in human pregnancies (James, Whitley, and Cartwright 2011; James, Chamley, and Clark 2017).

In some pregnancies, the maternal vasculature is unable to complete the necessary changes. This results in placental insufficiency which impairs exchange and adversely affects fetal growth. Fetal growth restriction (FGR) is defined as an infant with a birth weight in the bottom 3rd percentile (Gordijn et al. 2016). In cases of FGR, the fetus is unable to reach its full growth potential in utero, leading to postnatal consequences, as well as increased risk of adverse health conditions later in life. Importantly, FGR contributes to 28-45% of stillbirths (McCowan, Figueras, and Anderson 2018). However, if identified before birth, intervention can reduce the mortality rate 4 to 5-fold (McCowan, Figueras, and Anderson 2018). Pre-eclampsia is a maternal hypertensive disorder that is often associated with FGR pregnancies. It is one of the leading causes of maternal and perinatal morbidity worldwide (World Health Organization 2011). The condition is closely linked to FGR, with similar mechanistic pathways (more closely associated with the maternal factors) and often occurring together.

Although detection and monitoring of FGR is known to improve pregnancy outcomes, the current clinical methods for detecting placental insufficiency and FGR in pregnancies are not reliable, with an estimated 50% of cases being missed prior to birth (McCowan, Figueras, and Anderson 2018; Malhotra et al. 2019). The most common measurement of the growth of a fetus is by taking a fundal height measurement. Less frequently (typically twice during pregnancy in New Zealand) ultrasound imaging is used to measure the size of the growing fetus. However, these growth scans are prone to over-estimate fetal weight (Milner and Arezina 2018). Doppler ultrasound (of the fetal umbilical artery or the maternal uterine artery) is typically used when a pregnancy is considered at risk (Williams et al. 2018). Uterine artery (UtA) Doppler ultrasound provides an indication of the downstream vascular resistance (as a proxy for placental health). Techniques used in other areas of medicine for more detailed medical imaging (e.g. computed tomography) are not suitable for application in pregnancy due to the potentially damaging effects of radiation to the developing fetus (James, Chamley, and Clark 2017). Magnetic resonance imaging (MRI) can be used to estimate fetal weight and assess placental function by measuring oxygenation levels (Sørensen et al. 2013). However, it has a high associated cost and is not yet proven to be effective as a clinical tool for detecting problems such as FGR.

The contribution of the maternal uterine circulation to the health of a pregnancy is difficult to assess. This is because the transformation of the uterine vasculature happens over a relatively short time and is inaccessible to direct measurement due to the small size of the vessels downstream of the main uterine artery. Recent studies have improved the understanding of the evolution of anatomy in human uterine circulation in early pregnancy (Allerkamp et al. 2021) but understanding of the functional impact of the uterine vascular transformation is still incomplete. Animal models (most commonly rodents) can help to inform the understanding of maternal adaptations during pregnancy. Rat reproductive anatomy shares some important commonalities with human, including haemochorial placentation, trophoblast invasion, and an outward hypertrophic pattern of remodelling of the larger uterine vessels (radial, arcuate and uterine arteries) (Osol, Ko, and Mandalà 2019; Allerkamp et al. 2021).

Computational modelling is a useful technique for relating how anatomical changes within a system impact on its function. This type of modelling can also provide a link between animal data and how that translates to a human system. Computational modelling techniques can be used to investigate the uterine vasculature and the impacts pregnancy has on how this system remodels. Previous computational models of the uterine circulation have considered how the overall resistance of the system influences uterine hemodynamics, and how this impact is observed at the uterine artery (UtA) Doppler waveforms, a common clinical measurement. In early work modelling this circulation, components of uterine vasculature were lumped together, with the main resistance load within this presumed to arise from the terminal spiral arteries (Mo et al. 1988). More recently, improved anatomical parameterisation of models with the critical inclusion of arterio-venous (AV)-anastomoses which provide a parallel pathway for flow, as well as distinct modelling components for each level of the uterine vascular tree, highlighted the radial arteries as key rate limiters of flow with the ability to significantly impact UtA Doppler waveforms (Clark, Alys et al. 2018). This provided the impetus for further anatomical focus on the radial (rather than spiral) arteries, and prompted work to improve quantification of the structural changes in these vessels across pregnancy (Allerkamp et al. 2021, 571). Further research has improved the understanding of how radial arteries functionally adapt to pregnancy in terms of vasoreactivity (Allerkamp et al. 2022). However, these improved anatomical and functional understandings are yet to be incorporated into computational models to determine the interplay between structure and vascular function.

This thesis aims to build on existing computational models describing the adaptation of the uterine circulation over the course of the pregnancy by incorporating novel anatomical data of uterine vascular structure and vascular reactivity of pregnant radial arteries.

Chapter 2 – Literature Review

To construct a computational model of the uterine vasculature, the basic anatomy and function of the uterus needs to be understood, as well as the impact pregnancy and the remodelling process have on the uterine blood vessels (and flow within them). This chapter summarises the current understanding of the uterine vasculature in pregnancy and differences in pregnancy between humans and rodents.

2.1 Human Uterine Structure- the basics

The uterus houses the fetus during pregnancy. The human uterus consists of different layers (see Figure 1), the outermost layer being the muscular myometrium, adjacent to which the endometrium forms the inner layer of the uterus. The endometrium itself is considered to have two layers: a basal layer that is located at the boundary with the myometrium that is retained following menstruation, and the functional endometrium closer to the uterine lumen that grows over the course of the menstrual cycle to support potential growth of a fertilised egg but is shed during menstruation if implantation does not occur (James, Chamley, and Clark 2017). During pregnancy, extensive remodelling of the uterine vasculature also occurs. The vessels in the endometrium (the spiral arteries) are predominantly reshaped by invading trophoblasts (placental cells) into wide funnels, and the larger vessels in the myometrium outwardly remodel in response to local and systemic signals (James, Chamley, and Clark 2017).

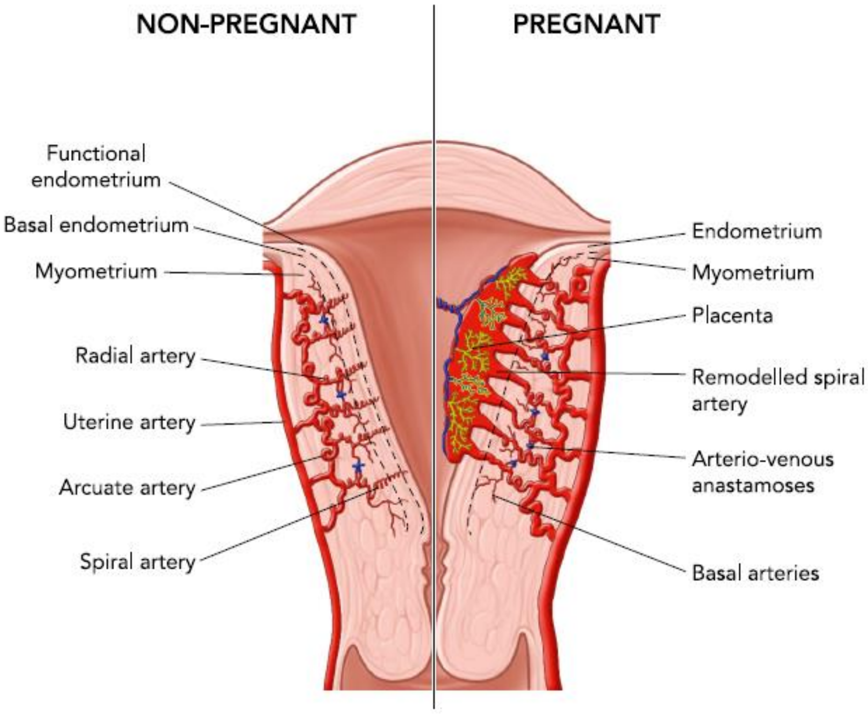

Figure 1: Reproduced from (James, Chamley, and Clark 2017). Basic uterine anatomy, a cross section showing organ shape, the tissue layers, and vascular levels. The left side shows the vessels in a non-pregnant state from the uterine artery, down to the spiral arteries. In contrast to the right, in a pregnant state, with the addition of the placenta, remodelled spiral arteries and an enlargement to upstream arteries.

2.1.1 Uterine Vessel Network

The uterine circulatory system is made up of a network of branching blood vessels which work to deliver blood to feed the uterus. During pregnancy, the uterine circulation additionally delivers blood to the surface of the placenta. The uterine vascular network can be broken down into different vessel levels, each level contributing to overall system function (Figure 2). The network begins with the uterine arteries, which branch bilaterally from the internal iliac arteries, and then run along either side of the uterus. Uterine arteries are the largest arteries in the maternal uterine circulation. Their function is to feed blood into the uterine network. A flow profile is measured here for UtA Doppler ultrasound, and downstream resistance is inferred from this point. They are observed to double in size over the course of pregnancy (Osol, Ko, and Mandalà 2019). The arcuate arteries arise from the uterine artery and run laterally around the uterus, close to the surface. They supply blood to both the myometrium and the intervillous space via the intermediate uterine vasculature. They are also observed to increase in size with gestation (Allerkamp et al. 2021). The radial arteries branch from the arcuate arteries, and travel inward through the myometrium, towards the cavity of the uterus, and play a role in modulating blood flow. Shortly before the radial arteries reach the endometrium, they transition into spiral arteries which run to near the surface of the endometrium (Clark, Alys et al. 2018). The spiral arteries function to deliver blood to the placental surface. The placenta itself has a branched villous structure and so maternal blood flows from the spiral arteries into the space between the villous branches, termed the intervillous space. The maternal and fetal blood do not mix, rather exchange occurs across a barrier formed by the outer surface of the placenta (Clark, Alys et al. 2018; James, Chamley, and Clark 2017).

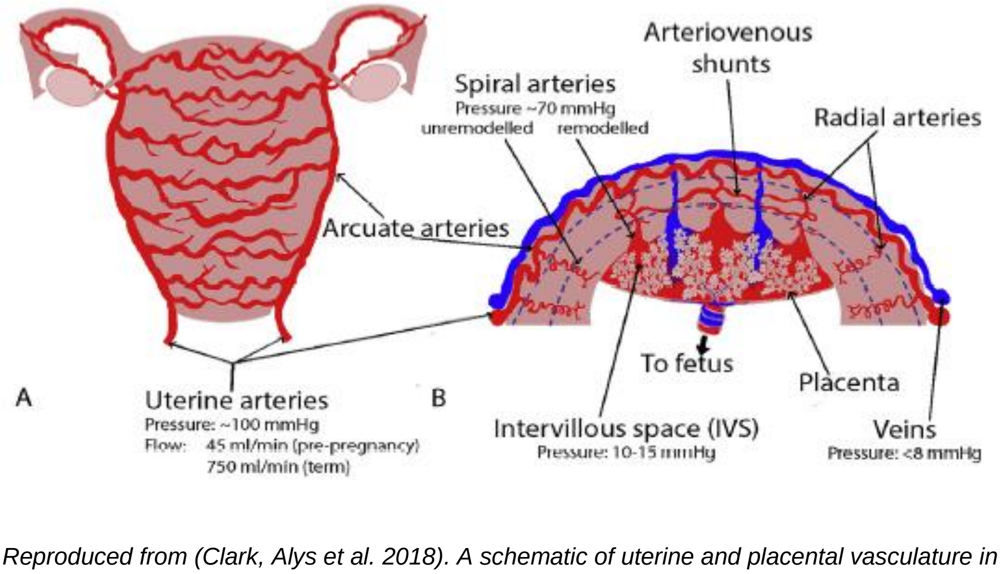

Figure 2: Reproduced from (Clark, Alys et al. 2018). A schematic of uterine and placental vasculature in pregnancy. A) Profile outline of uterus featuring uterine arteries. Arcuate arteries traversing the outer surface of the organ. B) Cross sectional view of arteries (red) and veins (blue). Arcuate arteries run across the outer surface before branching into radial arteries with AV shunts to veins at the junction with spiral arteries which feed into the IVS and placenta.

2.1.2 The Placenta

The placenta is an organ for exchange, allowing for the maternal circulation to nourish the fetus and remove fetal waste during pregnancy (Blackburn 2007). The placenta consists of an extensively branched network of fetal blood vessels that reside inside the villous trees. Trophoblast cells make up the outer epithelial layer of the placental villi, within which there is a core of mesenchymal cells containing the fetal blood vessels (Blackburn 2007) (Figure 3). The outer trophoblast layer consists of a bilayer of syncytiotrophoblasts which are a large multinucleated cell that cover the entire placental surface and is in direct contact with maternal blood for much of gestation, overlying a layer of proliferative cytotrophoblasts that drive placental growth. Finally, an invasive population of trophoblasts called extravillous trophoblasts, grow out from the tips of anchoring villi proximal to the decidua and invade into the decidual tissue where they colonise and remodel the spiral arteries first forming plugs, and then transforming them into wide funnel like vessels (Allerkamp et al. 2021). The fluid dynamics of the maternal blood flow in the intervillous space is impacted by the uterine vasculature and the placental villous structure, as well as the structure of the feto-placental vasculature. Both the maternal and fetal aspects play an important role in the efficiency of exchange (Clark, A. R. et al. 2015).

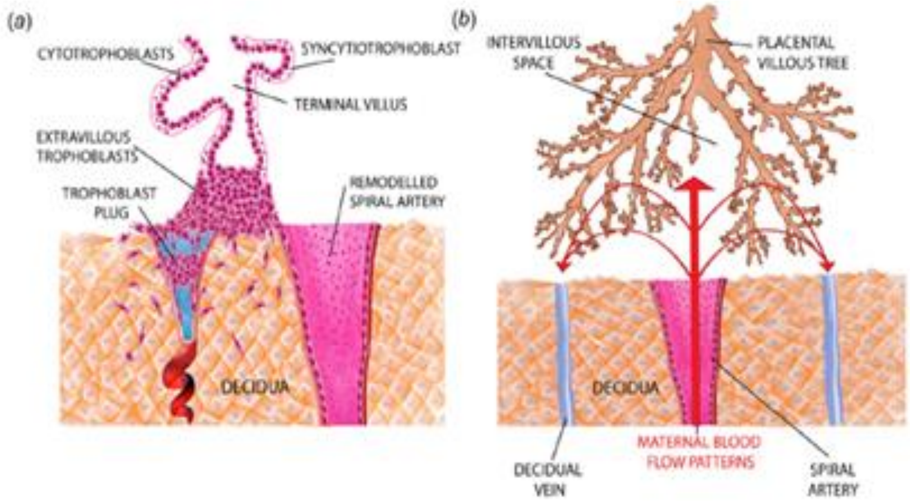

Figure 3: Reproduced from (Saghian et al. 2017). Trophoblast cell invasion remodelling maternal blood vessels. A) Spiral artery remodelling from small, tortuous vessels at the beginning or pregnancy, remodelled by extravillous trophoblast invasion to form large, funnel like openings. B) Maternal blood flow patterns in the intervillous space as a place for nutrient exchange with the placental villous tree.

2.1.3 Uterine Vessel Network Features

As in most vascular systems, the radius of the arteries in the uterus decreases the further they are down the arterial tree, at least when an individual is not pregnant. The arcuate arteries are wider, tube-like structures while the radial arteries have a degree of coiling, and the spiral arteries are even more coiled. During placentation, trophoblast cells (which originate from the placenta) invade into the uterus and first plug, and then open the spiral arteries to the surface of the placenta (more detail in Section 2.3.2). The flow velocity of the blood in the intervillous space affects the gas exchange between the maternal blood and the placenta. A slower blood flow allows for an even dispersion and sufficient time for oxygen exchange. Faster blood flow means there is a shorter transit time and less oxygen exchange. There is also the potential for damage to the villus structure (Saghian et al. 2017).

Arterio-venous (AV) anastomoses have been identified to branch out from the radial arteries around the point where they transition into spiral arteries. AV Anastomoses function to shunt blood directly between arteries and veins within the myometrium (James, Chamley, and Clark 2017). Blood that travels through the AV-anastomoses does not reach the placental surface and so does not participate in gas exchange. Schaaps et al. combined ultrasound data with casts of the uterine vasculature (following hysterectomy post-delivery due to complications) to identify the network of AV-anastomoses present in the myometrium (location of myometrium in Figure 2) (Schaaps et al. 2005). To confirm their functionality, blood gases taken at different points in the network were compared and a difference observed between the intervillous space and uterine venous blood partial oxygen pressure. They proposed a new model in which this system runs in parallel to the blood supply to the placenta. AV anastomoses are hypothesised to be protective of short periods of high pressure/flow (Schaaps et al. 2005). Extensive remodelling is observed in veins as well as the arterial network however they are rarely measured (Clark, Alys et al. 2018).

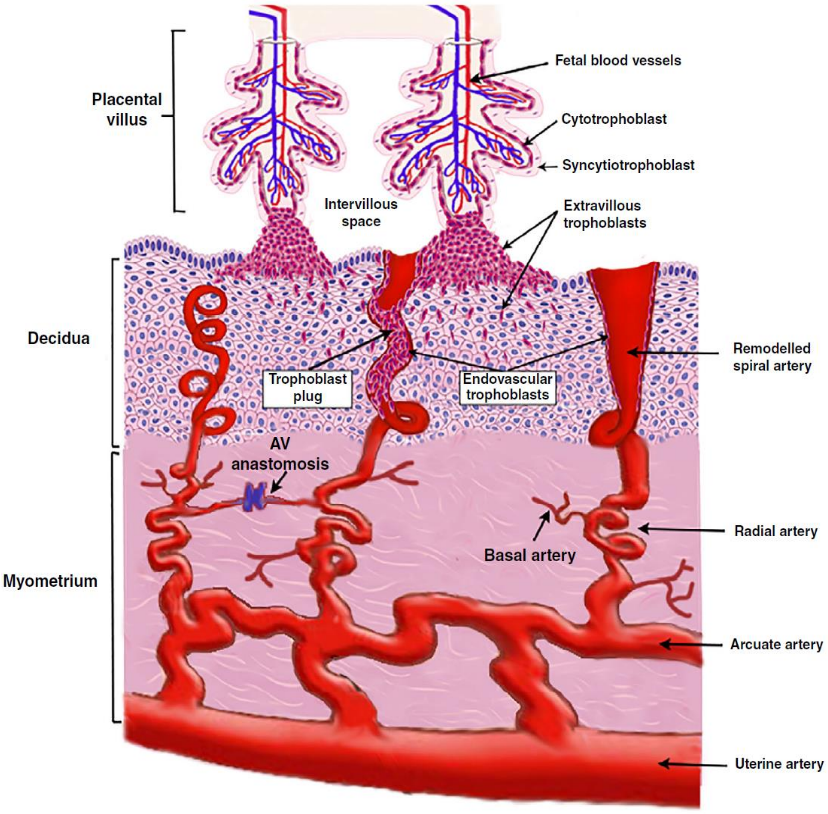

Figure 4: A diagram of utero-placenta circulation from the individual placental villi, depicted here with the outer layers of epithelial trophoblast cells surrounding the fetal blood vessels, to the maternal uterine artery. Maternal blood bathes these placental villous trees, flowing out from the spiral arteries. Deceptions of the spiral artery changes, from left to right, illustrate the extravillous trophoblast cells which migrate and invade the maternal arteries changing their structure from tightly coiled vessels to funnels. Adapted from (Clark et al.2021).

2.2 Animal models

For comparative studies with other species, it is important to consider the similarities and differences certain animals have with human physiology. In this thesis, data from rats are used as an animal model to gain further insight into how the human utero-placental system functions. Humans share a haemochorial type of placentation with rats. Haemochorial placentation has the distinct feature of maternal blood coming into direct contact with trophoblast cells, which have invaded from the placenta, in place of endothelial cells which usually line the vessel wall (Rai and Cross 2014). While humans have an intervillous space where maternal blood bathes the placental villi, rats have a labyrinth space. It is important to control the speed of blood flow into both the intervillous space (for humans) and the labyrinth space (for rodents) to prevent damage to the delicate placental structures and allow for efficient nutrient exchange. The placentation type has a significant influence on the upstream vasculature and how it changes through pregnancy (Osol and Mandala 2009).

2.2.1 Rat Uterine Structure

Rats have a double horn uterus, capable of multiple pregnancies in one gestational period. Rats do not menstruate like humans, rather decidualisation is dependent on implantation as well as hormones (Soares et al. 2011). Figure 5 depicts a single uterine horn with a uterine artery supplying the blood. The arcuate arteries form a ‘loop’, which connects back to the uterine artery and runs parallel to the uterine wall. Arcuate arteries branch into radial arteries as they enter the uterine tissue. The radial arteries feed into the spiral arteries and, rather than the intervillous space that acts as the exchange interface in human pregnancies, rats have canal vessels leading to a labyrinth zone where maternal blood can perfuse the placental trophoblasts (Osol et al. 2009). The rat does not appear to have any AV anastomoses within the myometrium (unlike humans), so there are no shunt pathways for blood at this level. It is not clear whether the connections between arcuate arteries and the uterine arteries may play a similar functional role to AV anastomoses.

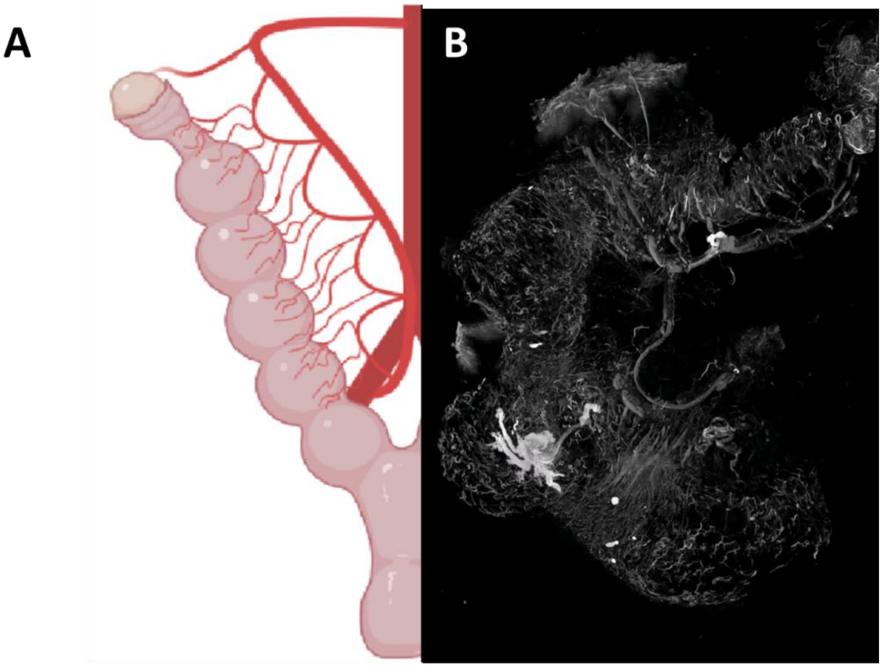

Figure 5: A) Depiction of a rat uterus showing one horn with the main uterine artery with the looping arcuate arteries branching off. The branching radial arteries to feed multiple placentations along the horn. B) A micro-CT image of a vascular cast of a pregnant rat uterine horn.

Rats and humans both undergo trophoblast invasion and the remodelling of the spiral arteries during pregnancy. The vessels upstream from the spiral arteries, like in humans, show a pattern of outward hypertrophic remodelling and a change in vascular compliance (Osol 2009). The rat uterine vasculature has a marked change in vessel axial length in pregnancy with the measurements of uterine artery length two to three times that in the non-pregnant state, and the radial/arcuate arteries exhibiting a 3 to 5 fold increase in length (Osol et al. 2014; Mandala et al. 2012). While human arteries appear to straighten in pregnancy, it is not clear whether they have genuine axial growth (James, Chamley, and Clark 2017; Osol and Mandala 2009).

2.3 Remodelling Mechanisms

The maternal uterine vasculature remodels during pregnancy, altering both vessel size and tone as resistance is dependent on these. The changes are progressive, responding to both local and systemic signals. Structural changes that occur in pregnant vessels and their active tone response can be examined to better understand the process of remodelling in these vessels (Osol 2009).

2.3.1 Blood Vessel Structure and Function

The arterial wall can be divided into three layers (Figure 6). Endothelial cells and connective tissue make up the innermost layer. The middle layer consists of elastin, smooth muscles cells and collagen. The outer layer is predominantly stiffer collagen fibres (Li 2004). The vessel's mechanical properties have a passive component, which is determined by the structure of the vessel wall itself (i.e. layer thickness), but is otherwise largely governed by the behaviour of these smooth muscle cells (Li 2004). Vessel tone (driven by smooth muscle contraction) changes in response to flow and pressure to adjust the diameter of the vessel actively. Circumferential wall tension and stress both contribute to vascular smooth muscle contractility. All uterine arteries have this structure at the start of pregnancy and some of the remodelling processes work to change this in the spiral arteries (as trophoblast invade into their lumen). In other arteries of the uterus, a prolonged elevation of blood flow (and hormonal influences) lead to a remodelling (a longer-term change in arterial structure and function). In these arteries, while the overall mechanisms of function remain, the passive (driven by vessel wall structure) and active (driven by smooth muscle) responses of the vessel change. The uterine vascular remodelling process can be broadly broken down into two categories, trophoblast dependent and trophoblast independent.

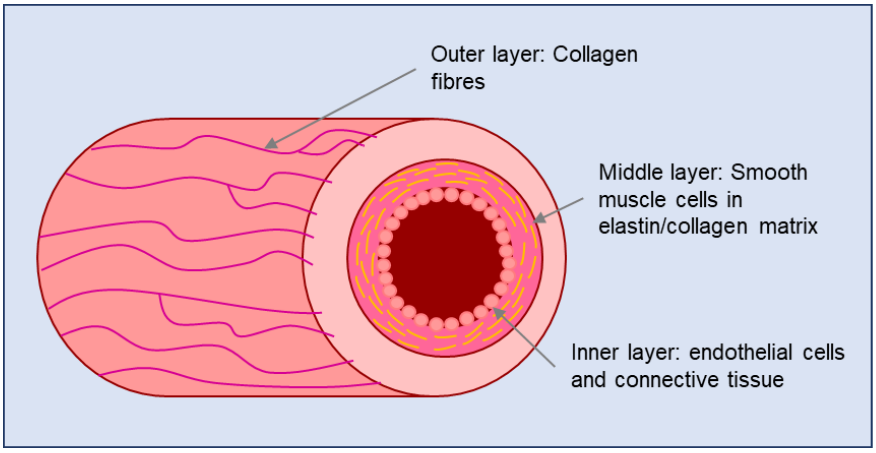

Figure 6: Arterial cross section depicting the different layers making up a typical vessel. The outer layer is predominantly made up of stiffer collagen fibres. The middle layer contains smooth muscle cells with elastin and collagen. The inner layer contains endothelial cells.

2.3.2 Trophoblast dependent

Extravillous trophoblasts migrate and invade into the decidua, inducing change in the spiral arteries from their non-pregnant state as tightly coiled structures with a high vascular reactivity, to wide, funnel like vessels, with little to no reactivity. To achieve this, the invading extravillous trophoblast cells (EVT) disrupt the smooth muscle cells (SMC) that line the spiral artery vessel walls. There is a breakdown in elastin and replacement of SMCs with EVTs, as shown in Figure 7 (Harris 2010; Khong et al. 1986).

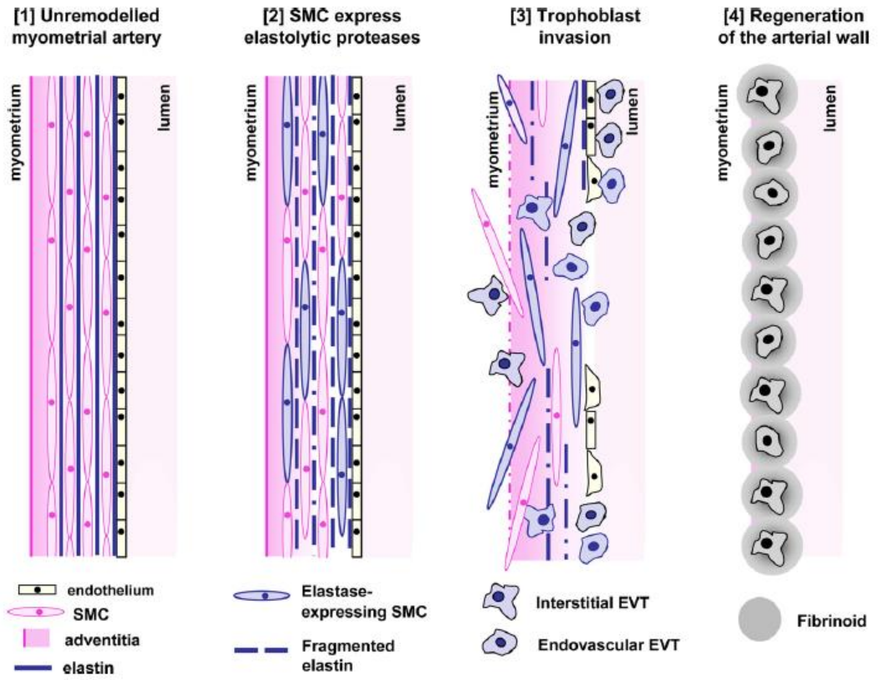

Figure 7: Reproduced from (Harris 2010). A schematic of a proposed sequence for the progressive remodelling of spiral arteries 1) An un-remodelled myometrial artery vessel wall, showing the layers typically present in a vessel wall, including closely packed smooth muscle cells interspersed with elastin fibres and an intact endothelium 2) The elastin begins to breakdown and disrupt layers of smooth muscle cells. 3) Extravillous trophoblast cells colonise the vessel walls with further loss of elastin and SMCs 4) SMC are replaced by EVT, embedded in fibrinoids.

The process of spiral artery remodelling takes place across the first twenty weeks of gestation (Allerkamp et al. 2021). Spiral artery remodelling is an important part of a successful pregnancy as it reduces the velocity of blood entering the intervillous space and enables a consistent blood supply to the placenta (Burton et al. 2009). Inadequate spiral artery remodelling is associated with pregnancy complications such as pre-eclampsia and FGR (Khong et al. 1986; Meekins et al. 1994).

As spiral artery remodelling is occurring, extravillous trophoblasts also form pseudo-plugs that limit flow to the intervillous space in early pregnancy (Figure 3) (Saghian et al. 2017). Limiting blood flow in the early stages of gestation is important as it creates a physiologically normal hypoxic environment which has been shown to be beneficial for placental development. Lower flow rates will also decrease shear stress within the spiral arteries (James et al. 2018). Endothelial cells on the inner surface of the vessels and extravillous trophoblasts invading the vessels can sense shear stress, and these low shear conditions have been shown to that enhance trophoblast migration (and endothelial cell apoptosis) (James et al. 2018).

In silico models of the remodelling spiral arteries (James et al. 2018) have lacked accurate anatomical measurements, which are required for understanding the relationship between anatomy and haemodynamics in pregnancy. A study by Allerkamp et al. analysed histological cross sections from the historic Boyd and Dixon collections, over the first 20 weeks of gestation, taking measurements of vessels and trophoblast plug characteristics (Allerkamp et al. 2021). Previous consensus in the field was that the plugs remain intact until 11-12 weeks of gestation. However, both Allerkamp et al. and Roberts et al. have noted a more progressive disintegration, with clear channels forming through the trophoblast plugs from 7 to 8 weeks gestation, wide enough to be flow pathways (Allerkamp et al. 2021; Roberts et al. 2017). These channels increase in size as remaining trophoblast aggregates condense towards the vessel walls, and as such, are thought to become the preferential pathway for flow (Allerkamp et al. 2021). How the downstream plug characteristics influence the upstream remodelling processes, and the temporal differences of these adaptations, requires further investigation (Allerkamp et al. 2021). The importance of plugs in upstream haemodynamic and how formation of channels may reduce resistance at this point in the network are yet to be quantified.

2.3.3 Trophoblast independent

The remodelling of spiral arteries through trophoblast invasion has been a focal point for research in the past because it is the most dramatic remodelling observed in the uterus. However, vessels upstream of the spiral arteries also undergo remodelling and inadequacies in this have been linked to poor pregnancy outcomes (Clark, Alys et al. 2018). Upstream vessels are not invaded by extravillous trophoblast cells but an increase in lumen is observed. This increase in lumen occurs with a corresponding change in wall thickness to maintain a constant wall to lumen ration over gestation (Allerkamp et al. 2021; Allerkamp et al. 2022), in line with a process termed ‘outward hypertrophic remodelling’ (Osol, Ko, and Mandalà; Roberts et al. 2017) (Figure 8).

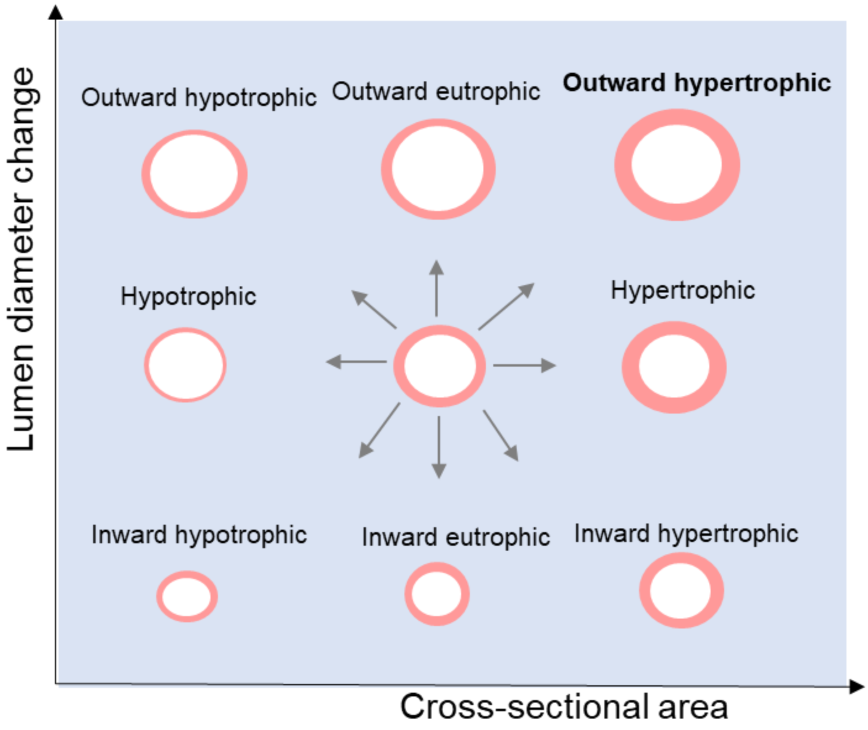

Figure 8: A diagram of the different remodelling mechanisms, plotting the two-dimensional relationship between cross section area and lumen diameter. Outward hypertrophic remodelling is in the top right corner, where an increase in inner diameter maintains wall thickness, as it is identified in uterine arteries (Osol 2009).

The outward remodelling of vessels is progressive and temporal differences exist between the vascular adaptations. The analysis by Allerkamp et al. suggested that radial arteries remain smaller than spiral arteries for the longest (Allerkamp et al. 2021; James et al. 2018). Radial arteries were quantified as having the most pronounced increase, approximately tripling in size, but this change happens later in gestation, around the 10-12 week mark to the 16-20 week (Allerkamp et al. 2021). The arcuate arteries increase in size earlier, approximately doubling in size from 6-8 weeks to 10-12 weeks of gestation (Allerkamp et al. 2021) . While the spiral arteries influence the flow pattern of blood through to the intervillous space and thus the placenta, it is likely that the upstream radial arteries are key volumetric rate limiting vessels (Allerkamp et al. 2021). Finally, the uterine arteries more than double in thickness (Palmer et al. 1992).

Maternal cardiac output also increases over pregnancy, increasing flow through the utero-placental circulation and the associated shear stress (Clapp et al. 1989). An increase in wall shear-stress is recognised as a stimulus for lumen enlargement (Osol and Mandala 2009). Vessels typically respond to the stimulus by either dilating or constricting to return shear stress to a normal set point. A pathway for this response is that shear stress stimulates endothelial NO secretion which has a vasodilator effect. While short term increases in shear stress usually have an immediate dilatory response, over time the basal set point will be altered, and this dilation/constriction response occurs over a wider vessel baseline (Baeyens et al. 2015). This process of shear stress normalisation is hypothesised to be a mechanism for vascular remodelling (Khankin et al. 2021).

The drivers for remodelling in uterine vessels are likely to be a combination of signals including shear stress, pressure, and hormones/paracrine factors (Allerkamp et al. 2021) but the mechanistic pathways and how these may be compromised in pregnancy pathologies are not yet fully understood. During pregnancy, circulating hormones as well as the hormone microenvironment in the uterus are altered. Hormones such as estrogen and progesterone and paracrine factors such as PIGF and VEGF are influential in blood vessel function (Osol and Mandala 2009; Osol et al. 2008; Gokina et al. 2009).

2.3.4 Vascular Function and the impact of pregnancy

In addition to the outward hypertrophic remodelling of these vessels, pregnancy alters vascular reactivity. Blood vessel autoregulation can be broken down into different components, which combine to give the overall response: passive vessel mechanics, an active response (myogenic), a shear-dependent response, and a metabolic response. Computational models of vascular reactivity have been used previously to better understand the behaviour of systemic vessels and contributions of the passive response, myogenic (no flow) and shear dependent (flow) in vessel autoregulation (Carlson, Arciero, and Secomb 2008; Carlson and Secomb 2005). Allerkamp et al. built on these models to consider a pregnancy specific example, investigating radial arteries in rats (Allerkamp et al. 2022). By using pressure myography to look at the vascular reactivity of rat radial arteries under static pressure and flow conditions, they were able to show that uterine radial arteries behave differently to the systemic arteries of an equivalent size with a low myogenic response and shear mediated constriction (Allerkamp et al. 2022). They found that radial arteries did not respond to low shear stress values. As shear stress increased, a flow mediated constriction rather than dilation was observed in systemic vessels

(Allerkamp et al. 2022). Additionally, pregnancy adapted the response by increasing passive vessel compliance, in line with an increase in radius. Pregnant vessels also exhibited increased myogenic responses, and under flow conditions, the vessels did not show a constricting response until higher pressures and flow rates were reached (Allerkamp et al. 2022). These differences in behaviour are an important finding as the radial arteries are considered to modulate blood flow in the system (Allerkamp et al. 2022). These new findings in radial artery vessel autoregulation behaviour have not yet been carried into a human model or incorporated into the network models of uteroplacental circulation.

2.4 Computational Models representing the uterine vasculature – A Review

Several previous models of utero-placental circulation have focused on the impact that system resistance has on UtA Doppler ultrasound. Doppler ultrasound is a common screening tool during pregnancy for detecting conditions such as preeclampsia. Clinical observation of an end-diastolic notch has been linked to FGR and preeclampsia, with uterine vascular resistance altering the Doppler waveform (Williams et al. 2018). Computational models are useful for linking measured parameters in ultrasound waveforms in clinic to possible anatomical features.

To better understand the physiological factors influencing the velocity waveforms observed in Doppler ultrasound, Mo et al. created a lumped transmission line model to simulate these waveforms (Mo et al. 1988). The group used an electric analogue model equating blood pressure to voltage and flow to electric current. From this, a vascular resistance could be calculated, and vessel compliance was incorporated as capacitance. By varying the vascular resistance, changes to wave characteristics S/D (systolic/diastolic velocity ratio) and PI (pulsatility index) were able to be measured. By varying resistance, they were able to simulate the observed diacrotic notch when the utero-placental vascular bed has an elevated resistance, which reflects a wave of high amplitude (Mo et al. 1988). The model allowed the effects of vessel radius and blood pressure on waveform shape to be elucidated. They found that an increase in vascular bed resistance resulted in the changed waveform observed in conditions such as FGR and preeclampsia. They directly linked this to incomplete spiral artery remodelling (Mo et al. 1988). While further work has shown it is likely incomplete remodelling of the entire uterine vasculature causing abnormal UtA Doppler waveforms (AV anastomoses can mask the effect of incomplete spiral artery remodelling) (Clark, Alys et al. 2018), the link to spiral artery remodelling continues to inform Doppler interpretation today.

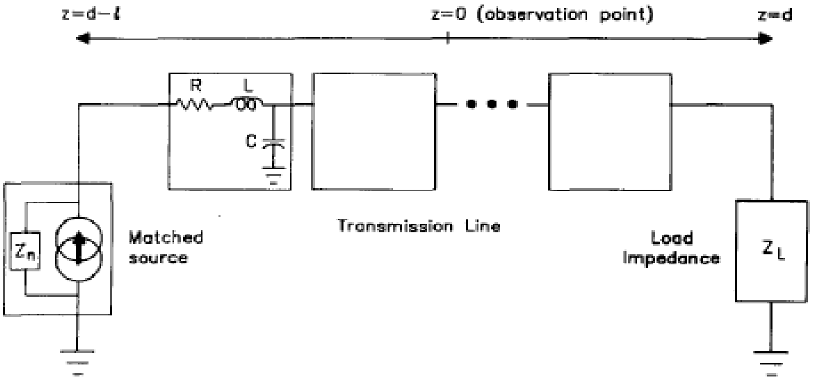

Figure 9: Reproduced from Mo et al (Mo et al. 1988). A schematic of an electrical analogue model. Transmission line theory represents the resistance of the vascular bed as a series of blocks containing a resistor to represent flow resistance (R), a capacitor (C) to represent vessel compliance and an inductor (L) for blood inertia.

While Mo et al. worked in the frequency domain, Talbert took things into the time domain with the assumption that blood momentum is a second order effect (Talbert 1995). They incorporated more detailed estimates of blood vessel size in the system and were able to produce flow velocity waveforms to match those in clinic (Talbert 1995). Similar to the findings by Mo et al., spiral artery resistance had a dominant impact in their lumped transmission line model (Mo et al. 1988; Talbert 1995). They incorporated vascular compliance into the model by likening it to a capacitor and found that notch formation depended on compliance of the artery walls (Talbert 1995).

Clark et al. built on how uterine artery Doppler wave forms are analysed (Clark, Alys et al. 2018). By incorporating the entire vascular anatomy, including AV anastomoses, they were able to better quantify the relative contributions of each vessel to overall function (Clark, Alys et al. 2018). A key finding was that AV anastomoses reduce the total resistance of the uterine vasculature by acting as a shunting pathway for blood. The model also showed that AV anastomoses can mitigate a high spiral artery resistance in terms of total uterine vascular resistance, although this increases the amount of shunted blood that does not feed the placenta (Clark, Alys et al. 2018). Rather than the spiral arteries dominating the waveform, it is in fact the radial arteries that have the largest contribution. The remodelling of radial and spiral arteries are likely to be interdependent (Clark, Alys et al. 2018; Lloyd-Davies, Collins, and Burton 2021). All previous modelling studies that aim to replicate Doppler have limited data for uterine vasculature dimensions. Estimates are made from literature and their impact on model predictions assessed. Clark et al. identified that if more detailed structural and functional data could be incorporated then the model could be improved (Clark, Alys et al. 2018).

Aside from a focus on Doppler, computational modelling has been used to investigate the impacts trophoblast plugs have on uterine haemodynamics (James et al. 2018). This model incorporated the geometrical properties of the spiral arteries based on reconstructed histological images (James et al. 2018). The characteristics of the trophoblast plugs were captured as porosity and plug length from published histological sections. Arteriovenous pathways were included with resistance and varied until a flow velocity criterion was met. Boundary conditions were defined as blood pressure at the radial artery, the entrance to the IVS and at the uterine veins. Different scenarios were run to determine the extent to which the plug structure influences blood flow rate into the IVS. This work showed that, as the plugs break down, the rate of blood flow reaching the IVS will rapidly increase in a nonlinear relationship at the upper limits (James et al. 2018). The study also simulated shear stress at the artery wall, as this has been previously linked to effective spiral artery remodelling (James et al. 2018). The model identified that the plug structure impacted the spiral artery resistance with a range of porosity and plug lengths modelled. When plugs are intact, a high portion of blood is being bypassed via the AV anastomoses to the venous circulation (James et al. 2018). Although the model incorporated new data on the changes to spiral artery structure in early gestation and summarised literature data on plug composition, there were still several unknowns in terms of the anatomy of the blood vessels (James et al. 2018). Incorporating a more detailed description of trophoblast plugs as they dislodge across gestation would help to improve the model. While AV anastomoses were included in the model, they require a more accurate quantification. The autoregulation behaviour of radial arteries requires further investigation as they were identified as important rate limiters for flow through to the IVS (James et al. 2018).

Models of the spiral artery openings and maternal blood flow patterns into the intervillous space have helped to inform how maternal blood flow interacts with the placental villous tree structures and the capacity for nutrient exchange (Saghian et al. 2017; Lin et al. 2016). Spiral arteries were modelled as a cylindrical tube with a funnel shaped openings (Burton, G. J. et al. 2009) into the IVS with a central cavity (region free of placental villi) at the SA openings (Saghian et al. 2017). Findings from the model suggest that the structure of spiral artery openings controls blood flow penetration into the IVS (Saghian et al. 2017). Modelling of cavities predicts that maternal blood jet length is associated with cavity size (Saghian et al. 2017).

In summary, Doppler indices measured through ultrasound in clinic and waveform patterns such as the 'notch' have been used to predict poor pregnancy outcomes. Initial studies correlated this altered waveform with poorly adapted spiral arteries creating increased resistance observable at the uterine artery. Further evidence suggests that this overly simplistic as they are unlikely to be the main contributor to the overall uterine vascular resistance. The inclusion of AV-anastomses into network models provides an alternative pathway for blood flow. With this addition, radial arteries have been highlighted as potential rate limiters for flow and influence UtA Doppler wave forms. Further work is required to determine the timeline of the observed anatomical changes (Lloyd-Davies, Collins, and Burton 2021).

2.5 Thesis Overview

This thesis aims to build on existing models of utero-placental circulation to better reflect how new plug characteristics and vessel size measurements influence the systems function. The models have also been extended incorporate a vascular autoregulation response for pregnant and non-pregnant radial arteries.

Chapter 3 considers the anatomical changes of the uterine vasculature captured by Allerkamp et al. (Allerkamp et al. 2021, 571), and aims to quantify the impacts these anatomical parameters have on the maternal uterine circulation. A new functional description captures the observed channels through the trophoblast plugs as they progressively breakdown across gestation. By incorporating this functional description, the impact trophoblast plugs have on the overall system resistance and haemodynamics can be quantified at this point in gestation. A focus was placed on flow and shear stress predictions at the radial artery level, as these have been identified as key modulators of flow, but the upstream arcuate and uterine arteries are also considered. A comparison is made between these human models of uterine circulation to models of rat uterine circulation, non-pregnant and pregnant.

Chapter 4 explores models of vascular autoregulation for uterine specific arteries and how this vascular compliance alters with pregnancy. A model of vessel autoregulation based on pressure myography data obtained for a rat data set on the vascular response of pregnant and non-pregnant radial arteries (Allerkamp et al., 2022) is used to parameterise a human model for vascular reactivity. A simple model of compliance based on a linear relationship between pressure and diameter is used as a comparison. These models for single vessel compliance were then incorporated into the network models outlined in Chapter 3.

The key findings of this thesis and potential points of focus for future work in this area are summarised in Chapter 5.

Chapter 3 – Fixed Geometry Network Models of Utero-placental Circulation

3.1 Motivation

Previous computational models have used electrical circuit theory to represent the uterine vasculature to enable a better understanding of the functionality of the system and how each part of the system contributes (i.e. the arteries that feed the placenta and the placenta itself) (Mo et al. 1988; James et al. 2018; Clark, Alys et al. 2018). Modelling of the uterine circulation to date has been limited by a lack of detailed measurements of the vasculature throughout gestation. Accurately capturing the physical geometries and the arrangement/connectivity of the vessels will help the understanding of how fluid flows through the vasculature and determine which components of the circulatory system are most important for a healthy delivery of maternal blood to the placenta. Simple anatomical measurements of plug characteristics were incorporated in a prior study modelling fluid flow through a porous plug (James et al. 2018). However, the anatomical data describing trophoblast plugging at the time were limited to reviews of the literature and a small number of histological sections. New insights into the dynamic structural changes captured by Allerkamp et al., and the observation of channels through the plugs (Allerkamp et al. 2021) are yet to be included accurately in modelling studies.

Chapter 3 explores network models of human uterine circulation, beginning at the uterine artery and ending at the intervillous space. The models outlined in Chapter 3 are established for a fixed geometry, at steady state with no active function included. Three anatomically distinct models were defined to capture the important remodelling changes over these first 20 weeks of gestation; 1) 6 to 8 weeks, 2) 10 to 12 weeks, and 3) 16 to 18 weeks. Blood vessel metrics and plug parameters quantified by Allerkamp et al. (Allerkamp et al. 2021) were incorporated and assessed for how they impact overall network function. A description for flow through a clear channel in a porous surround was created to model the channels observed to form through the trophoblast plugs as they break down. Finally, as functional measurements of arterial function (or reactivity, Chapter 4) cannot be made directly in humans, but rather require animal models, rat models were also generated in order to draw interspecies comparisons and better understand how animal model function relates to expected human function.

3.2 Model Geometries

The blood vessels in the uterine circulation are branching in nature. Beginning at a parent vessel, in this case the uterine artery, and moving down generation levels to the spiral arteries at the inner wall of the uterus. Typically, vessels increase in number and reduce in lumen diameter moving down the tree. The vasculature changes over the timescale of gestation with a largening of vessel lumen, the reshaping of spiral arteries through the invasion of trophoblast cells and the formation of plugs (Allerkamp et al. 2021; James et al. 2018). These changes occur dynamically over different temporal scales. Observations of the Boyd and Dixon collection identified that as the trophoblast plug progressively breaks down (Allerkamp et al. 2021; Clark, Alys R., Lee, and James 2021) a clear channel, presumably of preferential flow (Saghian et al. 2019), forms in the plug. As gestation progresses this clear channel grows, and the aggregates of the plug coalesce at the vessel walls.

A geometric representation of the uterine arterial system is constructed by grouping arteries into their anatomic "levels" within the vascular tree. For example, all spiral arteries are grouped together, all radial arteries are grouped together, and so on. It is assumed that each artery at a vessel level has the same radius (r_i, where *i* is level) and length (l_i). There are n_i vessels at each level. In a symmetric tree, n_i would double at each level, but the uterus does not exhibit symmetric branching. Three human model geometries were defined, capturing points in the remodelling process at key stages over the first half of pregnancy 6 to 8 weeks, 10 to 12 weeks and 16 to 18 weeks. Two rat models were considered, one defining virgin anatomy (non-pregnant) and the other capturing late-stage pregnancy (pregnant). The rat uterine arterial system contains similar vessel levels within a branching network. Figure 10 illustrates the connectivity of the different vessel levels that make up the human and rat anatomies.

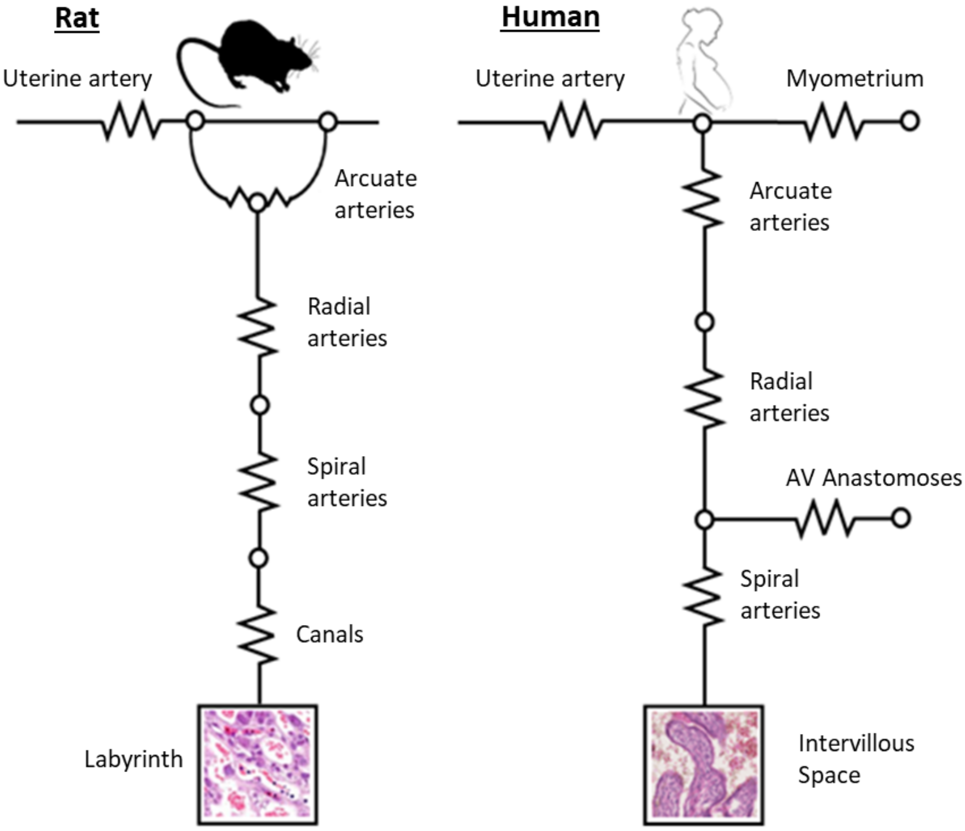

Figure 10: Adapted from Allerkamp et al. (Allerkamp et al. 2022) this diagram is a representation of the electric circuit theory network model for utero-placental circulation. A model overview for rat anatomy (Left) and human anatomy (right), demonstrate the connectivity of vascular levels, with each level represented by a resistor. The rat model terminates at the labyrinth and human model at the intervillous space.

3.2.1 Human Anatomy

The human uterine arterial system begins at the uterine artery and ends at the intervillous space (IVS), in which blood flows over the surface of the placenta to nourish the growing fetus. From the main uterine artery, blood either flows toward the placenta or feeds the uterine tissue that does not supply the placenta (the non-placental myometrium) (Talbert 1995). Blood that travels toward the placenta traverses the arcuate and radial arteries. From here, it can either bypass the placenta via AV-anastomoses or it will reach the surface of the placenta at the IVS via the spiral arteries. For the purpose of this model, the complexity of flow in the IVS and the non-placental myometrium are represented as individual resistors with a fixed resistance (Clark, Alys et al. 2018; Talbert 1995) . All other blood vessels in the system are defined as resistors and the same parameters represent all blood vessels in that generation (or level). There are five generations of blood vessels in the uterus that are explicitly represented in this model: 1) the uterine artery, 2) the arcuate arteries, 3) the radial arteries, and 4) the spiral arteries. AV-anastomoses that bypass the placenta are also explicitly represented (Talbert 1995; Clark, Alys et al. 2018).

The model proposed here of the whole human uterus improves on existing models of the same system (Clark, Alys et al. 2018) in three ways: 1) it is parameterised to represent the most up-to-date anatomical data on uterine vascular structure, and 2) it defines the spiral arteries rather than lumping spiral artery resistance with IVS resistance (Clark, Alys et al. 2018; Mo et al. 1988), and 3) it describes the evolution of spiral artery anatomy through pregnancy rather than treating spiral arteries as tubes (Talbert 1995, 261-271).

The remodelling of the spiral arteries is represented in the model by considering the artery as segments represented by either a clear tube, a funnel (section of tube increasing in radius), and then a plugged segment that is either a homogenous porous plug, or a porous plug with a clear channel through it (Figure 11). This expands on previous descriptions of the spiral artery as a simple funnel (Burton, G. J. et al. 2009, 473; Saghian et al. 2017) or as a plugged tubular segment (James et al. 2018, 1430-1441).

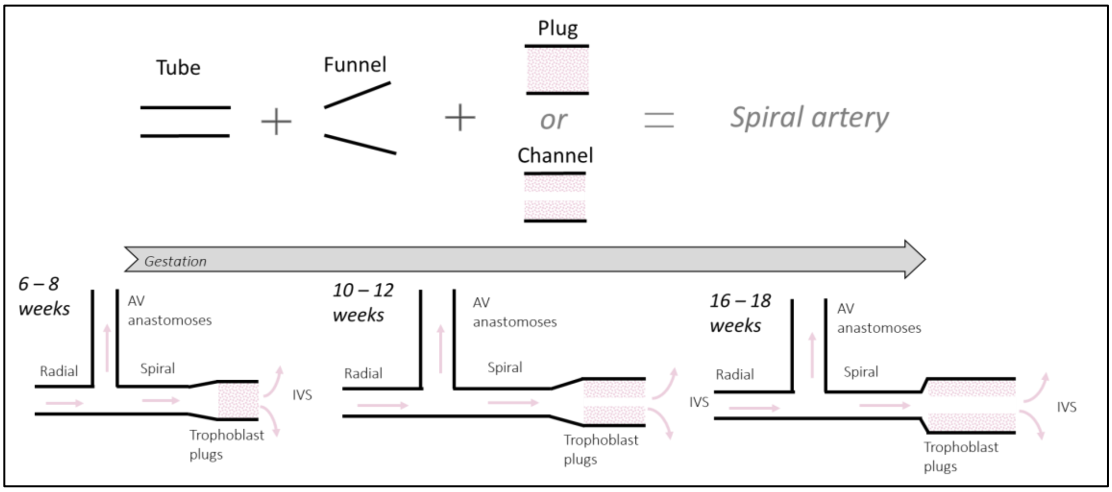

Figure 11: A diagram showing the combined functions to represent a spiral artery at key gestational stages. The segment can be broken down into a tube, funnel and either a plug or channel to represent the different stages of spiral artery remodelling.

Quantification of vessel dimensions: Measurements were captured from a review of the Boyd and Dixon collection of human placenta, made up of a series of histological cross sections of fixed tissue (Allerkamp et al. 2021) (Table 1). Images of the serial sections were captured and blood vessel metrics were quantified from in situ measurements over specimens ranging 6.1-20.5 weeks gestation (Allerkamp et al. 2021). Vessel levels were assigned based on the location in the tissue and measurements averaged across neighbouring cross sections (Allerkamp et al. 2021). Manual segmentation of inner and outer lumen provided quantification of luminal area and vessel wall area of the vessels (Allerkamp et al. 2021). Plug porosity (see section 3.4.2) and plug depth were also quantified. Values of channel width were taken from Allerkamp et al (Allerkamp et al. 2021). Vessel numbers at each level, and length parameters that could not be captured by this study, were taken from other sources in the literature.

Table 1: Table of vessel geometries at different gestational stages for human anatomy. [1](Allerkamp et al. 2021), [2](Clark et al. 2018), [3](Browne et al. 2015), [4](Burton et al. 2019),[5](Itskovitz, Lindenbaum, and Brandes 1980), [6](James et al. 2018), [7](Talbert 1995).

Gestational stage	6 to 8 weeks						
Generation	1	2	3	4	5	6	7
Vessel type	Uterine	Arcuate	Radial	Anastomose	Spiral tube	Spiral funnel	Spiral plug
# vessels	1	2[5]	50[2]	50[2]	50[7]	50	50
Radius (mm)	0.95[3]	0.249[1]	0.112[1]	0.032	0.036[1]	0.123[1]	0.123[1]
Length (mm)	100[2]	9[7]	6[2]	6.5[7]	7[4]	1.7[1]	1.3[1]
Gestational stage	10 to 12 weeks						
Generation	1	2	3	4	5	6	7
Vessel type	Uterine	Arcuate	Radial	Anastomose	Spiral tube	Spiral funnel	Spiral channel
# vessels	1	2[5]	50[2]	50[2]	50[8]	50	50
Radius (mm)	1.1[3]	0.03[2]	0.18[1]	0.05	0.124[1]	0.175[1]	0.175[1]
Length (mm)	100[2]	9[7]	6[2]	6.5[6]	7[4]	1.6[1]	1.4[1]
Gestational stage	16 to 18 weeks						
Generation	1	2	3	4	5	6	
Vessel type	Uterine	Arcuate	Radial	Anastomose	Spiral tube	Spiral channel	
# vessels	1	2[5]	50[2]	50[2]	50	50	
Radius (mm)	1.4[3]	0.403[1]	0.257[1]	0.1	0.3[1]	0.241[1]	
Length (mm)	100[2]	9[7]	6[2]	6.5[6]	7[4]	3[1]	

Table 2: Trophoblast plug measured characteristics for the three gestational models, measurements from Allerkamp et al. (Allerkamp et al. 2021).

Gestational stage	6 to 8 weeks
Porosity (area)	2.80E-01
Porosity (adjusted)	-
Channel radius (mm)	-
Particle diameter (mm)	0.04
Gestational stage	**10 to 12 weeks**
Porosity (area)	0.521
Porosity (adjusted)	0.123
Channel radius (mm)	0.0337
Particle diameter (mm)	0.04
Gestational stage	**16 to 18 weeks**
Porosity (area)	0.587
Porosity (adjusted)	0.164
Channel radius (mm)	0.162
Particle diameter (mm)	0.04

3.2.2 Rat Anatomy

Figure 10 illustrates the connectivity of the different vessel levels that make up the rat anatomy model. Unlike the human uterus which typically contains only one placenta and fetus, the rat uterine horn contains several placental beds that form a line along the horn (Figure 5). This means that in the rodent model of the uterus, blood coming from the main uterine artery either travels to the first placental bed along the horn or passes on to the next placenta. For each placenta of n_p situated along the horn, from the uterine artery branch the arcuate arteries, which in turn branch into the radial arteries, with the arcuate artery branch typically continuing back to merge with the uterine artery. The radial arteries feed into spiral arteries, and for the rat, the spiral arteries connect to the canals and flow into a labyrinth (Soares et al. 2011). There are no AV anastomoses to shunt blood directly to the veins identified in rats. However, the arcuate artery forms a shunt pathway that connects the uterine artery back to itself. Like in the human model, the rat model explicitly includes representations of the arteries that feed the placenta: 1) the uterine artery, 2) the arcuate artery, 3) radial arteries, 4) spiral arteries, 5) canals. The model lumps the complexity of the labyrinth into a single resistance, in the same way that the IVS is considered as a lumped resistance in the human model. In the rat model n_p repeating units are in series along the length of the uterine horn.

Table 3 outlines the geometries included in the rat models for a virgin (non-pregnant) and pregnant state. Measurements were captured from microcomputed tomography (micro-CT) imaging analysis performed on rat uteri (Schnauer 2021). A contrast agent was injected into the uterine circulation of post-mortem animals which highlights the vessels in the images relative to the surrounding flesh. The micro-CT scan can take a series of 2D images which can then be reconstructed into a 3D stack. A thresholding process identifies vessel structures, which were then manually corrected to correct misidentified features and separate out the vessels that are connected from the uterine artery to a single placenta. The manually segmented vasculature is skeletonised, which captures the geometry by representing the centre lines of the vessels. Nodes (a collection of points in space) and elements (connect the nodes) that represent this centreline are created, and duplicates or errors are removed manually. Finally, key vessel parameters can then be extracted from these simplified representations of the anatomy such as radius, length (Euclidean or branch length) and tortuosity. Vessels levels (the type of artery) are defined for the segmented and skeletonised representations, allowing the grouping of vessel type for the network models. Pregnant and non-pregnant rat uteri were analysed to quantify the effect of pregnancy (Schnauer 2021).

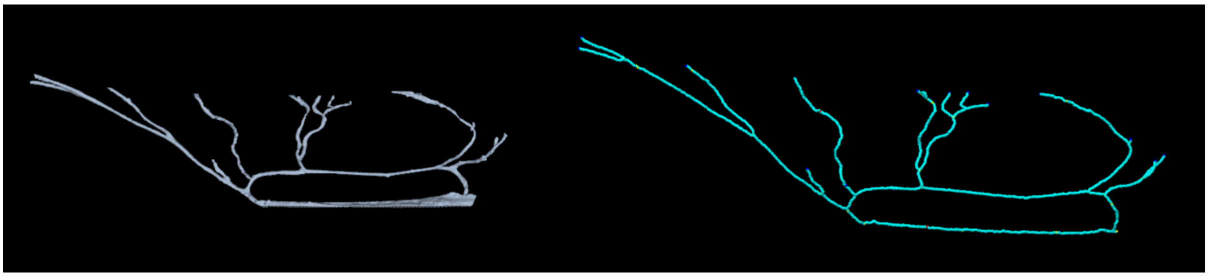

Figure 12: An example of the final produced images from the rat micro-CT analysis. Left - final image from segmentation process. Right - final image from skeletonization (Schnauer 2021).

Table 3: Rat vessel geometries in the non-pregnant (virgin) and late-pregnant (E19.5) states (Schnauer 2021).

Non-pregnant	(virgin)					
Generation	1	2	3	4	5	6
Vessel type	InUterine	Uterine	Arcuate	Radial	Spiral	Canal
# vessels	1	1	0.63	4.53	13	1.5
Radius (mm)	0.14	0.14	0.06	0.04	0.25	0.403
Length (mm)	5.4	5.7	6.19	4.1	0	0
Pregnant						
Generation	1	2	3	4	5	6
Vessel type	InUterine	Uterine	Arcuate	Radial	Spiral	Canal
# vessels	1	1	0.63	4.53	13	1.5
Radius (mm)	0.25	0.25	0.14	0.075	0.25	0.403
Length (mm)	9.3	9.07	10.47	19.7	6.12	7.2
# of placentae	7					

3.3 Flow and pressure distribution in the vascular network

The uterine artery is assumed to be the inlet to the system and, as each vessel within a group is assumed to be identical, flow is assumed to be evenly divided across each of n_a arteries within the same level. An electrical circuit equivalent model of resistances is assumed. Each vessel segment can then be assigned a resistance. The branching structure means some of the resistances will be related in series and some in parallel to calculate a total system resistance.

Resistance in series

$$R_T = R_1 + R_2 \tag{1}$$

Resistance in parallel

$$\frac{1}{R_T} = \frac{1}{R_1} + \frac{1}{R_2} + \frac{1}{R_3} \dots \tag{2}$$

where R_T is the total resistance, and R_1 , R_2, … are individual resistances in branches. As an illustration, branches in a network that are at a single vessel level are assumed to be in parallel and each vessel level is in series to the next level (Christensen 2009). The resistance of a single level *i* is related to the resistance of arteries in that level R_i and the number of arteries in that level n_{ai} *by* $R_T = R_i / n_{ai}$.

The whole system can be approximated to an electric circuit model, relating pressure to both flow and resistance. In an electrical circuit the relationship would be $V = IR$, where V is voltage, I is current and R is resistance. The equivalent for fluids is a driving force of the pressure difference ΔP, volumetric flow rate Q and fluid resistance R (Christensen 2009).

$$\Delta P = QR \tag{3}$$

3.4 Resistance Functions

3.4.1 Human

The resistance of each type of artery in the system depends on its structural parameters. Functions were created to represent the different vascular geometries at the different stages of remodelling over the course of pregnancy. Previous models applied to the uterus have defined functions for a clear tube, a porous plug, and a funnel geometry. However, porous plugs with a channel running through them have not been mathematically considered in these models.

a) Tube resistance

Fluid flow in a circulatory system is governed by the Navier Stokes equations. However, under assumptions of a Newtonian fluid and laminar flow through a uniform tube and circular cross section (Tuma, Durán, and Ley 2008) these equations can be simplified to Poiseulle's law, which takes the same form as equation (4) for fluid flow through a cylindrical tube of radius r and length L, and fluid viscosity μ. Flow resistance R under these assumptions is

$$R = \frac{8\mu L}{\pi r^4} \tag{4}$$

A steady state model takes radius (r) and length (l) as fixed. In this chapter the vessels in the system are assumed to be rigid however, blood vessels typically respond dynamically to pressure by changing lumen. This assumption is relaxed in Chapter 4 with the inclusion of vascular reactivity. The viscosity (μ) is that of blood at 3.4x10^{-3} Pa.s (Talbert 1995).

b) Plug resistance function

For a plugged segment of tubular vessel, representing plugged spiral arteries that are filled with trophoblast cells and do not contain channels, a resistance law considering flow through a porous medium was used (the Darcy-Brinkman law applied to a cylinder). Porosity (ɸ) is defined as the ratio of total volume of void space to total volume of medium. This effectively represents the extent of packing of trophoblast cells within a plug, which for this system can be defined as total artery luminal area to the area covered in trophoblast cells. Plug porosity measurements were quantified from 2D images using a custom Matlab script to identify area of artery filled with trophoblast cells (Allerkamp et al. 2021). Area porosity is defined as the ratio of luminal area to area containing trophoblast cells. Where channels were identified, an adjusted porosity was calculated by manually segmenting the channel and excluding it from the porosity measurement (Allerkamp et al. 2021).

Permeability (K) through a porous medium can be estimated using Carman-Kozney relationship (Kaviany 1995)

$$K = \frac{D_p^2}{180}\frac{\phi^3}{(1-\phi)^2} \tag{5}$$

where particle diameter (Dp) is set at the average diameter of the trophoblast cells, the particles defined in this scenario. Porosity (ɸ) is taken as either area or adjusted, depending on the defined geometry.

Using the Einstein formula for the effective viscosity (Kaviany 1995) and the Brinkman approach for fluid flow through a porous mass (Brinkman 1949) where ɸ is porosity of the medium as an approximate for γ (where γ is the ratio of actual to effective viscosity).

$$\gamma = \frac{1}{(1 + 2.5(1-\phi))} \tag{6}$$

Taking volumetric blood flow through a porous plug, an effective resistance can be calculated from modified Darcy flow where I_0 and I_1 are modified Bessel functions, μ is blood viscosity, L is length of arterial section and r is radius.

$$R = \frac{\mu L}{K\pi r^2}\left(1 - 2\left(\frac{\left(\sqrt{\frac{K}{\gamma}}\right)}{r}\frac{I_1\left(\sqrt{\frac{\gamma}{K}}r\right)}{I_0\left(\sqrt{\frac{\gamma}{K}}r\right)}\right)\right)$$

(7)

c) Channel Resistance Function

The final model, where blood can flow either through the porous plug or the clear channel it surrounds, has not been previously considered when modelling the uterus. To approximate this geometry, a clear central channel, surrounded by a porous medium, with an impermeable wall at the outer boundary of the blood vessel (tube) is considered. Appendix A outlines the derivation of resistance equations that represent this. Flow within the clear central channel, Q_1, is

$$\underline{Q}_1 = \frac{2\pi}{\mu L}\left(\underline{c}_2\frac{r_1^2}{2} - \frac{r_1^4}{16}\right)$$

(8)

where L is the length of the section tube, r_1 the radius of the clear channel and c_2 as a constant.

Fluid flow through the porous surrounds, Q_2, is

$$\underline{Q}_2 = \frac{2\pi}{\mu L}\left(\underline{c_3}\left(r_2 I_1\left(\sqrt{\delta r_2}\right) - r_1 I_1\left(\sqrt{\delta r_1}\right)\right) - \underline{c_4}\left(r_2 K_1\sqrt{\delta r_2}\right) - r_1 K_1\left(\sqrt{\delta r_1}\right) + k\frac{r_2^2 - r_1^2}{2}\right)$$

(9)

where r_2 is the radius of the outer tube and r_1 is the radius of the clear channel. I_1 and K_1 are modified Bessel functions of zeroth order of the first kind and second kind respectively. Parameters c_3 and c_4 are constants, k is permeability (as defined above) and γ as defined above in equation 6. δ is defined as the following relationship between gamma γ, and permeability, k.

$$\delta = \frac{\gamma}{k}$$

(10)

Total flow through this geometry is defined as the sum of the flow through the porous surrounds, Q_1 and Q_2 is the flow through the clear tube.

$$Q_T = Q_1 + Q_2$$

(11)

Resistance of the segment, R, is defined as

$$R = \frac{\Delta P}{Q_1 + Q_2} = \frac{1}{Q_T}$$

(12)

where ΔP is the pressure drop across the vessel segment.

d) Funnel Resistance Function

Where the geometry of a spiral artery can be described as a funnel shaped segment of tube, increasing from point a with smaller inlet radius (r_a), to point b with a larger outlet radius (r_b) (Burton, G. J. et al. 2009). Length L_a, is defined as the distance down the main axis of the tube to where the funnel begins, and length L_b is the distance down the main axis to the funnel end. The parameter c is defined the rate of increase.

$$c = \frac{r_b - r_a}{L_b - L_a}$$

(13)

Resistance in this case is determined by the modified flow relation equation (Burton, G. J. et al. 2009).

$$R = \frac{8\mu}{\pi r_a^4}\left(\frac{r_a}{3c} - \frac{r_a^4}{3c(r_a + c(L_b - L_a)^3}\right)$$

(14)

3.4.2 Rat

The resistance of a rat artery can be modelled as a cylindrical tube using equation 4 with a radius (r) and length (l).

3.5 Shear stress

3.5.1 Human

The model predicts shear stress (τ) at the vessel wall, where this is likely to be of physiological relevance, in a tube and a porous plug.

a) *Tube shear*

Following a simple Poiseuille tube, where μ is viscosity, Q is flow rate and r is radius (Tuma, Durán, and Ley 2008)

$$\tau = \frac{4\mu Q}{\pi r^3}$$

(15)

b) *Porous plug shear*

For a completely plugged segment of artery, shear stress is calculated using a Brinkman viscous term. Permeability (K) and gamma (γ), defined above in equations (5) and (6).

$$\tau = \frac{\sqrt{\gamma} Q R}{L} \frac{I_1\left(\sqrt{\frac{\gamma}{K}} r\right)}{I_0\left(\sqrt{\frac{\gamma}{K}} r\right)}$$

(16)

3.5.2 Rat

Similarly, the rat model predicts shear for a tube or radius r, flow rate Q and fluid viscosity μ following equation 15.

3.6 Boundary conditions

Pressure and flow rate are set values at the inlet defined at the uterine artery. A terminal resistance is defined at the intervillous space for humans and the labyrinth for rats. For the venous circulation, the same assumption as model by Clark et al. (Clark, Alys et al. 2018) was incorporated, such that venous resistance is half the value of arterial resistance upstream of the AV anastomoses.

Table 4: The boundary conditions for the three gestational models of human pregnancy.

Inlet	**Unit**	**6 to 8 weeks**	**10 to 12 weeks**	**16 to 18 weeks**
Static Inlet Pressure	mmHg	80	82	84
Reference		(Hunter and Robson 1992)		
Steady Flow Rate	mL/min	24.3	27.2	39.5
Reference		fits to measurements acquired from (Assali, Nuwayhid, and Zugaib 1978; Burton, Alan C. (Alan Chadburn) 1972)		
Terminals				
Myometrial Resistance	Pa.s/mm3	25.8	25.8	25.8
IVS resistance	Pa.s/mm3	1.3	1.3	1.3
Number IVS		1	1	1
Reference		(Clark, A. R. et al. 2018)		

Table 5: The boundary conditions for the rat virgin and pregnant models of pregnancy (Allerkamp et al. 2022).

Inlet	**Unit**	**Virgin**	**Pregnant**
Static Inlet Pressure	mmHg	106	82
Steady Flow Rate	mL/min	1.2	27.2
Number placentae	-	7	7
Terminals			
Labyrinth Resistance	Pa.s/mm3	400	25.8
Number Labyrinth	-	1	1

3.7 Results

To investigate the impact of the different remodelling process on the network model, trophoblast plug characteristics and vessel radii quantified in prior studies (Allerkamp et al. 2021) were used to parameterise network models of the uterine circulation. Three separate models were created for key gestational stages over the first half of pregnancy incorporating the measurements obtained for 1) 6 to 8 weeks, 2) 10 to 12 weeks and 3) 16 to 18 weeks.

For each parameter, a sensitivity analysis was conducted to assess how changes in vessel and plug characteristics effect shear stress and flow rate in the upstream arteries. Keeping other parameters constant, individual parameters were adjusted over a set range and the model run. The parameters tested were vessel radius, plug porosity, plug depth, radius of channels, and vessel lumen. Focus was placed on the radial arteries, but the arcuate and uterine arteries were also considered. The different functions that were implemented to calculate flow either through a porous plug or a clear channel with porous surrounds were also assessed.

3.7.1 Vessel lumen and shear stress relationship

The remodelling of the uterine blood vessels during pregnancy involves an outward hypertrophic enlargement of vessel lumen. Figure 13 plots the relationship between radius and shear stress for a range of physiological values for radius at the radial, arcuate and uterine artery levels. This physiologically reflects a change in the extent of outward remodelling in these arteries. The physiological radius, which is the average measured (Allerkamp et al. 2021) is also plotted for reference, labelled as ‘default’. In the radial arteries, for radius values below the physiological, shear is predicted to increase, suggesting that if these vessels stayed smaller than predicted, shear stress would increase at these arteries. For radial lumen at 6-8 weeks, at half the size of the physiological, a shear stress of 6 fold larger than physiological is predicted, while at a radial lumen double the physiological predicts a shear stress of 0.9 fold smaller than the modelled physiological shear stress (Figure 13A). For the arcuate lumen at 6-8 weeks, at a radius half the size of the physiological, a shear stress of 0.8 fold larger than physiological is predicted, while at an arcuate lumen double the physiological predicts a shear stress of 0.96 fold smaller than the modelled physiological shear stress (Figure 13B). For the uterine lumen at 6-8 weeks, at a radius half the size of the physiological, a shear stress of 6 fold larger than physiological is predicted, while at a uterine lumen double the physiological predicts a shear stress of 0.9 fold smaller than the modelled physiological shear stress (Figure 13C). For the arcuate arteries at 10-12 week model, a 4 fold increase in shear stress is observed at a radius half the physiological size relative to the shear stress at physiological size (Figure 14B). For the 16-18 week model, this reduces to a 2.8 fold change (Figure 14A and Figure 15B). At the uterine artery level, a 7 fold increase in shear stress is observed at a radius half the physiological size relative to the shear stress at physiological size at both the 10-12 week model and the 16-18 week model (Figure 14C and Figure 15C). The effect of radius is non-linear, consistent with the Poiseuille resistance model used to describe their function (equation 4).

The model predictions in the upstream arteries (radial, arcuate and uterine) were then compared with the inclusion of trophoblast plugs and the exclusion of trophoblast plugs (assumed to be a tube), to investigate how plugging may either promote or impair the uterine vasculature from remodelling effectively. Comparing plugged and unplugged scenarios across the arterial tree shows that the trophoblast plugs have the greatest haemodynamic impact on the vessels closest to them in the network. At the physiological radius, shear stress was 0.6 fold higher in the radial arteries when the spiral artery section was not plugged with trophoblast aggregate compared to when there was plugging (Figure 13A). The arcuate arteries had a similar difference at the physiological radius 0.6 fold higher in the arcuate arteries when the spiral artery section was unplugged with compared to when there was plugged with trophoblast aggregates (Figure 13B). There was no difference in shear stress predictions at the uterine arteries in the presence of trophoblast aggregates within the spiral arteries (Figure 13C). Figure 14A, B and C plot the same relationships at 10 to 12 weeks of gestation, with a 2.4 fold increase in shear stress in a network with unplugged spiral arteries relative to plugged at the radial artery level, and a 2.3 fold increase at the arcuate artery level. Figure 15A, B and C plot the same relationship at 16 to 18 weeks gestation. At this gestation the difference between the predicted shear stress values is negligible between the section of spiral artery with trophoblast aggregates and a section of spiral artery with no trophoblast aggregates.

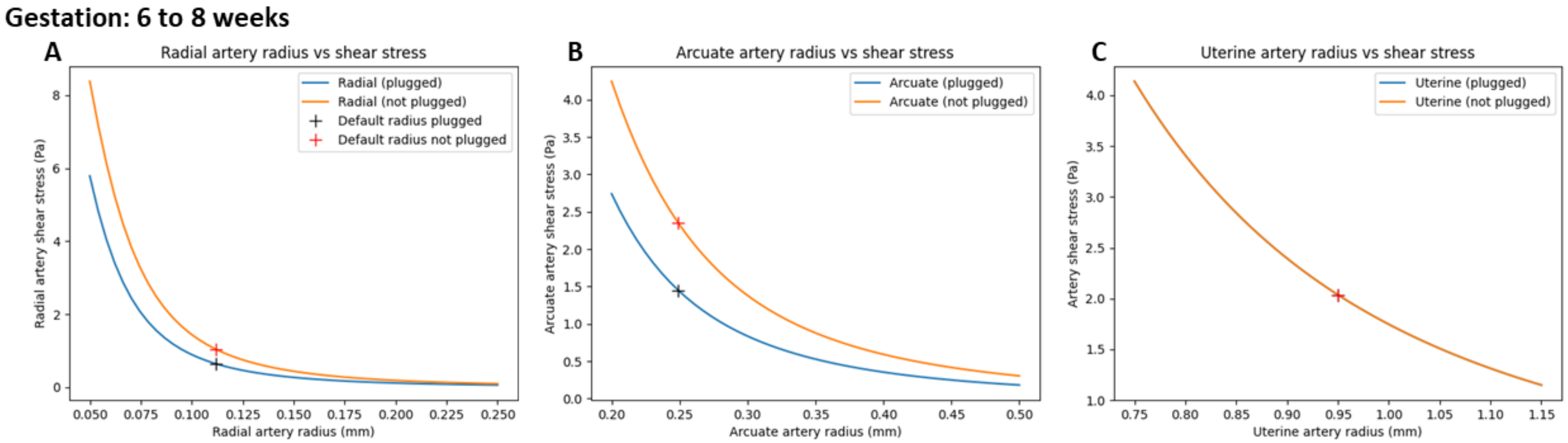

Figure 13: Plots of the relationship between artery radius and shear stress for plugged and unplugged cases for the 6-8 weeks gestational stage model. A) This plot is at the radial artery level B) This plot is varying radius at the arcuate arteries. C) This plot is varying uterine artery radius. The measured radius values are also shown on the plots, labelled as default (+).

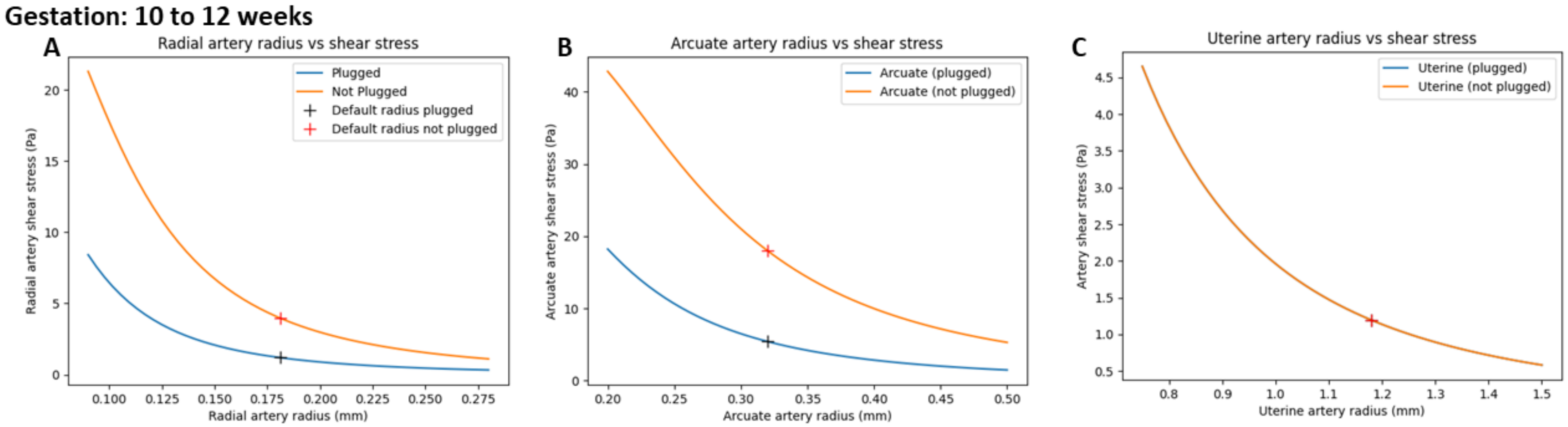

Figure 14: Plots of the relationship between artery radius and shear stress for plugged and unplugged cases for the 10-12 week gestational stage model. A) This plot is at the radial artery level B) This plot is varying radius at the arcuate arteries C) This plot is varying uterine artery radius. The measured radius values are also shown on the plots, labelled as default (+).

Gestation: 16 to 18 weeks

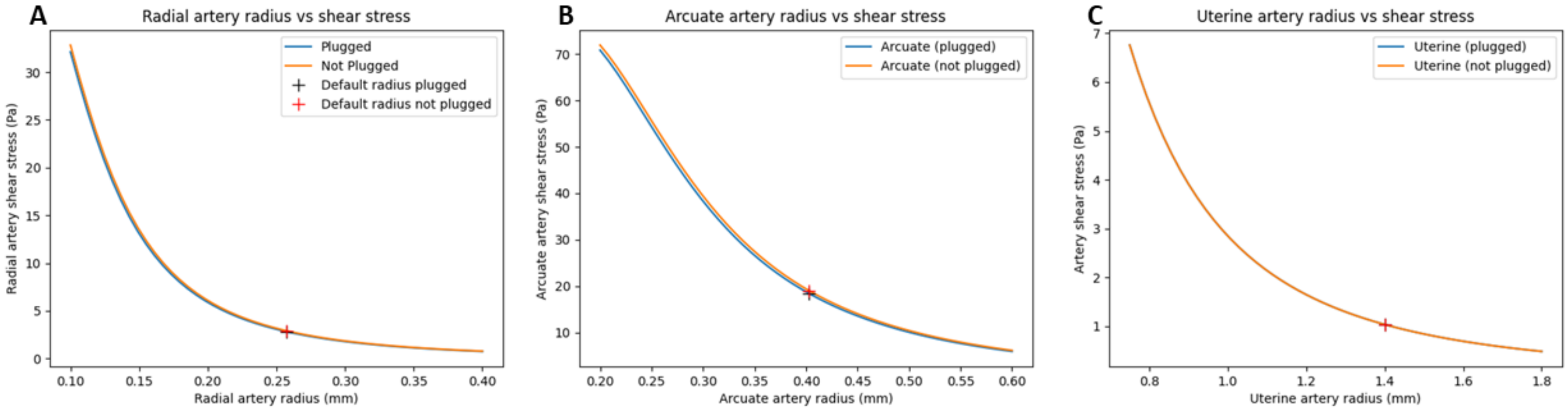

Figure 15: Plots of the relationship between artery radius and shear stress for plugged and unplugged cases for the 16 to 18 week gestational stage model. A) This plot is at the radial artery level B) This plot is varying radius at the arcuate arteries C) This plot is varying uterine artery radius and how this varies shear stress. The measured radius values are also shown on the plots, labelled as default (+).

3.7.2 Plug porosity

While the previous section contained a comparison between the shear stress in the presence and absence of trophoblast aggregates in the upstream arteries, this section investigates the parameters which define the section of spiral arteries invaded by trophoblast cells. A sensitivity analysis was also conducted on porosity, the amount of free space in the trophoblast plug. Figure 17A, B and C show plots of shear stress in the radial arteries for a range of porosity values across the three gestational models. In the 6 to 8 weeks of gestation scenario (Figure 17A), an unplugged scenario creates a 0.6 fold increase in radial artery shear stress compared to the plugs of physiological porosity (default). For the 10-12-weeks weeks of gestation, the model predicts a 2.4 fold increase in radial artery shear stress for an unplugged scenario compared to plugs of physiological porosity (Figure 17B). At 16 to 18 weeks gestation (Figure 17C), when trophoblast aggregates in the spiral arteries is minimal and the channel for flow is well established, the unplugged scenario only shows a negligible increase in radial artery shear stress compared to the scenario containing trophoblast aggregates.

.

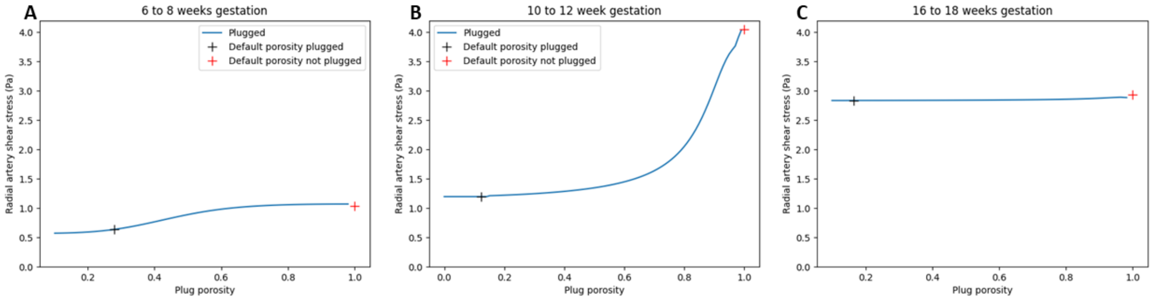

Figure 17: Sensitivity analysis for plug porosity in the human models of uterine circulation, predicting shear stress in the radial arteries for a range of plug porosities. A) 6-8 weeks of gestation model with points for the plugged and unplugged scenarios. B) 10-12 weeks gestation model. C) 16-weeks model of gestation.

3.7.3 Channel Radius

Another parameter defining the trophoblast plugs in the network models of uterine circulation is the radius of the clear channel which is observed to form through the trophoblast plugs from 10-12 weeks (Allerkamp et al. 2021). The addition of a function to capture flow through a clear channel with porous surrounds in this model reflects this observation in the anatomy, for which the measurements have not yet been assessed. Figure 11 depicts the remodelled spiral arteries as represented by functions in the model. At 6-8 weeks of gestation, no channels are observed, and the trophoblast plug can be represented by a section of porous plug. The plugged section has already been remodelled to a wider radius than the upstream section of artery and a funnel function is used to ahead of the plug to represent this. By 10-12 weeks a channel has been observed so a function for a clear channel with porous surrounds represents the plugged section. At 16-18 weeks gestation, the vessels have further remodelled to a wider lumen, the channel has grown and the remaining trophoblast aggregates are condensed towards the vessel wall.

Figure 18 demonstrates how the radius of the clear channel changes the predicted shear stress in the radial arteries for a set adjusted porosity (porosity measured with the exclusion of the area defined as channel). First, it was assumed that the plug retains the same density of cells (constant porosity) and a range of channel width from 0 mm to the spiral artery radius (effectively no plug aggregates) was assessed. A widening channel radius might represent trophoblast aggregate being pushed out of the way as blood flows through the channel. For low values of porosity (densely packed aggregates) the whole region is effectively impermeable to flow. This was assessed in the model, and for porosity values lower than 0.15, the solution to a channel model with impermeable walls is equivalent to the channel model with a porous region surrounding it. For the 10-12 weeks model, the adjusted porosity value is 0.123, lower than the threshold of 0.15, and so flow is approximated by flow through a tube (equations 3 and 4). For the 16-18 weeks of gestation model, a higher adjusted porosity is measured averaging to 0.164. As a comparison, this section of artery could also be approximated as a fully plugged section with porosity taken as the area porosity value (includes the channel space as part of the total void space). For the 16-18 week model, for a section of artery with trophoblast aggregate density equivalent to the area porosity, predicted shear stress at the radial arteries to be approximately 30% less than the approximation of a clear channel with porous surrounds at the adjusted porosity value.

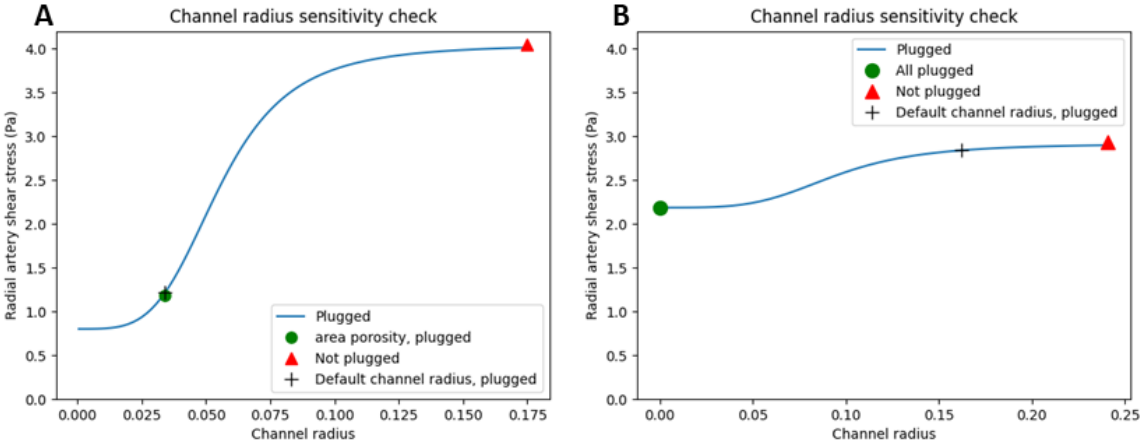

Figure 18: A graph of the relationship between the channel radius and the shear stress in the radial arteries over a range of channel radius values. Additional points plotted capture the average measured channel radius with adjusted porosity, a porous plug with area porosity and a clear tube with no plug medium, A) Plot for 10-12 weeks gestation B) Plot for 16-18 weeks gestation.

Flow proportions through clear channel and porous surrounds

For the section of spiral arteries that contains trophoblast plugs with a clear channel for flow, the proportion of flow through the channel is compared to the flow through the porous cellular surrounds (Figure 19). Flow through the channel dominates except at very small channel radius values. At the higher end porosity values (when the plug contains a lot of empty space), flow trends towards the porous surrounds (Figure 19). At the physiological values of channel radius and porosity, the clear channel dominates blood flow.

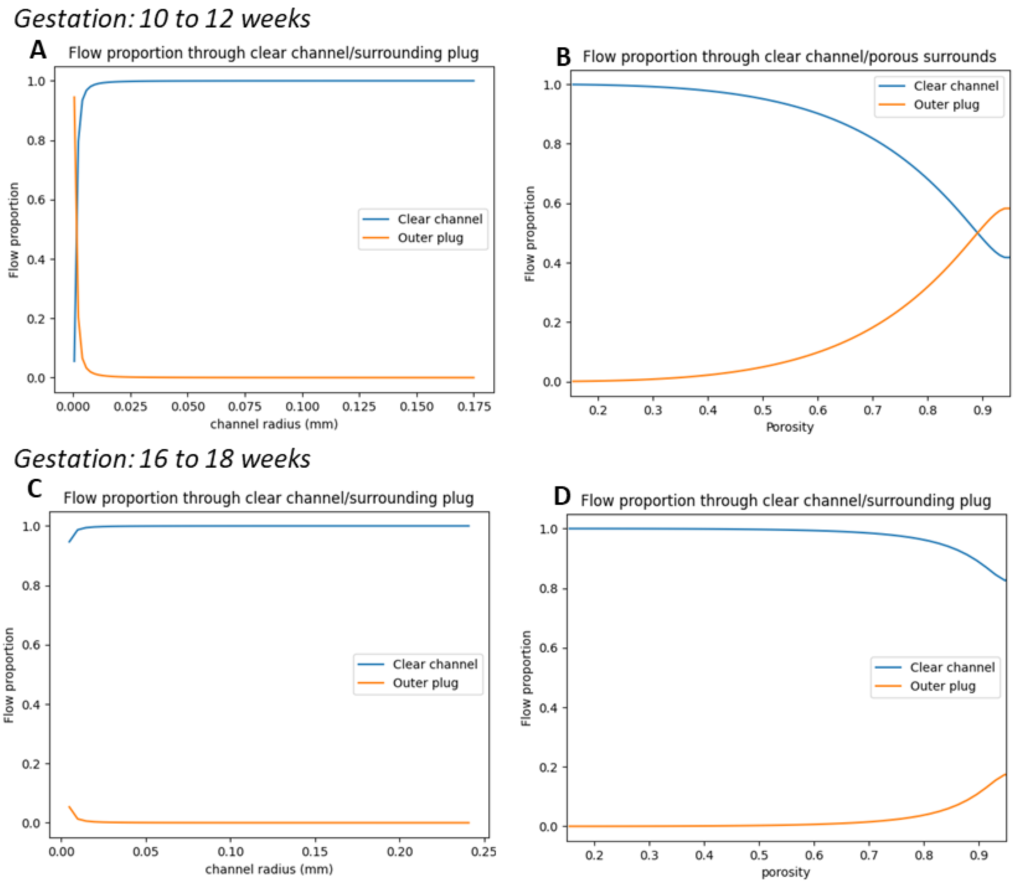

Figure 19: Graphs of the proportion of flow through the clear channel and porous surrounds over range of channel radius and porosity values. A) Plot of channel radius from 0 to the outer spiral artery radius for 10-12 week gestational stage. B) Plot of relationship between porosity of porous surrounds and flow proportion for 10-12 weeks gestation. C) Plot of channel radius from 0 to the outer spiral artery radius for 16-18 week gestational stage. D) Plot of relationship between porosity of porous surrounds and flow proportion for 16-18 weeks gestation.

The analysis displayed in Figure 19 tests the full range of channel radius and porosity values. However, channel radius and porosity are most likely not independent. Indeed, observations of spiral artery anatomy suggest that as the channel grows, the trophoblast aggregate coalesces towards the vessel wall, decreasing the associated porosity. To better represent this relationship, the total void space (and so the total volume of trophoblast within a spiral artery) was calculated for the measured porosity and channel radius values. The void space was then kept constant, and the possible variations of clear channel radius and the porosity of porous surrounds were calculated. A range of channel radius and porosity values were able to be modelled without a change in volume of trophoblast aggregates (Figure 20). For 10 to 12 weeks of gestation, with a constant void space, the maximum channel radius is 0.077mm and the maximum porosity value is 0.19. The average measured value lies between these two points. For 16 to 18 weeks of gestation (Figure 20B), the measured anatomical geometry trends towards the maximum radius for this void space. That is, the cells at this gestation are maximally packed, likely pushed to the side through flow in the channel.

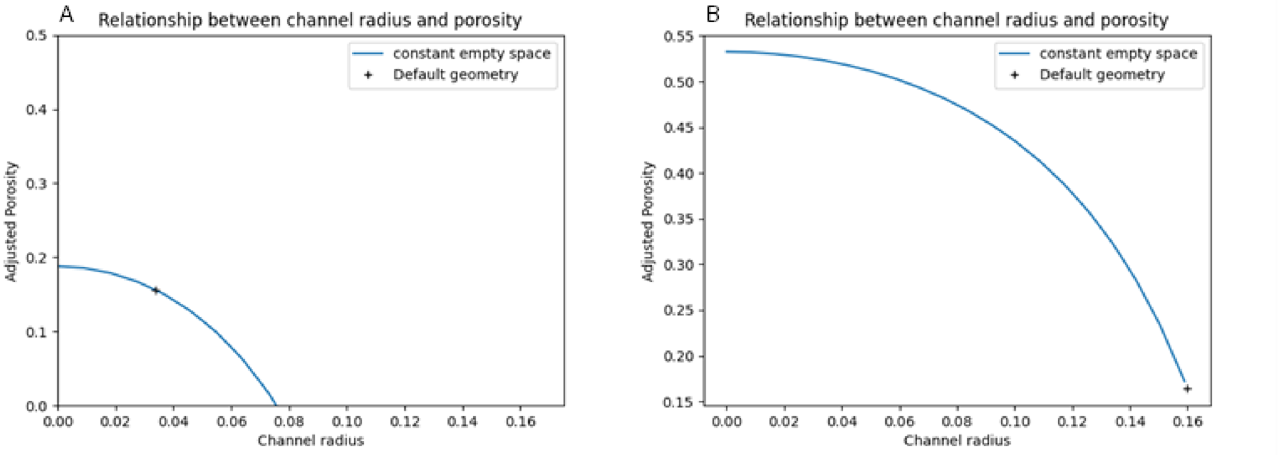

Figure 20: For a constant void space, the relationship between channel radius and associated adjusted porosities were plotted. A) 10 to 12 weeks of gestation and B) 16 to 18 weeks of gestation.

Within the bounds of valid solutions for a constant void space the flow proportions were calculated for the clear channel and porous surrounds. For the 10-12 weeks of gestation model, flow through the clear channel dominates (Figure 21A&C). For model at 16-18 weeks, at small channel radius values and high porosity values, flow through the porous surrounds is dominant. Flow through clear channel begins to dominate over the porous surrounds at a radius as small as approximately 0.01mm. Physiologically, as the channels start to form, the modelling shows that they likely dominate haemodynamics. Regardless of the gestation, blood flow through the plugged region is very small and it acts as a bottleneck to flow through the clear channel. This finding matches the observations in anatomy, where large channels are observed, and trophoblast aggregates are densely packed towards the vessel wall.

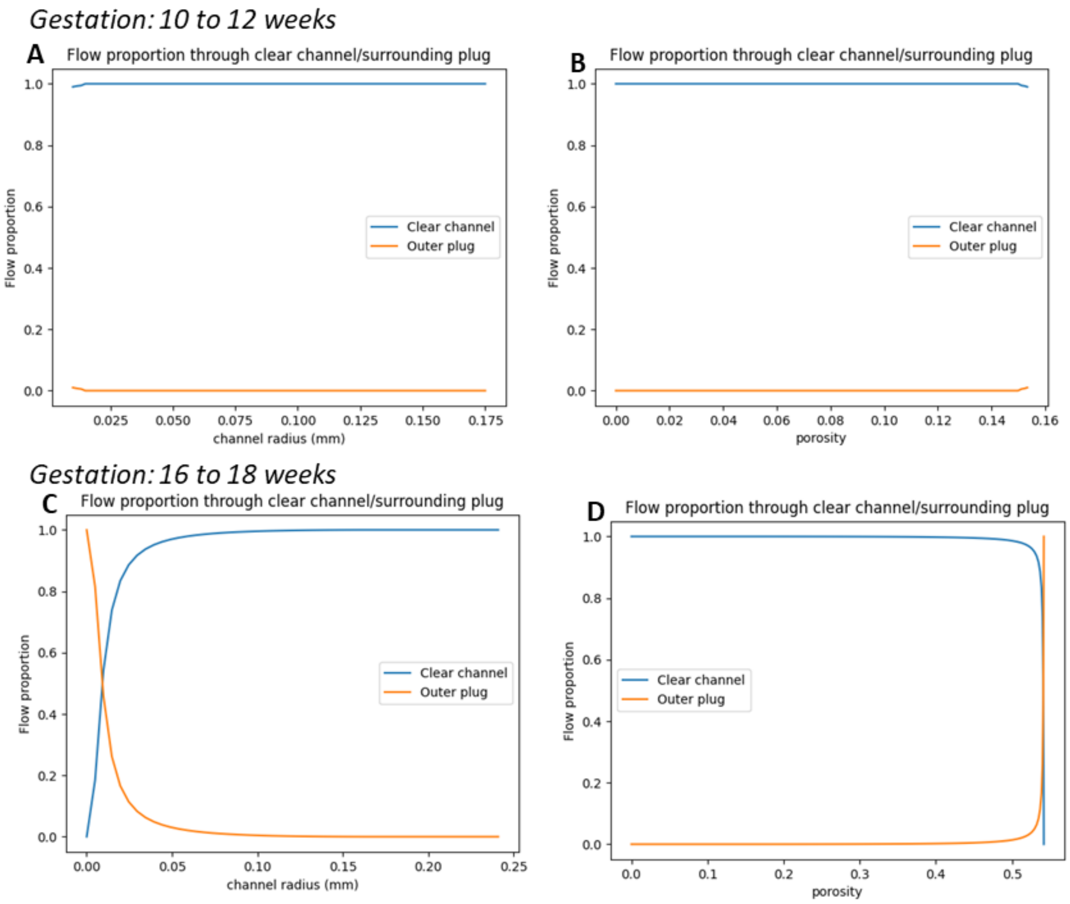

Figure 21: Flow proportions through the clear channel and porous surrounds for a constant void space. A) Channel radius values for 10-12 week gestations. B) Porosity values for 10-12 weeks gestation. C) Channel radius for 16-18 weeks gestation. D) Porosity values for 16-18 weeks.

3.7.4 Plug length

The depth of trophoblast invasion has been identified as a factor contributing to conditions such as pre-eclampsia and FGR (Meekins et al. 1994). However, plug length has rarely been measured in the literature. Allerkamp et al. were able to measure plug length in histological samples of gravid uteri with placentae in situ, and this new anatomical data allows us to better assess the influence of plug length on uterine blood flow (Allerkamp et al. 2021). Plug length was varied to determine the impact on shear stress at the radial arteries in the three models of gestation (Figure 22). Overall, the measured anatomically (average of 1.3 mm for 6-8 weeks, 1.4mm for 10-12 weeks and 3mm for 16-18 weeks) appear to be sufficiently long to reduce flow (and shear stress) by 0.6 fold in the 6-8 week model and 2.3 fold in the 10-12 week model (Figure 22 A&B). Plug length did not change shear stress values in the 16-18 weeks model (Figure 22C). At this stage of gestation, the channels through the plugs are well established meaning the plugs have a less significant effect on the haemodynamics.

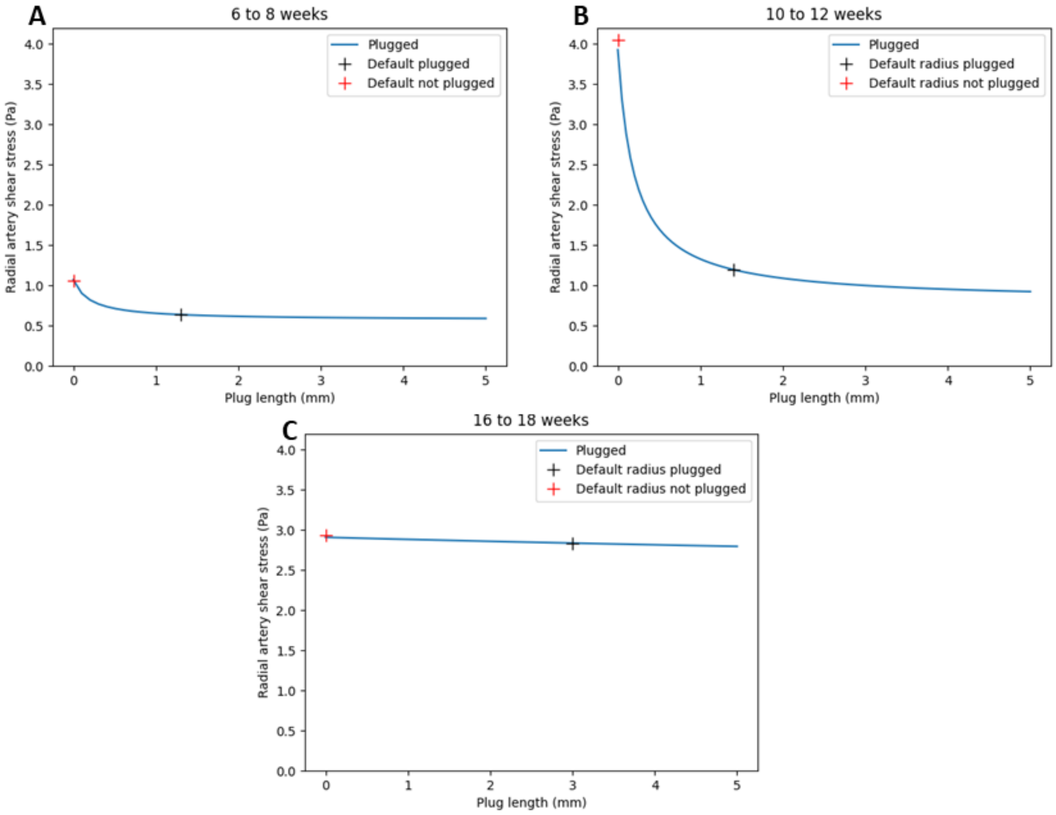

Figure 22: Sensitivity analysis on trophoblast plug length with points marked 'default' for the physiological radii and plug lengths. A) 6 to 8 weeks. B) 10 to 12 weeks. C) 16 to 18 weeks.

3.7.5 Rat as a model for human anatomy

To use rat anatomy as an analogue for human data, the shear stress predictions from the existing models were compared. As rat data is acquired at near-term, an existing term model of the human anatomy is also simulated (Clark, Alys et al. 2018) assuming all spiral artery plugging is dispersed, and the spiral arteries can be represented as a funnel geometry (Burton, G. J. et al. 2009). Rat models of uterine circulation for the virgin and pregnant states were used to predict shear stress values in the radial arteries relative to their measured size, and these were then compared to the models of human uterine circulation. The models radius and shear stress predictions were plotted to better understand how different stages of human pregnancy correlate in relation to shear stress exposure upstream and the corresponding impacts on remodelling When comparing shear stress values for the different human and rat models, relative to radius as a % of physiological size, the human gestation curves are initially lower than the rat models (Figure 23A). For the human model at term, the rat and human curves are more comparable (Figure 23A). When comparing the shear stress values as a percentage of the value predicted for the physiological radial artery radius, there is greater crossover across all the models (Figure 23B). While there is some divergence at smaller radius values, there is sufficient cross over at 100% of physiological size (Figure 23B).

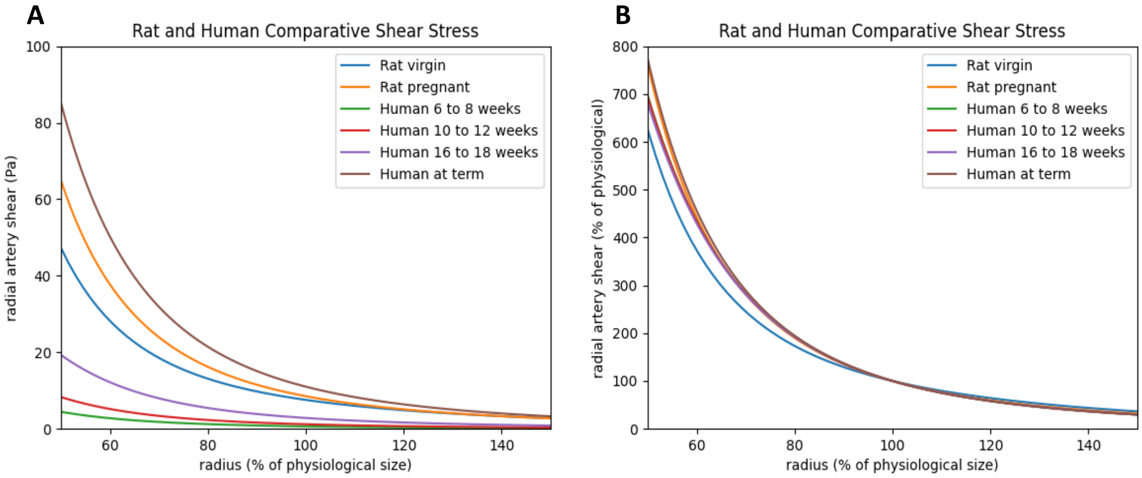

Figure 23: Two plots relating vessel radius relative to measured physiological size to shear stress for non-pregnant and pregnant rat and human gestation stages 6-8 weeks, 10-12 weeks, and 16-18 weeks and an at term model. A) radius as a % of physiological size relative to shear stress B) radius as a % of physiological size relative to shear stress as a % of physiological size.

3.8 Discussion

In this chapter, three network models of the human uterine circulation spanning the first half of pregnancy were parameterised, with detailed measurements available for vessel geometries and plug characteristics. A sensitivity analysis was carried out to establish which of these anatomical attributes has the greatest functional impact on flow and shear stress in the larger uterine vessels – the radial, arcuate and uterine arteries. Finally, models of the rat uterine circulation, non-pregnant and pregnant, were also presented to help with comparisons between the species.

Once parameterised, an analysis of model sensitivity for key parameters relating to uterine vascular structure and spiral artery plugging was conducted. Flow and shear stress predicted by the model in the arteries upstream of the plugs was used as a prediction of interest to understand how spiral artery plugging relates to function in these upstream arteries. This is important as plugging may either promote or impair the uterine vasculature from remodelling effectively. Relative to the unplugged state, the shear stress predictions in the radial and arcuate arteries were lower in the presence of trophoblast plugs when compared to predictions in their absence, but only in early gestation. In the 6-8 week and 10-12 week model the resistance of the plug is significant, and so it impedes flow toward the IVS, as well as the total resistance of the blood vessels feeding the placenta. Together, this provides an expected low flow environment at the placenta (James, Chamley, and Clark 2017). Early in gestation the placenta is still forming the delicate villous structures and their development is impaired by high maternal flow rates through the IVS which could have longer term impacts on placental sufficiency (James, Chamley, and Clark 2017).

By the 16-18 week gestation model, the plugs have established channels that are large enough that (volumetric) flow is not significantly impeded, therefore more flow is passing through and the spiral arteries have less significance in the network. At this later stage of gestation, the outward remodelling of the vessels upstream of the spiral arteries has a greater significance, in line with observations of significant flow to the IVS by this stage of gestation (James et al. 2018). In this analysis, the size of the radial and arcuate arteries was treated independently however, they are likely linked and inform one another. The measurements obtained by Allerkamp et al. (Allerkamp et al. 2021) suggested that arcuate and radial arteries remodel on similar temporal scales suggesting they should not be handled individually.

As gestation progresses beyond the 6-8 week mark, plugs within the spiral arteries begin to show signs of channels and eventually the plugs are expected to breakdown. Clear channels have been observed through the plugs and progressively increase in size with gestation. At 10-12 weeks of gestation and 16-18 weeks of gestation, the trophoblast aggregates coalesce towards the vessel wall and a clear channel for flow is observed. The two variables characterising flow through this section of the network are porosity and channel radius. For the channel function, the flow split calculations of the flow through clear channels compared to the porous surrounds, supports that they are the dominant pathway for flow. For the values measured by Allerkamp et al. taking into account the clear channel (adjusted porosity) (Allerkamp et al. 2021), the porous medium is sufficiently packed that it acts more as a bottleneck for flow. Analysis of these channels, which have been observed to form through the plugs, provided insight into the point in gestation where the plugs begin to break down, and other parts of the system may begin to dominate haemodynamics. The channel starts off small and as gestation progresses these channels are observed to widen (Allerkamp et al. 2021). The porous surrounds are sufficiently dense to limit the flow through the plugged portion of the vessel. Rather than flow through a porous medium, they can be better approximated as a bottleneck for flow. While the exact adhesion molecules that bind cells to each other in the plugs, or the resulting phenotypic/mechanistic changes that lead to their dispersal remain unknown, prior agent based modelling from Saghian et al. proposed channels forming in the plug which progressively expand with increasing flow (Saghian et al. 2019). Observations in the anatomy from Alkerkamp et al (Allerkamp et al. 2021) is of a progressive breakdown of trophoblast plugs through the formation of channels. The modelling here supports these by demonstrating that the observed channels act as bottleneck pathways for flow that gradually widen. Depending on the upstream vessel sizes, the flow could be limited by a point located further upstream, perhaps at the radial artery level, as these vessels have been shown to remain smaller for longer than the spiral arteries (Allerkamp et al. 2021).

The average plug length measured is sufficiently long so as to reduce shear stress in the upstream arteries by 0.6 fold relative to if there were no plug for 6-8 weeks and 2.4 fold for 10-12 weeks, but not at the 16-18 week gestation. If plugs were shorter than this, it is possible that upstream shear stress would be higher than expected, altering the conditions for these vessels to remodel. This increase in shear at plug lengths below the average is most pronounced at the 10-12 week gestational stage. James et al considered how trophoblast plug length impacts the shear stress in the spiral arteries (James et al. 2018). In this thesis, new anatomical data was incorporated into the modelling (James et al. estimated plug length >0.1m was required to restrict flow (James et al. 2018)) and considered arteries upstream of the spiral arteries by predicting shear in the radial, arcuate and uterine arteries.

Comparing the three models of gestation presented, the plug parameters seemed most influential in the 10-12 week model. For the 6-8 week model of gestation, it could be that the vessel lumens in the network are not large enough to carry any extra flow, such that, while the plugs may limit blood flow through the IVS, in the absence of plugs, the flow through the network would remain relatively unchanged. For the 10-12 week model, outward remodelling has progressed to widen vessel lumens such that, in the absence of plugs here, a marked increase in flow and predicted shear stress is observed. Once pregnancy has progressed to 16-18 week stage, the plugs are no longer considered as significant in the system, and further changes will be dependent on outward remodelling of the vessels.

The models presented in Chapter 3 are limited to the first half of pregnancy. In relation to UtA Doppler ultrasound, a clinical screening test, where the reflected notch (as a possible indication of preeclampsia) is not usually observed beyond 20 weeks gestation (Clark, Alys et al. 2018). Most of the remodelling happens over the first half of pregnancy, with the most marked increase in vessel lumen and the reshaping of spiral arteries through trophoblast invasion (Allerkamp et al. 2021). Although the models are limited to the first half of pregnancy, they are sufficient to draw connections between the uterine vasculature being investigated and UtA Doppler waveform interpretations. When the “notch” is observed beyond 20 weeks of gestation, this can indicate a high resistance in the uterine arterial network with links to FGR and preeclampsia (James, Chamley, and Clark 2017). Assumptions in the models are that blood flow is laminar and Newtonian. These assumptions hold sound for the vessel sizes in these models. Another simplification made is that the vessels are taken as straight and fixed when known to be tortuous and compliant. Vessels within the same level are assumed to be the same when biological variation exists. The models presented are at steady state. A study by Saghian et al looked at the pulsatile flow at the spiral arteries and concluded that a steady state approximation of the system is accurate as the Strouhal and Womersley numbers are small (Saghian et al. 2017).

Rat models provide a useful tool for gaining insight into uterine circulation and the remodelling process. The shear stress values predicted for the human models of uterine circulation are comparable to the rat models for the purposes of this study. Rat vessels are typically smaller than human, so it is important to consider the vessel size when comparing values. When shear stress predictions are taken relative to physiological size, the human and rat models are comparable within physiological ranges (Figure 23). The rat models presented are for two states of non-pregnant and pregnant (late-stage), while the human models span across the first half of gestation with the addition of a term model for comparison.

Trophoblast invasion of spiral arteries transforms these vessels into stiff, wide bore funnels, while the other arteries in the uterine circulation are compliant and respond to changes in pressure and flow by either dilating or constricting. Radial arteries in rats showed a constriction response at higher pressure and flow rates (Allerkamp et al. 2022). If shear stresses and flow rates (proportional variables) are higher than expected in the upstream arteries due to insufficient trophoblast plugging, then these arteries may remodel around a different set point. The network models presented so far consider the models as a single fixed geometry. The vascular reactivity response vessels, specific to those in the uterus, will be explored in the following chapter.

Chapter 4 – Incorporating vascular reactivity into a model of uterine circulation

The models presented in Chapter 3 use a rigid vessel approximation with the assumption that there is no significant vessel dilation or contraction in response to stimuli. In reality, blood vessels respond to the stimuli of flow and pressure by either constricting or dilating to maintain sufficient flow and control high pressure events. Chapter 4 builds on the utero-placental network models by incorporating a model of vascular reactivity (the response to any given stimulus).

4.1 Background

Mathematical models of vascular reactivity are of importance to the field of cardiovascular biomechanics, as every vessel in the human body is dynamic and adapts its radius in response to changes in blood pressure, flow, metabolic availability, and hormones. There are multiple different mathematical approaches to understanding this reactivity (see, for example a review by Namani et al. (Namani et al. 2020)) which scale models of isolated vessels to vascular networks and organ scaled models. Blood vessel autoregulation can be broken down into different components, which combine to give the overall response; passive vessel mechanics (intrinsic to the structure of the vessel); and an active response (which relates to smooth muscle contraction). The active response itself can be broken down into a myogenic response (a change in the vessel size due to pressure or stretch), a shear-dependent response, and other responses such as metabolic response. Typically, models of vascular reactivity have been derived from ex vivo pressure or wire myography experiments, where individual vessels are tested by measuring diameter changes over a range of intraluminal pressures. The testing environment (vessel conditions) are altered to induce these different responses and produce characteristic pressure and diameter curves (Carlson and Secomb 2005; Carlson, Arciero, and Secomb 2008). A commonly used model of vessel response to stimuli was derived by Carlson and Secomb (Carlson and Secomb 2005), who looked to understand the response of a number of systemic blood vessels of various sizes and who showed relationships between vessel size and the parameters that define vessel reactivity. The group later adapted this model to include metabolic and shear responses (Carlson, Arciero, and Secomb 2008).

Vessels that make up the uterine vasculature undergo a remodelling process during pregnancy in which vascular reactivity is altered (Osol, Ko, and Mandalà 2019). Allerkamp et al. developed an understanding of systemic vessel autoregulation by fitting the model to data from pressure myography experiments conducted on rat radial arteries, generating the first uterine-specific model of vascular reactivity (Allerkamp et al. 2022). They considered rat arteries from non-pregnant (virgin) and pregnant rats toward the end of their gestational period. First, the passive vessel mechanics (the impact of the vessel wall structure) were studied by bathing the vessel in a calcium free solution (Allerkamp et al. 2022). The absence of calcium means the constriction response of smooth muscle cells is disabled as it is a calcium mediated pathway (Allerkamp et al. 2022). The active response of the vessel was measured experimentally by first increasing pressure in a step wise fashion with no added flow (Allerkamp et al. 2022). Flow was then introduced by slowly increasing the pressure drop across the vessel in a step wise fashion (Allerkamp et al. 2022). Vessels that make up the uterine vasculature undergo a remodelling process during pregnancy in which vascular reactivity is altered (Osol, Ko, and Mandalà 2019). The experiments conducted by Allerkamp et al. (Allerkamp et al. 2022) were carried out in non-pregnant rat vessels and pregnant vessels to assess the influence of hormones and paracrine factors in the uterine microenvironment (these include progesterone, estradiol, placental growth factor and vascular endothelail growth factor) on this vascular reactivity (Figure 24).

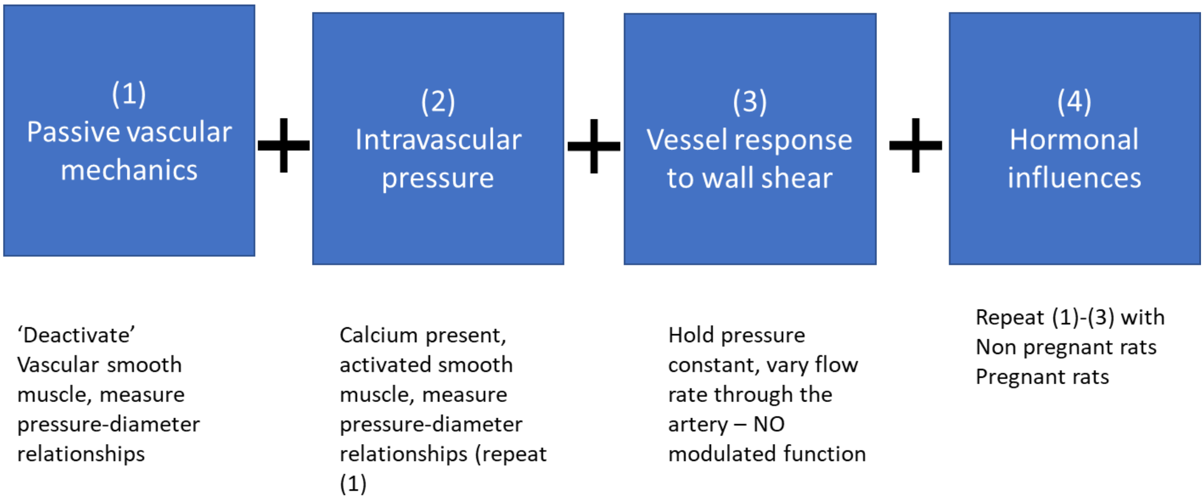

Figure 24: Flow diagram of the pressure myography experiments conducted for rodent radial vessels to obtain pressure and diameter responses for the different components of vascular reactivity (Adapted from 2021-JMBBM-AlysClark - Presentation).

4.1.1 Parameterisation of the Rat Model of Compliance

Combining mathematical models of vascular reactivity, based on prior work by Carlson and Secomb, with the results from ex vivo pressure myography data for rat radial arteries, enabled Allerkamp et al. to parameterise a computational model for isolated vessel behaviour (Allerkamp et al. 2022). By comparing their experimental results (collected from rat radial arteries) to the systemic vessels analysed by Carlson and Secomb, they were able to assess how uterine specific arteries compared to systemic vessels of a similar size (Allerkamp et al. 2022; Carlson and Secomb 2005). They were also able to compare the pregnant and non-pregnant rat radial arteries which provided insight into how pregnancy alters vascular reactivity as part of the remodelling process (Allerkamp et al. 2022).

The modelling results from Allerkamp et al. for rat radial arteries showed that the passive vessel response was comparable to systemic vessels of a similar size, and the changes during pregnancy are in line with the increase in vessel size seen in pregnancy (Allerkamp et al. 2022). For the active response but no flow, radial arteries show a response which is different to equivalently sized systemic vessels. Non pregnant rats had a relatively high active tension (defined by Carlson and Secomb as the sum of elements that represent vessel wall response, a passive non-linear spring and an active contractile unit (Carlson and Secomb 2005)) which reduces with pregnancy. Non-pregnant rats had a lower myogenic response (how smooth muscle cells respond to intraluminal pressure) than would be expected for a vessel of this size, and pregnancy further reduces this value (Allerkamp et al. 2022). These differences in parameter values mean that non-pregnant radial arteries have a consistent active tone and a lower myogenic tone (% decrease between passive and active parameters) such that, at higher pressures, the active vessel response dominates over the myogenic constriction. Pregnancy alters the vessel autoregulation response, more in line with equivalent systemic vessels and the vessels are able to tolerate higher flow rates if they adapt adequately to pregnancy (Allerkamp et al. 2022).

Allerkamp et al. also considered the impact of flow through a vessel, with an aim to replicate in vivo conditions (Allerkamp et al. 2022). To do this they used a simplified version of the rat network model presented in Chapter 3 to determine blood flow in a rat radial artery in the non-pregnant and pregnant scenarios. In the non-pregnant scenario they considered active response with no flow, and the additional effect of flow rates of 5 and 10 uL/min. In the pregnant case they considered higher flows at 50 and 0 uL /min. The passive model shows an continually increasing diameter in response to increasing pressure. While the active model has an initial increasing diameter in response to pressure, there is also a second phase of vessel constriction at higher pressures. With increasing flow through the vessel, this constriction response counters the passive response, which is to increase diameter with flow, and instead reduces diameter to a greater degree for higher flow conditions (Allerkamp et al. 2022, H72-H88). They showed that presenece of flow through these vessels dampens the increase in diameter in response to increasing transmural pressure. However, changes in flow, pressure, and diameter are all interelated in vivo and to understand these relationships arteries can not be considered in isolation. Therefore a network model which takes into account vascular reactivity is needed.

4.2 Methods

In this Chapter, the models developed in Chapter 3 are used as a basis to investigate the influence of vascular reactivity on whole system function. Model geometries, and the governing equations for flow and pressure within the network are as described in Chapter 3. Here, two models of vascular reactivity are introduced: 1) a simple model that describes the radius of a vessel as a linear function of transmural pressure, and 2) a more complex model based on the findings of Allerkamp et al. (Allerkamp et al. 2022), which includes how the passive, active and shear dependent responses of vessels contribute to the relationship between vascular radius, pressure and blood flow within a vessel. The vascular reactivity in a network model relates directly to anatomical and vascular reactivity for rats in non-pregnant and late-pregnant conditions. However, no measurements exist that define the evolution of vessel reactivity across pregnancy. In humans, it is not possible to measure this vascular reactivity, so model parameters must be inferred from those determined in rodents. As the human models reflect an evolution in anatomy in early pregnancy, it is assumed that early pregnancy (6-8 weeks) is more like the non-pregnant rat than the near-term rat, and that mid-pregnancy (16-18 weeks) is more like the late-pregnant than the non-pregnant rat. However, this remains to be tested.

4.2.1 Compliance models

Linear compliance: A simple model of vascular reactivity is to approximate a linear relationship between radius and pressure by a factor α.

$$r = r_0(1 + \alpha P_{out})$$

(17)

where r_0 is the initial radius, α is a compliance constant, and P_{out} is transmural pressure, defined as the difference between the external pressure on the vessel and the pressure within the vessel. For this model, an assumption is made that the external pressure is fixed such that the vessel radius changes in response to blood pressure only. This function enables the vessels to respond to local pressure changes by a factor of α and is a commonly used relationship to describe the compliance of a vessel in the literature (Clark, A. R. et al. 2011; Krenz and Dawson 2003).

From a plot of the pressure myography experimental data for rat radial arteries, a slope relating change in inner diameter to change in intraluminal pressure was extracted. This relationship was then used to define the compliance constant α.

Vascular reactivity model: A mechanical representation of the vessel wall which can be used to link vessel diameter, intraluminal pressure, and model parameters was developed by Carlson and Secomb (Carlson and Secomb 2005; Carlson, Arciero, and Secomb 2008). Allerkamp et al. expanded upon Carlson and Secomb's model to develop a uterine-specific model of rat radial artery function, based on active and passive pressure myography data of pregnant and non-pregnant rat vessels (Allerkamp et al. 2022).

To describe a vessel wall under tension, 'total tension' (T_{tot}) is defined as a combination of passive response (non-linear spring) and a contractile element.

$$T_{tot} \; = \; T_{pass} \; + \; AT^{max}{}_{act}$$

(18)

where T_{pass} is passive tension, A is the activation (level of VSM tone), and T_{act}^{max} is the maximal active component of tension.

From observations in pressure myography (where pressure and diameter are measured), the response to pressure by changing diameter is related to tension through Laplace's law.

$$T_{tot} = \frac{PD}{2}$$

(19)

where P is transmural pressure, and D is vessel diameter.

The passive component is derived from measuring passive pressure-diameter relationships (i.e the relationship between pressure and diameter when there is no active contraction of the vessel, or in the experimental context no calcium available). At low pressures, the relationship is relatively linear and plateaus at higher pressures. Equation 17 represents the simplest way to reflect a passive response, but there are several models for passive tension available in the literature. A typical non-linear relationship for passive tension can be defined as an exponential, depending on D (the vessel diameter),

$$T_{pass} = C_{pass} exp\left(C'_{pass}\left(\frac{D}{D_0} - 1\right)\right)$$

(20)

where D is the diameter of the vessel, D_0 is passive diameter of the vessel at a pressure of 100mmHg, C_{pass} is passive tension at diameter D_0 and C'_{pass} is the steepness of the exponential curve.

The maximal active tension (T_{max}^{act}) is the maximal active tension a vessel can generate. The definition of this quantity used in previous modelling studies was based on observations in skeletal muscle and follows a Gaussian curve.

$$T_{max}{}^{act} = C_{act} exp\left(-\left(\frac{\frac{D}{D_0} C'_{act}}{C''_{act}}\right)^2\right)$$

(21)

Where the parameter C_{act} controls maximum tension (represents peak magnitude), C'_{act} controls which diameter the peak occurs (relative peak location) and C''_{act} controls curve width.

Smooth muscle activation, A, is assumed to depend on stimulus (S_{tone}) in a sigmoidal relationship and incorporates the myogenic tone.

$$A = \frac{1}{1 + e^{-S_{tone}}}$$

(22)

Based on previous models of isolated vessel response, the active contributions to autoregulation can be grouped by the nature of the response (i.e. myogenic response (pressure dependent), shear-dependent) (Carlson et al. 2008). The total active response can be captured by S_{tone} (an active stimulus) and the following linear relationship, fitted to the experimental data (Carlson, Arciero, and Secomb 2008), particularly where individual mechanisms can be experimentally investigated one by one

$$S_{tone} = S_{myo} + S_{shear} + C'_{tone} = C_{myo}T - C_{shear}\tau + C'_{tone}$$

(23)

Here, S_{myo} is myogenic tone, S_{shear} is shear dependent tone, C_{myo} is a parameter that controls the strength of the myogenic response, T is wall tension, C_{shear} controls the constricting response to shear, τ is shear stress at the vessel wall and C'_{tone} is a constant that represents an inherent tone (or mechanisms that cannot be captured by the experimental investigation). This typical relationship assumes that any increase in shear stress is dilatory.

Allerkamp et al. (Allerkamp et al. 2022) noted that uterine radial arteries, consistent with some other small arteries, have no response to shear at low shear stress, followed by a constrictive response at increasing shear stress, and a dilatory effect at higher shear stresses. They modified the shear stress component of S_{tone} to reflect this.

$$S_{shear} = \left\{ \begin{array}{cc} 0, & if\ \tau < \tau_1, \\ C_{shear}(\tau - \tau_1), & if\ \tau_1 < \tau < \tau_2, \\ -C'_{shear}\left(\tau - \left(\frac{C_{shear}}{C'_{shear}}(\tau_1 - \tau_2) + \tau_2\right)\right), & if\ \tau > \tau_2 \end{array} \right\} \tag{24}$$

τ_1 is the shear stress when VSM tone begins to increase. As shear stress increases, τ_2 defines the shear stress beyond which the VSM tone decreases with increasing shear stress. For a very low shear value, there is no change to tone. C_{shear} controls the constriction response while C'_{shear} controls the relaxation response (Allerkamp et al. 2022)(Allerkamp et al. 2022, H72-H88) .

4.2.3 Model Parameterisation for rats

The model for vessel autoregulation defined here contains parameters relating vessel diameter to intraluminal pressure for 1) the passive response, 2) the active response (pressure, no flow) and 3) the shear dependent response (flow) (Carlson, Arciero, and Secomb 2008). Allerkamp et al parameterised this model of vessel autoregulation for rat models 1) non-pregnant and 2) pregnant (late-term), based on experimental data (Table 6) (Allerkamp et al. 2022).

Table 6: Parameters for models of vessel autoregulation for rat radial arteries(Allerkamp et al. 2022).

Parameter	Description	unit	Rat	
			Virgin	Pregnant
D_0	passive diameter of the vessel at a pressure of 100mmHg	µm	93.59	155.71
C_{pass}	passive tension at 100mmHg	N.m	0.622	1.035
$C_{passdash}$	steepness of the exponential curve describing passive tension	no unit	7.26	6.24
C_{act}	maximum active tension	N.m	4.392	1.099
C'_{act}	controls diameter of peak active tension	no units	0.99	0.766
C''_{act}	controls width of Gaussian curve defining active tension	no units	0.181	0.18
C_{myo}	controls strength of myogenic response	m/N	0.01	0.01
C'_{tone}	a constant parameter	no units	-6.69	-7.15
C_{shear}	controls smooth muscle tone in constriction response to shear	1/Pa	0.0797	0.0772
C_{Shear1}	controls smooth muscle tone in relaxation response to shear	1/Pa	0.045	0.3035
τ_1	muscle tone begins to increase with increasing shear	Pa	1.67E-12	16.401
τ_2	shear stress at which smooth muscle tone begins to decrease (relax) with increasing shear	Pa	40.326	40.326

4.2.4 Model Parameterisation for humans

While vascular reactivity data in rats is not directly translatable to humans, the data provided by Carlson and Secomb showing how vessels of a particular size are expected to behave, along with Allerkamp et al.’s data on how vascular reactivity changes in pregnancy in the context of vessel size allows some ability to infer human parameters from the rat data in the of experimental pressure myography data available for human uterine arteries (Allerkamp et al. 2022; Carlson and Secomb 2005).

To infer what might happen in the human uterine vasculature in pregnancy an extrapolation was made from rodent data to human data. Carlson and Secomb identified that several parameters of the model were related to vessel size (regardless of the location in the body) (Carlson and Secomb 2005). In that study they conducted linear fits to data, but it was clear here when plotting this data that some relationships were non-linear. This was accounted for in extrapolation of human parameters. For the parameters dependent on vessel diameter (C_{pass}, C'_{pass}, C_{act} and C_{myo} with D_0), human parameters were defined to match the larger vessel lumens found in human anatomy compared with those in rats. First, Carlson and Secomb data fits were extrapolated to capture the range of human uterine vessel diameters. Parameters C'_{pass} and C_{myo} were updated with non-linear fits which offered a better match, particularly at the larger vessel sizes found in human uterine tissue, and a higher R^2 value was seen in each case compared with in previous reports (Allerkamp et al. 2022; Carlson and Secomb 2005).

As well as being dependent on diameter, the vessel response is changed by the paracrine environment of pregnancy, changing the values between the non-pregnant model and the pregnant model. This can be noted for parameters C_{act} and C_{myo} where the rat parameters do not follow the trendline for the systemic vessels. For the human models, there are three gestational models of pregnancy spanning over the first half of pregnancy. It was assumed that the 6-8 week model is closer to the non-pregnant rat model and the 16-18 week model closer to the pregnant rat model, and that the change follows a straight line trajectory over pregnancy. Parameters which are not dependent on diameter were sourced from Allerkamp et al. (Allerkamp et al. 2022). The non-pregnant values were taken for the 6-8week model and the pregnant values (influenced by paracrine environment) were used for the 10-12 week model and the 16-18 week model (Allerkamp et al. 2022).

A sensitivity analysis was then undertaken on the human parameter fits which are dependent on vessel diameter (D_0, C_{pass}, C'_{pass}, C_{myo} and C_{act}). Other parameters were kept constant, and a single parameter varied over the range of values relevant to those of interest. For the passive model, C_{pass} is defined as the total tension at 100mmHg, which is the pressure where diameter is D_0 (Carlson and Secomb 2005). Taking equation 24 and setting pressure (P) to 100mmHg and diameter (D) to D_0, this relationship with C_{pass} was maintained.

4.2.5 Model Solutions

With these parameterised models of vessel autoregulation, there is a relationship between transmural blood pressure, diameter and flow rate defined by equations 18 and 19. As this relationship cannot be solved directly for diameter at a given pressure/flow rate a bisection method is used to find roots to the defined equations and calculate diameters for a given vessel dependent on intraluminal pressure and flow rate through an individual vessel. The bisection method seeks solutions for diameter based on an initial "over” and “under" estimate (where one represents a positive solution to equation 18-19 and the other a negative solution). Solutions were initially sought between a 10 um diameter and a diameter of $2*D_0$. Where this was not successful using the bisection method, a sweep of possible radii was conducted to find the lowest diameter at which the solution changed sign, and the bisection method was always successful in finding a solution under these conditions (albeit less quickly due to the required diameter sweep).

4.2.6 Vessel compliance in network models of the uterine circulation

Models of vessel autoregulation were then incorporated into the vascular network models defined in Chapter 3. Introducing the compliance behaviour of radial arteries in the model, the arteries at the radial level simulate a dynamic response to pressure by either constricting or dilating. For a simple linear approximation of the radius pressure relationship outlined in section 4.1.1, a stepwise function was implemented to calculate the vessel diameter until a stable solution was found at a given pressure and flow. For the vascular reactivity model outlined in section 4.1.2, the network model was first solved to give the pressure and flow values at the radial artery level. The pressure and flow for an individual radial artery were inputted into the compliance function to calculate a new vessel diameter at these conditions. This was repeated for the passive mechanics only, active function (pressure with no flow), and adding in the shear mediated response (flow). The inlet boundary condition of input flow was then increased in a step wise fashion to assess how the vessels responded to an increase in blood flow through the system. Inlet pressure was kept constant.

4.3 Results

4. 3.1 Extrapolated human isolated vessel behaviours

In order to translate the model of vasular reactivity for rat radial ateries defined by Allerkamp et al. to the context of human models, the model needs to be paramaterised for human vessels. Given experimental data for human radial arteries is not available, parameter predictions were made based on the trends presented by Allerkamp et al. In the rat model, the parameter values D_0, C_{pass}, C'_{pass}, C_{myo} and C_{act} depend on vessel size, while the other parameters change value from the non-pregnant state to pregnant state. Projections of how pregnancy changes the vascular compliance were made by progressively changing the parameter values of D_0, C_{pass}, C'_{pass}, C_{myo} and C_{act}, starting with 6-8 week model, assumed to be closer to the non-pregnant rat model, and progressing along a predicted trajectory to 10 weeks gestation and then to the 16-18 week model, assumed to be closer in behaviour to that of the pregnant rat model. The passive parameters (C_{pass} and C'_{pass}) followed the Carslon Secomb trend projections (Figure 25A &B) with this trend extrapolated to include human physiological values. For the active parameters (C_{act} and C_{myo}), the radial arteries showed parameter values which are not only following the trend of outwardly remodelling, but they are also adapted by the paracrine environment in pregnancy. For C_{act}, the non-pregnant rat arteries started with a value lower than the Carlson and Secomb trend and the pregnant value closer to that of a systemic vessel (pink lines in Figure 25C). For Cmyo, the rat value increased in the pregnant state, rather than decreasing as would be expected with an increase in diameter. The human predictions for C_{act} and C_{myo} can be seen in Figure 25C & D in comparison to the rat model parameters (blue trajectory for human and pink trajectory for rats). Figure 25C shows the adaptation during pregnancy of the vessel's active response (C_{act}) towards a behaviour similar to that of a systemic vessel. Figure 25D, shows the pregnancy adaptation of the myogenic tone (C_{myo}) for radial arteries towards a stronger myogenic constriction response. Table 7 contains the predicted parameters for the three human models of gestation.

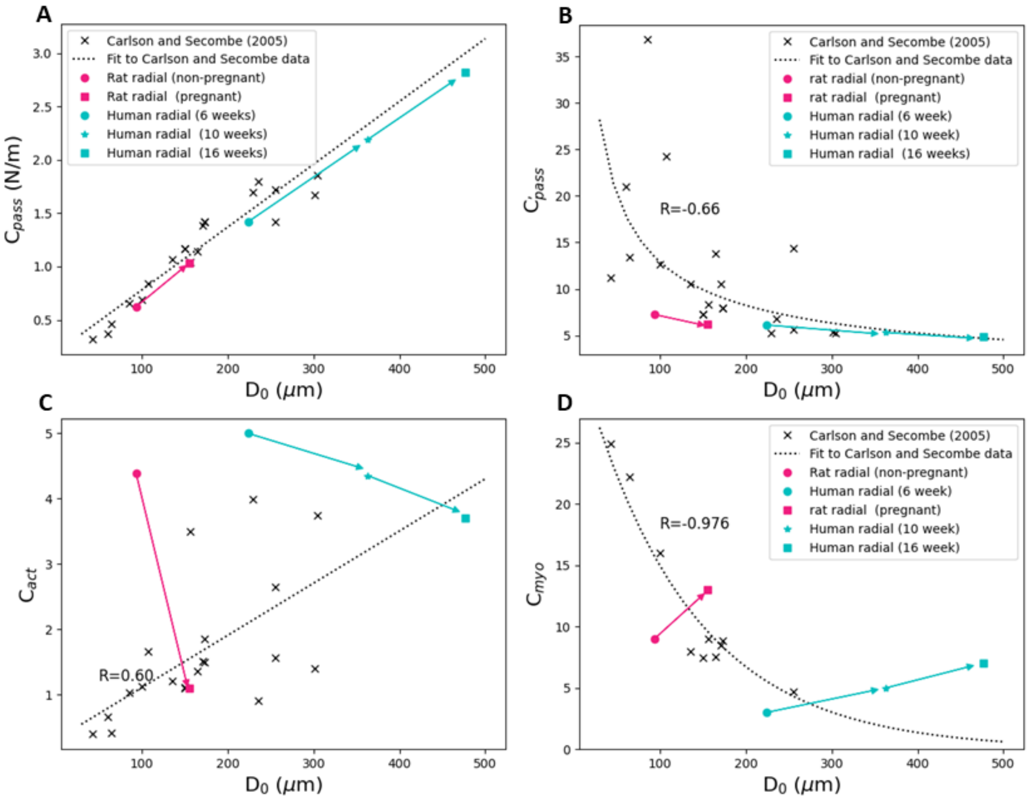

Figure 25: Plots of the four parameters dependent of vessel diameter with the experimental data fits, the rat parameter fits and the predicted human parameter fits. The three projected values for human model of radial artery behaviour for the three models of gestation 6-8 week, 10-12 week, and 16-18 week.

Table 7: Table of vascular reactivity parameters matched for human at 6-8, 10-12, and 16-18 week gestational models. Parameters which are not dependent on diameter sourced from Allerkamp et al. (Allerkamp et al. 2022).

Parameter	**Description**	**unit**	**Human**		
			6 weeks	**10 weeks**	**16 weeks**
D_0	passive diameter of the vessel at a pressure of 100mmHg	µm	224	363	477
C_{pass}	passive tension at 100mmHg	N.m	1.42	2.19	2.82
$C_{passdash}$	steepness of the exponential curve describing passive tension	no unit	6.12	5.31	4.82
C_{act}	maximum active tension	N.m	5	2.89	3.71
C'_{act}	controls diameter of peak active tension	no units	0.99	0.766	0.766
C''_{act}	controls width of Gaussian curve defining active tension	no units	0.181	0.18	0.18
C_{myo}	controls strength of myogenic response	m/N	0.003	0.007	0.007
C''_{tone}	a constant parameter	no units	-6.69	-7.15	-7.15
C_{shear}	controls smooth muscle tone in constriction response to shear	1/Pa	0.08	0.0772	0.0772
CS_{hear1}	controls smooth muscle tone in relaxation response to shear	1/Pa	0.045	0.3035	0.3035
T_1	muscle tone begins to increase with increasing shear	Pa	1.67E-12	16.401	16.401
T_2	shear stress at which smooth muscle tone begins to decrease (relax) with increasing shear	Pa	40.326	40.326	40.326

4.3.2 Combined Response – relation of pressure and vessel diameter

Whilst passive and active responses were previously modelled in rat radial arteries, this thesis sought to translate these models to human radial arteries. To model the passive and active responses in the human models, the relationship between pressure and diameter was predicted at each of the three gestational stages. The passive model results (Figure 26A) show a curve for each gestational stage with an increasing diameter with pressure. Figure 26B, the active and passive models for 6 week gestation had a similar shape to the non-pregnant rat model curves. Figure 26D, passive and active model response for 16 weeks gestation, has a second constricting phase to the active response at higher pressures, again in line with the pregnant rat model. Figure 26C, the active and passive responses at 10 weeks gestation, has the same constricting response. The physiological blood pressure in humans is approximately 80mmHg.

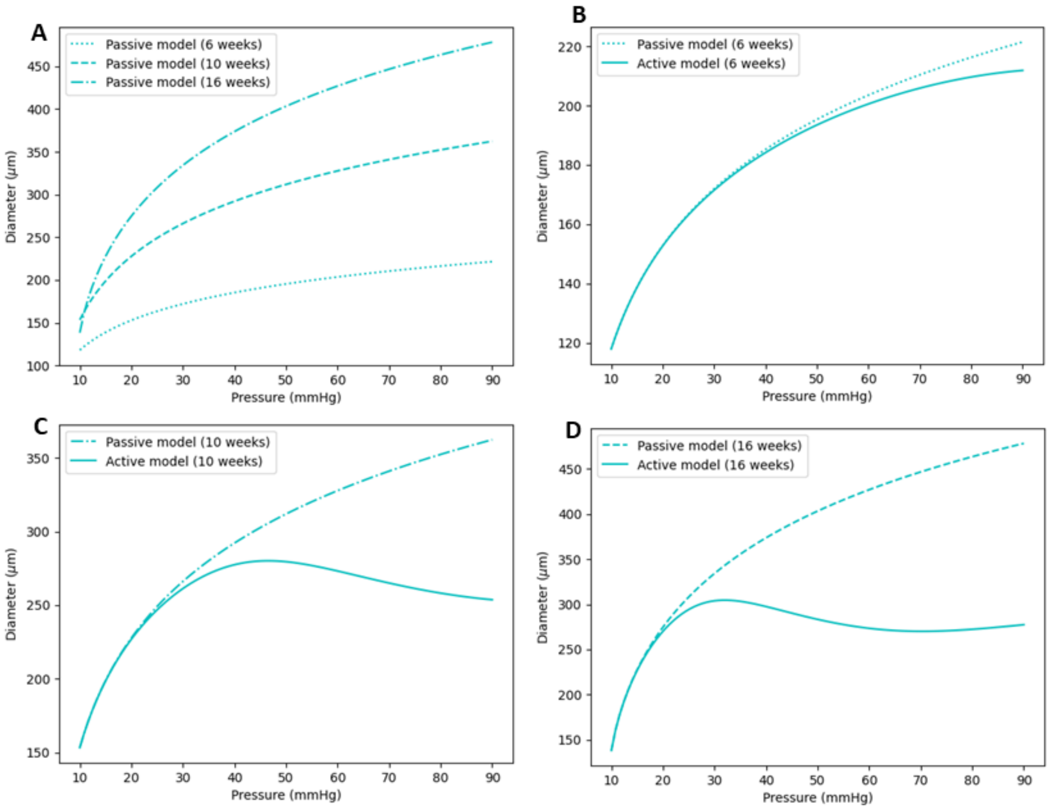

Figure 26: Plots of the relationship between pressure and diameter for the human passive model response and the addition of the active model response for three gestational stages. A) Passive model response curves show larger diameter at same pressure for larger diameters consistent with later stages of pregnancy. B) Active response curves plotted alongside the passive model, for the 6-8 week model, show that the active model initially follows the passive but smooth muscle activity acts to constrict at higher pressures. C) Active and passive response for 10-12 week gestation stage shows the more dominant active response. D) Active and passive response for model at 16-18 weeks gestation, shows the active response acts to constrict the vessel.

4.3.3 Vascular Reactivity in the presence of flow

Adding flow to the system induces the shear component in vascular reactivity. Figure 27 shows the predicted pressure diameter when flow is introduced to the system. As pressure increases, the dilatory response is mediated by a flow constriction response. For the non-pregnant human model (Figure 27A), the constricting response is observed around 40mmHg intraluminal pressure while the pregnant arteries (Figure 27B) begin to constrict at a lower pressure, around 20mmHg intraluminal pressure. The pregnant radial arteries modelled are able to withstand higher flow rates before constricting, similarly to the rat arteries.

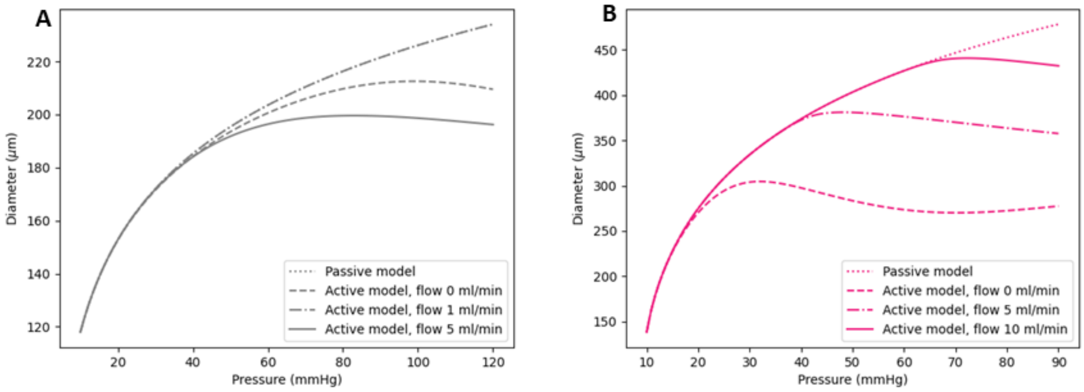

Figure 27: Plots of the relationship between pressure and vessel inner diameter for the passive model, active function added and the addition of flow to the system. A) Pressure diameter curves for the human model at 6-8 weeks gestation. B) Pressure diameter curves for the human model at 16-18 weeks gestation.

4.3.4 Sensitivity Analysis

In order to reflect uncertainty in human parameterisation of the model for vascular reactivity, for the parameters which are dependent on vessel diameter (C_{pass}, C'_{pass}, C_{act} and C_{myo}), a sensitivity analysis was conducted to see the impact each individual parameter has on the pressure diameter curves predicted by the model. Figure 28 shows the pressure diameter curves for the human parameters fits for the 6-8 week model and 16-18 week model. Keeping the other parameters constant, the pressure diameter relationship was plotted for range of values for D_0 from 0 to 500 um (Figure 28A &B). For D_0 and C_{pass}, the relationship defined in equation 19 was maintained. With increasing parameter values the D_0 curves are shifted upwards, showing trend of larger diameter for same pressure. The curves for C_{pass} show a similar trend of an upward shift with increasing value (Figure 28C &D). The curves for C'_{pass} show a larger separation at lower pressures and converge at higher pressure values. C'_{pass} is defined in equation 19 and governs the steepness of the curve (Carlson and Secomb 2005). The model was able to find valid solutions for the range of values tested.

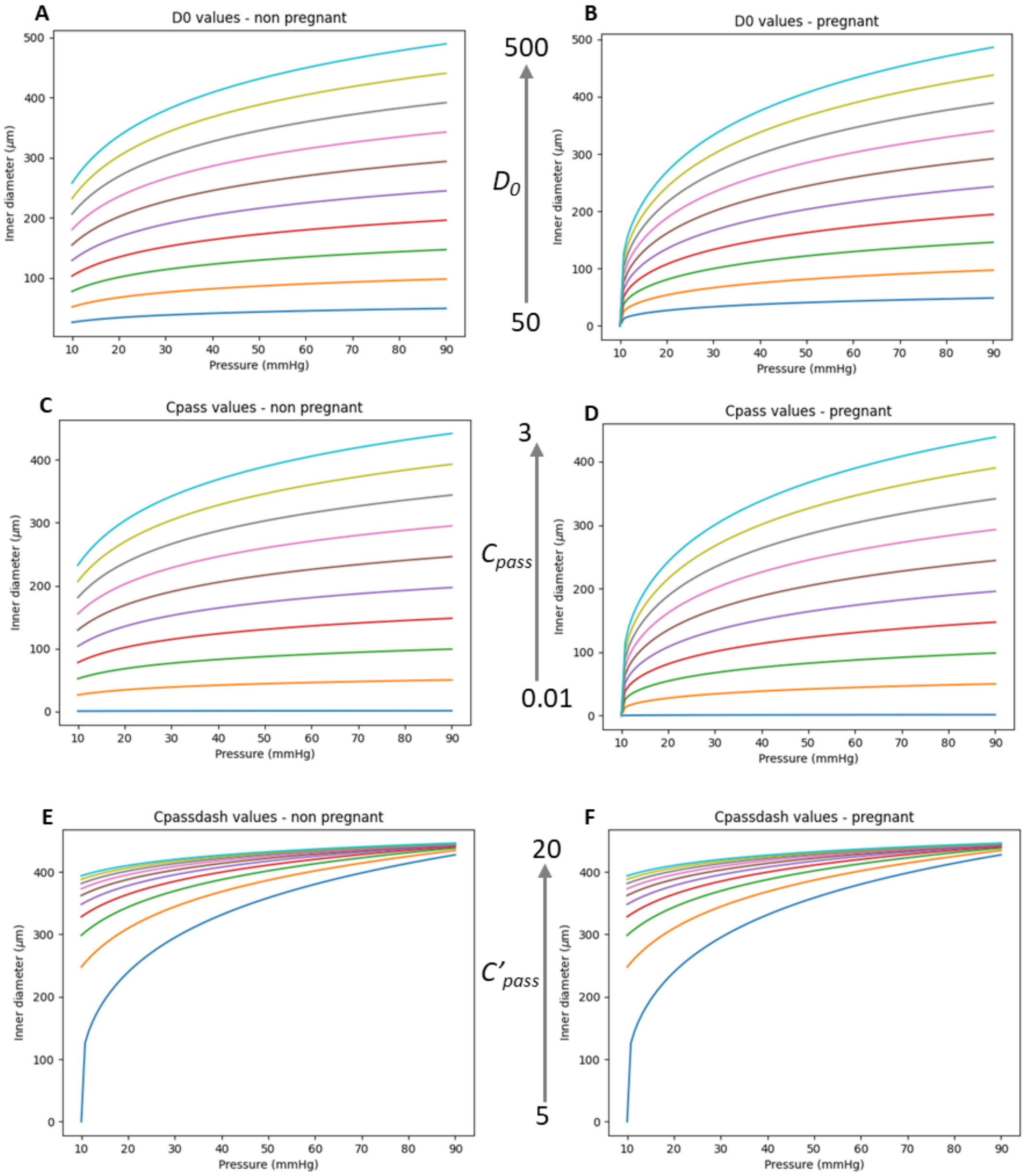

Figure 28: Plots from a sensitivity analysis for the human parameters for vascular autoregulation which are dependent on vessel diameter for the passive model. A) For the non-pregnant human parameter fits, vary D_0 over range 50 to 500. B) For the pregnant human parameter fits, vary D_0 over range 50 to 500. C) For the non-pregnant human parameter fits, vary C_{pass} over range 0.01 to 3. D) For the pregnant human parameter fits, vary C_{pass} over range 0.01 to 3. E) For the non-pregnant human parameter fits, vary C'_{pass} over range 5 to 20. For the pregnant human parameter fits, vary C'_{pass} over range from 5 to 20.

Figure 29 contains the pressure diameter curves for the human parameters dependent on vessel diameter in the active model. Figure 29A and B show the sensitivity analysis results for parameter C_{act} 6-8week and 16-18week models respectively. For the 6-8week curves, the shape is similar to that of the rat non-pregnant graphs while the pregnant graph follows the shape of the expected for pregnant rat radial arteries. Other parameters which were not included in the sensitivity analysis as they are not dependent on vessel diameter, an assumption was made that the 6-8week model has the same values as the non-pregnant rat model and the 16-18 week with the same values as the pregnant rat model.

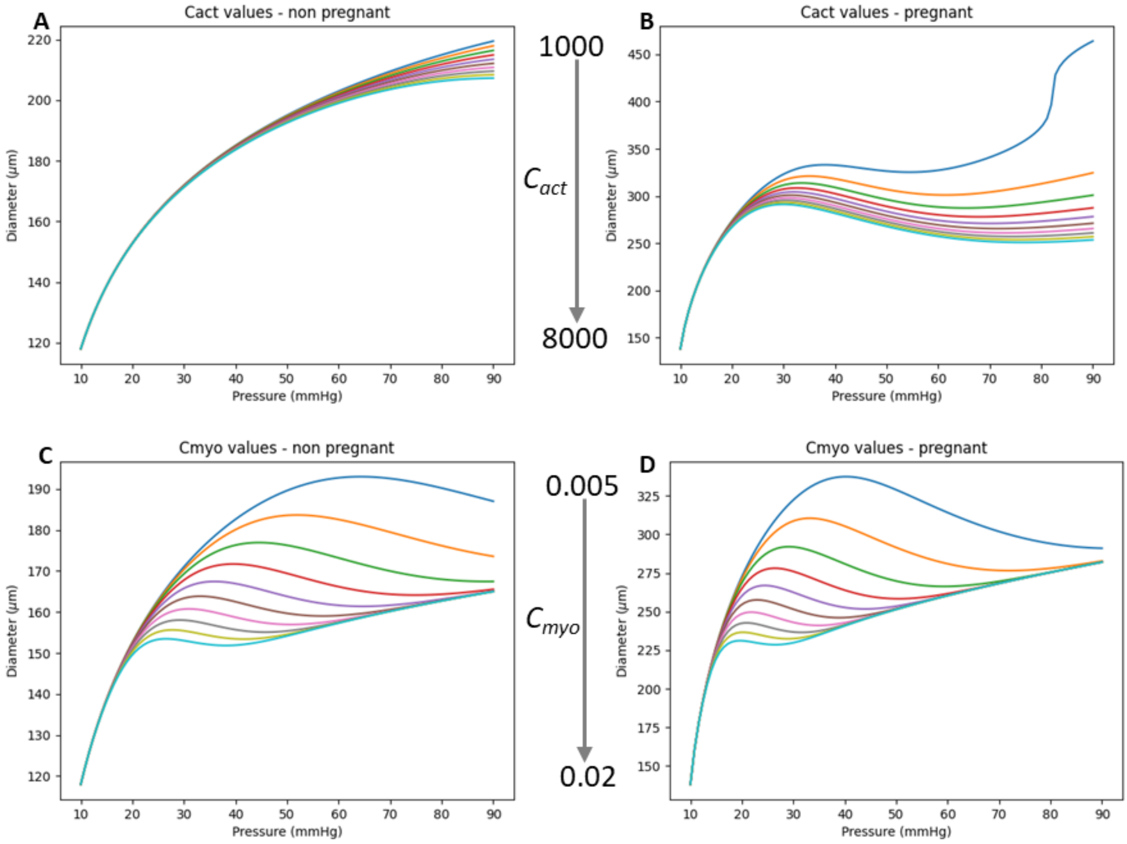

Figure 29: Sensitivity analysis plots for the human parameter fits for vascular autoregulation, active model with no flow. A) Range of C_{act} human parameter for non-pregnant model. B) Range of C_{act} human parameter values for pregnant model. C) Range of C_{myo} human parameter values for non-pregnant model. D) Range of C_{myo} human parameter values for the pregnant model.

4.3.5 Network models of circulation with simple vessel compliance

This thesis next sought to incorporate models of vascular reactivity for an isolated vessel into network models of uterine circulation. First, a simple model of compliance, based on a linear relationship between pressure and diameter by a compliance parameter α, was implemented into the network models of uterine circulation as outlined in Chapter 3. The vessel diameter was predicted over a stepwise increase to inlet flow rate for a constant inlet pressure. Physiologically, over the course of pregnancy, flow rate is expected to increase.

Rat vessel networks, linear compliance

Figure 30 shows the change in diameter for both the non-pregnant and pregnant rat models. From the passive experimental data, a gradient of $3.16e^{-6}$ mm/Pa for the virgin rat model and $6.48e^{-6}$ mm/Pa for the pregnant rat model, were extracted for the value of compliance factor α. The predicted radial artery radius values for these input flow rates are plotted (black dotted line) along with the “measured flow” (the red plus in Figure 30), which is the expected physiological value for these models (Figure 30). The compliant model predicts a radius 2.5% higher than the vessel radius measured ex vivo at the physiological inlet flow rate for the non-pregnant model, and 2.3% higher in the pregnant model. This small difference in predicted radius relative to measured physiological value could be explained by the absence of flow mediated effects. The compliant vessel model predicts, a larger vessel radius than measured ex vivo without pressure control, as blood pressure acts to expand the vessel. In both non-pregnant and pregnant models, this diameter decreases in size with increasing input flow rate. This is because the boundary conditions imposed on the model fix input pressure and flow, so when flow increases pressure in the radial arteries decreases.

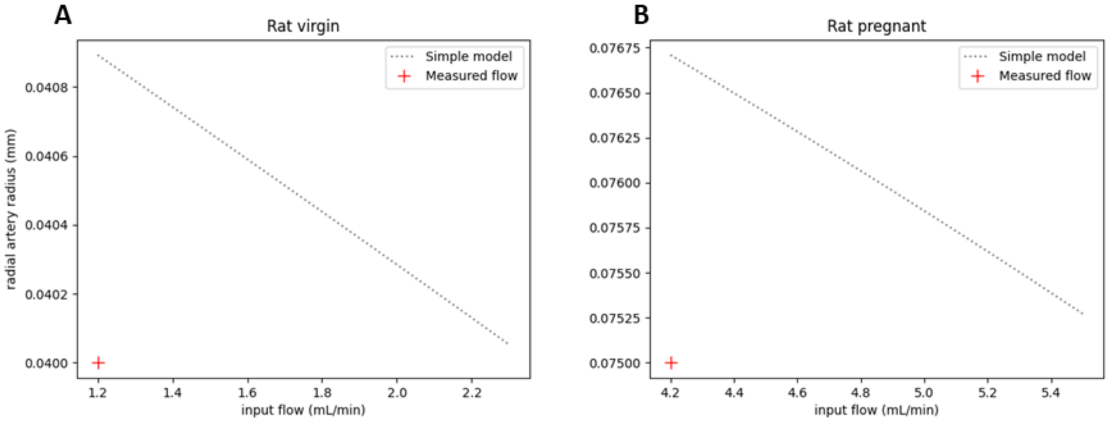

Figure 30: Plots of inlet flow rate against radial artery radius for simple compliance models at the radial artery level for rat uterine circulation. A) The virgin rat model flow radius relationship and a point for the measured inlet flow and radial radius. B) the pregnant rat model flow radius relationship and a point plotted for the measured inlet flow and radial radius.

Human vessel networks, linear compliance

Figure 31 plots the same relationship for the three human models of uterine circulation. A linear decrease in vessel lumen is seen for increasing flow rate, as with the rat. The non-pregnant rat model alpha was used for the human 6-8 weeks model and the pregnant rat model alpha value was applied in the human 10-12 week model and the 16-18 week model. The trends in the human models are similar to the rat model. At the expected physiological inlet flow rate, the vessel size measured ex vivo (measured from histology without pressurised vessels) was 3.2% higher compared to the model prediction for the 6-8 week model, 3.3% in the 10-12 week model and 7% higher for the 16-18 week models. For all the models (regardless of gestation), radius decreases with increasing flow rate.

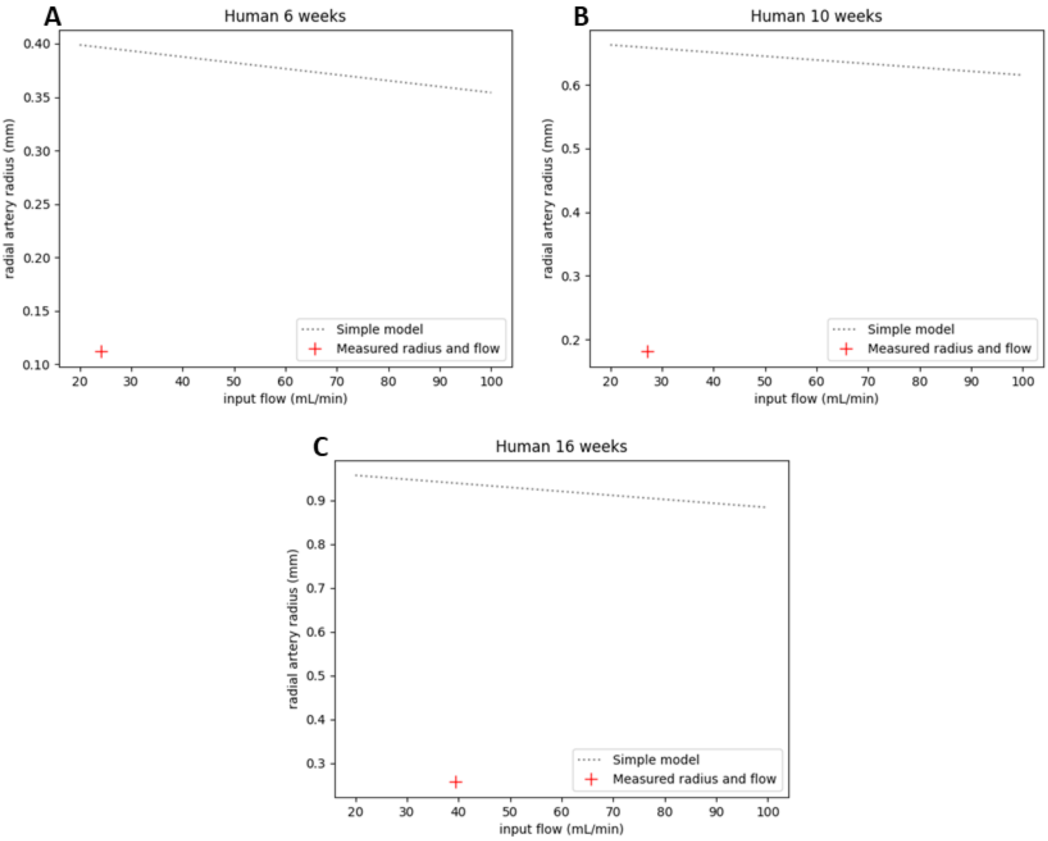

Figure 31: Plots of inlet flow rate against radial artery radius for simple compliance models at the radial artery level for human uterine circulation. A) The 6-8 week human model of gestation flow radius relationship and a point for the physiological (measured) inlet flow and radial radius. B) The 10-12 week human model of gestation. C) The 16-18 week human model of gestation.

4.3.6 Network models of circulation with vessel autoregulation

After incorporating the simple linear models of vessel compliance into the network models of utero-placental circulation, the more complex models of vascular reactivity were also incorporated at the radial artery levels. These models of vascular reactivity distinguish between the passive response, active (no flow) and shear response and while they have been previously modelled for rat radial arteries (Allerkamp et al. 2022), these models have not yet been incorporated into organ level network models of circulation. The results presented are for the two rat models, virgin and pregnant, and the three human models of gestation, 6 -8 weeks, 10-12 weeks, and 16-18 weeks.

Rat model, including reactivity

Keeping the inlet pressure constant, inlet flow was increased from a physiological starting value in a stepwise fashion (Figure 32). For the virgin rat model, at the physiological inlet flow the passive compliance model predicts a vessel radius 4.8% larger than the physiological vessel radius. As inlet flow increases, the radius of the radial arteries reduces as the vessel constricts in response to the increased flow. For the pregnant rat model, at the physiological inlet flow the passive model predicts a radial artery radius 26.4% smaller than the physiological radius. As input flow increase, these vessels continue to constrict, further reducing the vessel radius. Comparing the passive vessel mechanics to the response when active function is added, the active function had a marginal effect of further constricting the vessel. The addition of the flow mediated response has no change on the flow radius curve. While the simple model of compliance showed a linear relationship (Figure 30), this more complex model of compliance shows a non-linear relationship (Figure 32).

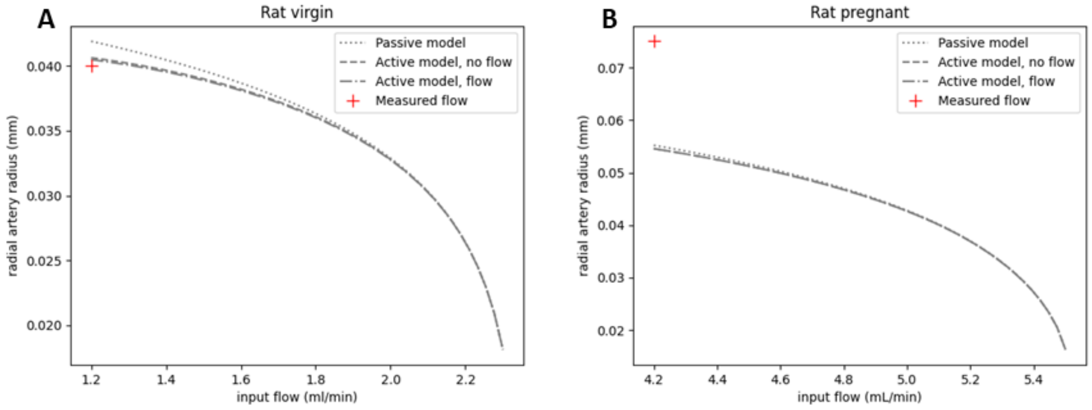

Figure 32: Plots of network input flow against radial artery radius of rat uterine circulation with vascular reactivity at the radial artery level. A) Non-pregnant (virgin) rat model. B) Pregnant rat model.

Human model, including reactivity

The human uterine arterial network has the additional feature of AV anastomoses which can bypass blood flow from the IVS to connect directly into the veins at a point in the network between the radial arteries and the spiral arteries. For the human model, inlet flow was initially kept constant and the flow in the spiral arteries in a static network (Chapter 3) was compared to the network model with vascular reactivity at the radial artery levels. Flow through the spiral arteries feeds directly through to the placenta, while flow through the radial arteries can branch into the spiral arteries or to the AV-anastomoses which bypass the intervillous and connect straight into the venous network. By looking at flow through the spiral arteries, it is possible to see how the vascular reactivity changes the flow that reaches the placenta. For the 6-8 week gestational model, compliant radial arteries reduced flow through the spiral arteries by 0.33%. Flow through the spiral arteries in the 10-12 week gestational model reduced by 3% while the 16 to 18 week gestational model reduced by 12%.

Next, inlet pressure was kept constant, and inlet flow was increased from the physiological values in a stepwise fashion up to an approximate physiological flow rate at term, 500mL/min. For the network model prediction, the passive responses, active (no flow) responses and shear (flow) mediated responses of the compliant radial arteries were then compared. At the physiological flow rate, the passive model predicts a radius 4.5% less than the physiological radius for the 6-8 week model, 2.8% lower in the 10-12 week model and 9.7% lower in the 16-18 week model (Figure 33). The physiological values which are measured ex vivo and as such are in a relaxed state (Allerkamp et al. 2021). When the active response is added to the system, the predicted radius reduces 7% relative to the physiological radius for 6-8week model, 29% for 10-12 week model and 47% for 16-18 week model. The addition of the flow mediated response has no effect on the radius for any of the models, suggesting that the vascular response is in the region of shear response where it has no effect on constriction or dilation of the vessel. For the 6-8 weeks gestational model, with increasing flow rate, radial artery radius continues to decrease over the range tested. For the 10-12 week model, at flows above physiological, the active response dampens the passive response but there is a period where diameter increases with flow before beginning to decrease again. Lastly, for the 16-18 week model follows a similar trend to the 10-12 week model.

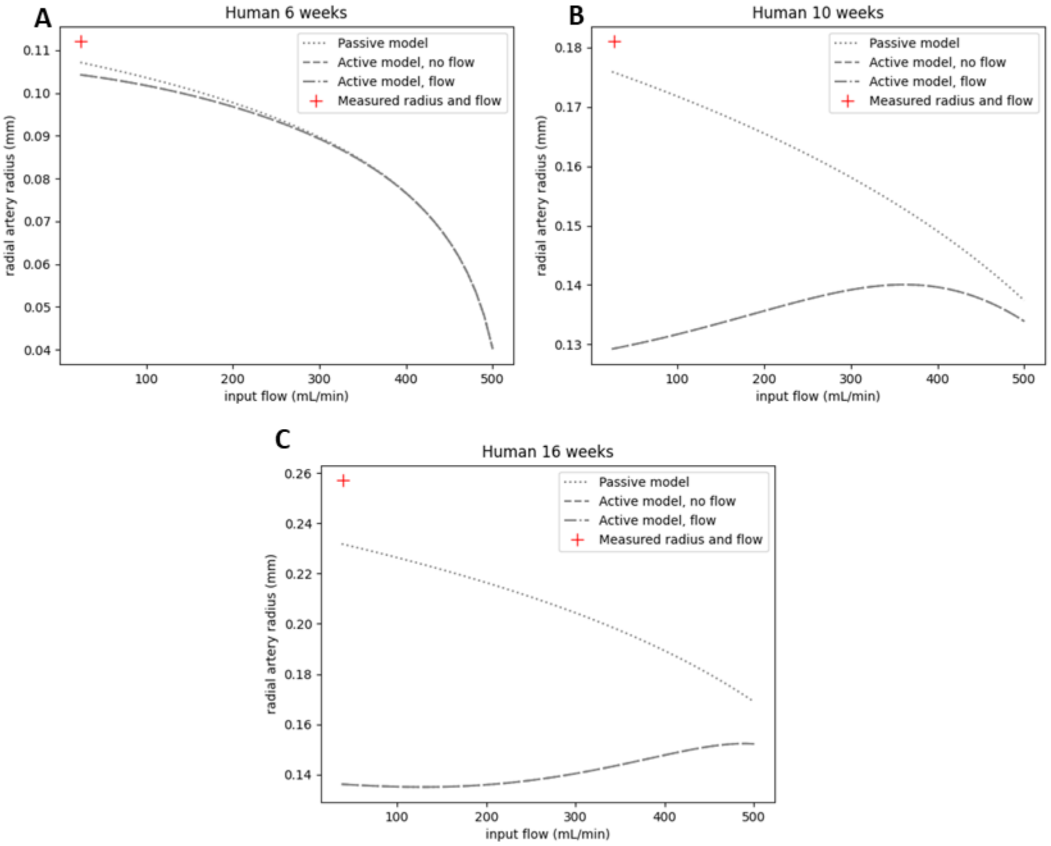

Figure 33: Plots of network input flow vs radial artery radius for human models of uterine circulation with vascular reactivity at the radial artery level. The three lines represent passive model, active model no flow and the flow mediated response. A point was also included for inlet flow and measured radial artery radius from the static models of circulation. A) Model for 6-8 weeks gestation B) Model for 10-12 weeks gestation C) Model for 16-18 weeks gestation.

4.4 Discussion

In this chapter a model of vascular autoregulation (Carlson, Arciero, and Secomb 2008; Allerkamp et al. 2022) was translated from a model for rat radial arteries into a model for human radial arteries as it is not possible to conduct the ex vivo experiments with human uterine vessels. Human arteries were expected to be more compliant due to their larger size, and the Carlson and Secomb data fits helped to extrapolate the parameters dependent on vessel size (C_{pass}, C'_{pass}, C_{act} and C_{myo}). Vascular autoreactivity is also altered by the paracrine environment created during pregnancy. The trend from non-pregnant to pregnant behaviour captured in the rat models is expected to translate between the species to the human model (Allerkamp et al. 2022). While two rat models, pregnant and non-pregnant, were parametrised by Allerkamp et al. (Allerkamp et al. 2022) the human models here are defined in gestational stages across the first half of pregnancy. An assumption was made that the 6-8 week model is closer to that of the non-pregnant rat while the 16-18 week model was closer to that of the pregnant rat, and that changes over gestation in vascular reactivity are linear. Physiologically, at 6-8 week gestation, the paracrine environment has already been changed and so it is likely that vascular reactivity has already been affected. At 16-18 weeks, although this gestational stage is far from term, it is reasonable to assume that most changes have occurred, as vessels have been exposed to the paracrine environment of pregnancy for several weeks.

As human model parameterisation cannot be tested, a sensitivity analysis was conducted by varying the compliance parameters across a range within the different anatomical scenarios across the first half of pregnancy. The model was able to solve for solutions within the physiologically relevant range of values. The results helped to demonstrate how each of the parameters which depend on vessel size change the shape of the pressure diameter curves for a range of values. Only one set of parameters for each of the human models was carried forward into the network modelling. Further work could include assessing how a parameter values effects the network response, rather than just the single vessel response presented in section 4.2.4. For the other parameters which are not dependent on diameter, but do change value with pregnancy, these parameters are likely to change on a spectrum for the human models rather than non-pregnant and pregnant value sets available. In the vascular reactivity models, τ_1 and τ_2 define the points that the shear stress component of the total active response changes from zero, to constricting and then to dilating (equation 24). It is possible that the τ_1 and τ_2 values for the human models need refining, or it could be that the range of pressure and flow values in the network model are in the range of shear stress values where there is no contribution from the shear response to the total active response. Further work could be done to better define a range of parameter values across the time span of gestation to model the progressive changes of pregnancy to vascular autoregulation.

These models for vascular reactivity at a single vessel scale were incorporated into the network models of uterine circulation, as presented in Chapter 3. Radial arteries have been previously identified as key modulators of maternal blood in the network of vessels that make up the uterine circulation, which acts to feed the placenta during pregnancy (Allerkamp et al. 2021). A simple model relating radius to pressure by a linear function and compliance factor α, was also presented as a comparison with this more complex model of compliance. The value of α was derived for the rat model as experimental data is available. These values were then translated into the human model however, the human models would be more accurate with an α value based on the passive model response as it is not possible to obtain human vessels for ex vivo experiments. A linear relationship in the simple model between pressure and diameter shows vessel lumen decreasing with a stepwise increase to input flow rate. A non-linear relationship is observed in more complex models of vessel compliance. The model of vascular reactivity implemented (Allerkamp et al. 2022; Carlson, Arciero, and Secomb 2008) means it is possible to see how the passive, myogenic and flow mediated responses combine to either be additive or reductive. The passive response follows the trend of increasing vessel diameter with increasing pressure. When the active response is added, the myogenic response (no flow) adds a constriction response, dampening the passive increase in diameter. Adding the shear response onto this gives the overall combined response. For the range of pressure and flow conditions modelled, the addition of flow does not change from the active response in the network model. Radial arteries show shear mediated constriction behaviour, but only after a certain shear value is reached. Pregnancy adapts the radial vessels to tolerate a higher flow rate before constricting, which is important for maintaining blood flow through to the placenta. While the predicted behaviour of radial arteries was incorporated into these network models of uterine circulation, the impact of un-adapted radial arteries in a network model requires further assessment.

The results for the model predictions for a single vessels autoregulation response are presented as pressure diameter curves, while the network model data is presented as inlet flow diameter curves. While comparing rat flow radius curves to human model flow radius curves, it is important to remember the differences in their network circulation. AV anastomoses present in human anatomy provide a shunt pathway direct to venous circulation located after the radial arteries in the network (Clark, Alys et al. 2018). In humans, for high downstream resistance, flow in the network may be diverted to the venous network, bypassing the IVS as flow will always take the path of least resistance. Vascular reactivity can either work to reduce resistance (dilating) or increase resistance (constricting). For the human models, comparing the flow through the spiral arteries between the static network model and the network model with compliant radial arteries is useful as they feed blood directly through to the placenta. Rat models' arcuate arteries can loop back to the uterine artery, but these are upstream of the radial arteries. While both the human and rat spiral arteries are invaded by trophoblast cells and remodelled into stiff wide bore funnels, human spiral arteries also have pseudo-plugs to flow as modelled in Chapter 3. If this part of the remodelling process was disrupted, then it is possible spiral arteries may retain some vasoreactivity behaviour, altering the pressure and flow conditions.

There are limitations to the predictions of models in this chapter, including significant uncertainty in the evolution of vascular function in humans in pregnancy, as it is simply not possible to measure these changes in the early stages of pregnancy. In addition, a fixed inlet pressure is assumed in all models in this thesis (discussed further in Chapter 5), which may impact the accuracy of model predictions in a network context. However, this model does provide an important proof of concept that vascular network function is likely highly dependent on the reactivity of the vessels within it. This is illustrated strongly by the fact that when no vessel compliance or a simple vessel compliance is assumed, the model behaves differently to when a non-linear model of vascular reactivity is incorporated. This indicates that further research into the evolution of the network of vessels in the uterus over pregnancy is required to relate expected changes to outcomes.

Chapter 5 – Conclusions and Future Work

Although adequate adaption of the uterine circulation is critical for a healthy pregnancy, it is very difficult to assess, and little is quantified in regard to anatomical structure and function over the course of gestation. The computational modelling presented for uterine circulation in this thesis used novel anatomical measurements that define the evolution of the human uterine artery anatomy in the first half of pregnancy. This allowed for the refinement of existing models, and new modelling of the mathematical descriptions for trophoblast plugging and the subsequent breakdown with gestation. By considering the arteries upstream of the trophoblast plugs (in the spiral arteries), it was possible to infer how downstream features influence upstream haemodynamics, linking features of remodelling at multiple points of the system. A network model of the rat uterine circulation was also constructed, from micro-CT data in non-pregnant and near-term rats, as human data on the function of isolated uterine blood vessels is rare. With anatomically derived network models of human and rat uterine circulations, this thesis then considered vascular reactivity within a network context of uterine circulation. Models of vascular reactivity previously parameterised for rat radial arteries (from experimental data) were extrapolated to human models. A sensitivity analysis was carried out assessing how human parameter values influence the pressure and diameter curves for isolated vessel models. These models of vascular reactivity were then incorporated into network models to consider how vascular autoregulation might influence network function, with an interplay between vessel diameter, blood pressure and flow/shear stress. The modelling was able to demonstrate that 1) vascular reactivity alters network behaviour and 2) the feedback in a network changes the behaviour from what is seen for a vessel in isolation.

Chapter 3 presented new network models of the uterine circulation, with the primary addition to these models being a mathematical description of the nature of trophoblast plugs in human uterine circulation. Using anatomical quantification from Allerkamp et al. (Allerkamp et al. 2021), the models aimed to represent spiral arteries that are initially plugged with trophoblast but as pregnancy progresses, channels begin to form in the plugged regions. Plugged arteries and arteries with channels through the plugs, were described mathematically assuming that the plugged portions of the arteries can be represented as porous media. The computational modelling of trophoblast plug breakdown supports the idea that channels become the dominant pathway for flow as they form within plugs, particularly as the trophoblast aggregates that line the vessels around channels appear to be tightly packed (low porosity). This suggests that channels act as a bottleneck for flow and may prevent a sudden increase in flow to the placental surface that might have arisen if plugs simply dispersed. Previous modelling approaches (Saghian et al. 2019), have suggested that the formation of channels may contribute to plug break up. Saghian used agent-based modelling to investigate plug evolution computationally, and suggested that once these channels begin to form, they become highways for flow. Trophoblast cells cannot migrate effectively in high flow (shear stress) regions and so channels likely grow over gestation (James, Whitley, and Cartwright 2011). While the model presented here does not evolve dynamically like an agent-based model of a plugged spiral artery (Saghian et al. 2019), it does enable analysis of the consequences of adequate and inadequate spiral artery remodelling on the upstream vessels in the uterine circulation, as it represents the whole organ. A study by Gleason et al developed a mathematical model for the whole maternal vascular tree incorporating changes to maternal vasculature and cardiac output over the course of an uncomplicated pregnancy (Gleason and Sedaghati 2022). The modelling captured vessel geometries, mechanical properties, and hemodynamic metrics, and validated the results against UtA velocity waveforms measured in clinical ultrasounds (Gleason and Sedaghati 2022). The study further highlighted gaps in the data available from literature to validate computational models (Gleason and Sedaghati 2022).

Plugging in the spiral arteries reduces shear stress (and flow) in the upstream radial and arcuate arteries, while shear stress predictions in the uterine arteries were not changed by the absence/presence of plugging Trophoblast plugs had the greatest impact on upstream shear stress in the 10-12 week model of gestation where channels through the porous plug are observed and modelled. The plug aggregate is sufficient to still limit flow at this stage in gestation (as noted by an increase when they are not modelled in the system) but in their absence, the system is able accommodate an increase in flow. In the 6-8 week model, while trophoblast plugs limit flow through to the IVS, vessel lumens appear to be sufficiently small to still resist a large flow increase through the network. By the time gestation has progressed to 16-18 weeks, the channel has sufficiently widened, and the remaining trophoblast aggregates have negligible impact on upstream shear stress values.

Chapter 4 incorporated vascular reactivity into the presented network models of uterine circulation at the radial artery level. A model of vascular reactivity parameterised for rat radial arteries based on experiment work by Allerkamp et al. (Allerkamp et al. 2022) was extrapolated for human radial arteries to account for the relative increase in vessel lumen and how the paracrine environments of non-pregnant and pregnant may relate to gestation. These parameterised models of vessel autoregulation were then incorporated into the network models (outlined in Chapter 3) which altered their behaviour relative to how they behave in isolation. Additionally, the inclusion of vascular reactivity altered network behaviour relative to the static model. Comparing the static network models to those with compliance showed a reduction in blood flow reaching the placenta which increased with gestation. The passive vessel response was comparable with the physiological radius at physiological inlet flow, while the addition of the active response (no flow) further reduces the vessel lumen, and the addition of the shear response (flow) had no affect for the flow and pressure conditions modelled. The physiological measurements are captured ex vivo when the vessel is in a relaxed state (Allerkamp et al. 2021) which is more in line with the passive model. With increasing flow rate (as flow is expected to increase with gestation) vessel lumen decreased for the network model conditions.

Throughout this thesis, the same boundary condition was applied across all network models. That is, a volumetric rate of blood flow was prescribed in the uterine artery, the inlet to the system, which was defined based on typical uterine artery blood flow in the rat and human at the gestations considered. In addition, a blood pressure in the uterine artery of 80-84 mmHg was assumed. This prescription of boundary conditions at the system inlet effectively assumes that the uterine resistance does not impact maternal delivery of blood to the organ (either via blood pressure or flow). Multiple alternative boundary conditions could be prescribed, each with their own physiological interpretation. For example, an alternative would be to keep pressure fixed at the venous circulation, an outlet boundary condition for the system. This assumes a venous pressure which is independent of what is happening upstream in the circulation. Another option would be to define a pressure drop across the network such that the uterus does not impact on blood pressure in the maternal circulation. However, a poorly adapted uterus would likely receive less blood as an increased resistance would reduce blood flow for a fixed driving pressure. The models described in Chapter 3 do not include vessel compliance. They describe the resistance of the system (i.e. the relationship between pressure drop and flow) and so, they can be scaled to reflect any of these boundary conditions. However, once the reactivity of uterine blood vessels is considered, accurate boundary conditions are required to define the diameter of individual arteries. In this model, if it were assumed that blood pressure at the veins was fixed, increases in blood flow would elevate pressure at the radial artery level, altering the results presented in this thesis. This would likely lead to a dilation of radial arteries in the models in Chapter 4 at high blood pressures which is not seen in the presented results.

The limitations in the choice of boundary conditions presented are inherent to computational models of the circulation in whole organs. This is because, in a real physiological system, the body (or in this case the maternal circulation) would adapt locally (and perhaps systemically) to a change in uterine circulatory resistance. An improvement would of course be to consider the entire maternal circulation in a model, which could then potentially predict any adaption of the vasculature upstream of the uterus to changes in the uterine circulation. However, with each portion of the maternal circulation added to a model, this increases the complexity of the modelled systems. Therefore, although it would be interesting to include changes in maternal haemodynamics in response to changes in the uterus, this is beyond the scope of work presented here.

Anatomical and vessel reactivity data used in this thesis reflect recent studies that specifically aim to investigate this system (Allerkamp et al. 2021; Allerkamp et al. 2022). However, there are still gaps in our understanding of the system as a whole. For example, data available on the anatomy of the uterine circulation is limited to a very small number of samples, which have been imaged *ex vivo*. Therefore, there is uncertainty and variability in the size of blood vessels in the system. In addition, vascular reactivity has been measured in rats, but parameterisation of the vessel reactivity model in humans has been inferred, in the absence of any specific data. To account for uncertainty in parameters, a sensitivity analysis was conducted on the vessel radii and trophoblast plug parameters in Chapter 3, and vascular reactivity parameters in Chapter 4. A more sophisticated sensitivity analysis methods such as Sobol analysis or polynomial chaos (Zhang et al. 2015; Pettersson 2015) could be implemented to help quantify which parameters have the greatest impact on the solution.

The data available on vessel reactivity was based on the behaviour of vessels in non-pregnant and late pregnant rats. Although assumptions can be made to relate these to the evolution of vessel function in pregnancy and in humans, there is no direct data on how the uterine vessels evolve over time. In addition, although it assumed that the hormones of pregnancy have an influence on vessel behaviours, and there is certainly evidence of the role of hormones in vascular adaption (Osol et al. 2008; Rupnow et al. 2001), the effects of hormones and paracrine factors are not separated out. A more considered approach to the impact of hormones and paracrine factors and how they may progressively change the vessels could be taken in the future. Looking at not just the parameters that change with diameter, but also how all the parameters that change from non-pregnant to pregnant might change across a spectrum, not just the binary. Future work could focus on linking inadequately remodelled radial arteries, from a vascular reactivity perspective to network function by simulating physiological scenarios of how pregnancy may not adequately adapt these vessels and quantifying how that impacts blood flow through to the placenta. By parameterising the human model with un-adapted, or partially adapted radial artery autoregulation into network models, different physiological scenarios could be better assessed.

While it is not possible to conduct ex vivo pressure myography experiments with human uterine vessels, it would be beneficial to test the predictions of human modelling in ongoing pregnancies. This is difficult as the small blood vessels that are important to system function are difficult to detect in vivo. Advances in ultrasound may present future possibilities to better study how the utero-placental circulation adapts with pregnancy. Ultrasound is the current technology that is used most in clinic to assess pregnancies, but it is limited to Doppler waveform profiles (indication of downstream resistance) and the flow patterns from the spiral artery mouths. Improvements to the imaging resolution or ultrasound interpretation may help to improve the ability to resolve smaller but functionally important vessels in the future. If it were able to offer in vivo measurements on some of these smaller uterine vessels, then computational models could be more accurately quantified. To understand how blood vessel respond to maternal flow, it may be possible to look at scenarios where a change in blood flow in the mother impacts the flow to the uterus. For example, magnetic resonance imaging studies are exploring how a supine position in mothers can reduce blood flow to the uterus and thus, the placenta (Couper et al. 2021). Couper et al found an approximate 20% reduction in blood flow to the uterus in supine compared to the left lying position (Couper et al. 2021). With expected continual improvements in imaging, if uterine, arcuate, or radial arteries could be imaged to provide some indication of their size in relation to this change in position, then this could be used to assess the validity of the type of model presented here. Linking computational modelling with what is observable in clinical measurements is important for relating findings from model simulations with physiology, which may help in identifying the size of change that would need to be measurable to detect pathology and should be a focus for the future.

When considering what aspects of the utero-placental circulation are the most important, it is essential to remember that nothing happens in isolation. It is the interplay between these different structural and functional aspects of circulation that will inform how adequate blood flow is able to carry oxygen and nutrients to the growing fetus. This thesis has made steps toward constructing models of some aspects of this interplay by incorporating data on anatomy, and function in isolated vessels, into an integrated model of utero-placental circulation

Bibliography

1. Allerkamp, Hanna H., Teagan Pole, Ali Boukham, Joanna L. James, and Alys R. Clark. 2022. "Pregnancy-Specific Uterine Vascular Reactivity: A Data-Driven Computational Model of Shear-Dependent, Myogenic, and Mechanical Radial Artery Features." *American Journal of Physiology.Heart and Circulatory Physiology; Am J Physiol Heart Circ Physiol* 323 (1): H72-H88. doi:10.1152/ajpheart.00693.2021.

2. Allerkamp, Hanna H., Alys R. Clark, Tet Chuan Lee, Terry K. Morgan, Graham J. Burton, and Joanna L. James. 2021. *Something Old, Something New: Digital Quantification of Uterine Vascular Remodelling and Trophoblast Plugging in Historical Collections Provides New Insight into Adaptation of the Utero-Placental Circulation*. Vol. 36 Oxford University Press (OUP). doi:10.1093/humrep/deaa303.

3. Assali, N. S., B. Nuwayhid, and M. Zugaib. 1978. "Control of the Uteroplacental Circulation in Health and Disease." *European Journal of Obstetrics and Gynecology; Eur J Obstet Gynecol Reprod Biol* 8 (1): 43-55. doi:10.1016/0028-2243(78)90008-4.

4. Baeyens, N., S. Nicoli, B. G. Coon, T. D. Ross, K. es, J. Han, H. M. Lauridsen, et al. 2015. "Vascular Remodeling is Governed by a VEGFR3-Dependent Fluid Shear Stress Set Point." *eLife; Elife* 4 (4): 4645. doi:10.7554/eLife.04645.

5. Blackburn, Susan Tucker. 2007. *Maternal, Fetal, & Neonatal Physiology : A Clinical Perspective*. 3rd ed.. ed. St. Louis, Mo.: St. Louis, Mo. : Saunders Elsevier c2007.

6. Brinkman, H. C. 1949. "A Calculation of the Viscous Force Exerted by a Flowing Fluid on a Dense Swarm of Particles." *Flow, Turbulence and Combustion* 1 (1). doi:10.1007/BF02120313.

7. Browne, Leonard D., Khalid Bashar, Philip Griffin, Eamon G. Kavanagh, Stewart R. Walsh, and Michael T. Walsh. 2015. "The Role of Shear Stress in Arteriovenous Fistula Maturation and Failure: A Systematic Review." *PloS One; PLoS One* 10 (12): e0145795. doi:10.1371/journal.pone.0145795.

8. Burton, Alan C. (Alan Chadburn). 1972. *Physiology and Biophysics of the Circulation; an Introductory Text*. 2d ed.. ed. Chicago: Chicago, Year Book Medical Publishers 1972.

9. Burton, G. J., A. W. Woods, E. Jauniaux, and J. C. P. Kingdom. 2009. *Rheological and Physiological Consequences of Conversion of the Maternal Spiral Arteries for Uteroplacental Blood Flow during Human Pregnancy*. Vol. 30 Elsevier BV. doi:10.1016/j.placenta.2009.02.009.

10. Carlson, Brian E., Julia C. Arciero, and Timothy W. Secomb. 2008. "Theoretical Model of Blood Flow Autoregulation: Roles of Myogenic, Shear-Dependent, and Metabolic Responses." *American Journal of Physiology - Heart and Circulatory Physiology* 295 (4): 1572-1579. doi:10.1152/ajpheart.00262.2008. http://ajpheart.physiology.org/content/295/4/H1572.

11. Carlson, Brian E. and Timothy W. Secomb. 2005. "A Theoretical Model for the Myogenic Response Based on the Length-Tension Characteristics of Vascular Smooth Muscle." *Microcirculation (New York, N.Y. 1994)* 12 (4): 327-338. doi:10.1080/10739680590934745. http://www.ingentaconnect.com/content/apl/umic/2005/00000012/00000004/art00002?crawler=true.

12. Christensen, Douglas A. 2009. *Introduction to Biomedical Engineering Biomechanics and Bioelectricity. Part II*. San Rafael, Calif. (1537 Fourth Street, San Rafael, CA 94901 USA): San Rafael, Calif. 1537 Fourth Street, San Rafael, CA 94901 USA : Morgan & Claypool Publishers c2009.

13. Clark, A. R., J. L. James, G. N. Stevenson, and S. L. Collins. 2018. "Understanding Abnormal Uterine Artery Doppler Waveforms: A Novel Computational Model to Explore Potential Causes within

the Utero-Placental Vasculature." *Placenta, 66, 74-81* 66: 74. doi:10.1016/j.placenta.2018.05.001. http://handle.unsw.edu.au/1959.4/unsworks_61879.

14. Clark, A. R., M. Lin, M. Tawhai, R. Saghian, and J. L. James. 2015. "Multiscale Modelling of the Feto–placental Vasculature." *Interface Focus* 5 (2): 20140078. doi:10.1098/rsfs.2014.0078. https://www.ncbi.nlm.nih.gov/pubmed/25844150.

15. Clark, A. R., M. H. Tawhai, E. A. Hoffman, and K. S. Burrowes. 2011. "The Interdependent Contributions of Gravitational and Structural Features to Perfusion Distribution in a Multiscale Model of the Pulmonary Circulation." *Journal of Applied Physiology; J Appl Physiol (1985)* 110 (4): 943-955. doi:10.1152/japplphysiol.00775.2010.

16. Clark, Alys R., Tet Chuan Lee, and Joanna L. James. 2021. "Computational Modeling of the Interactions between the Maternal and Fetal Circulations in Human Pregnancy." *Wiley Interdisciplinary Reviews. Systems Biology and Medicine* 13 (1): e1502-n/a. doi:10.1002/wsbm.1502. https://onlinelibrary.wiley.com/doi/abs/10.1002/wsbm.1502.

17. Clark, Alys, Jo James, G. N. Stevenson, and S. L. Collins. 2018. "Understanding Abnormal Uterine Artery Doppler Waveforms: A Novel Computational Model to Explore Potential Causes within the Utero-Placental Vasculature." *Placenta, 66, 74-81* 66. doi:10.1016/j.placenta.2018.05.001. http://handle.unsw.edu.au/1959.4/unsworks_61879.

18. Couper, Sophie, Alys Clark, John M. D. Thompson, Dimitra Flouri, Rosalind Aughwane, Anna L. David, Andrew Melbourne, Ali Mirjalili, and Peter R. Stone. 2021. "The Effects of Maternal Position, in Late Gestation Pregnancy, on Placental Blood Flow and Oxygenation: An MRI Study." *The Journal of Physiology; J Physiol* 599 (6): 1901-1915. doi:10.1113/JP280569.

19. Gleason, Rudolph L. and Farbod Sedaghati. 2022. "A Mathematical Model of Maternal Vascular Growth and Remodeling and Changes in Maternal Hemodynamics in Uncomplicated Pregnancy." *Biomechanics and Modeling in Mechanobiology; Biomech Model Mechanobiol* 21 (2). doi:10.1007/s10237-021-01555-0.

20. Gokina, Natalia I., Olga Y. Kuzina, Robert Fuller, and George Osol. 2009. "Local Uteroplacental Influences are Responsible for the Induction of Uterine Artery Myogenic Tone during Rat Pregnancy." *Reproductive Sciences (Thousand Oaks, Calif.); Reprod Sci* 16 (11): 1072-1081. doi:10.1177/1933719109340927.

21. Gordijn, S. J., I. M. Beune, B. Thilaganathan, A. Papageorghiou, A. A. Baschat, P. N. Baker, R. M. Silver, K. Wynia, and W. Ganzevoort. 2016. "Consensus Definition of Fetal Growth Restriction: A Delphi Procedure." *Ultrasound in Obstetrics & Gynecology* 48 (3): 333-339. doi:https://doi.org/10.1002/uog.15884. https://doi.org/10.1002/uog.15884.

22. Harris, L. K. 2010. "Trophoblast-Vascular Cell Interactions in Early Pregnancy: How to Remodel a Vessel." *Placenta (Eastbourne)* 31: S93-S98. doi:10.1016/j.placenta.2009.12.012.

23. Hunter, Stewart and Stephen C. Robson. 1992. "Adaptation of the Maternal Heart in Pregnancy." *British Heart Journal; Br Heart J* 68 (12): 540-543. doi:10.1136/hrt.68.12.540.

24. Itskovitz, Joseph, Ella Lindenbaum, and Joseph Brandes. 1980. "Arterial Anastomosis in the Pregnant Human Uterus." *Obstetrics and Gynecology (New York.1953); Obstet Gynecol* 55 (1): 67-71.

25. James, Joanna L., Lawrence W. Chamley, and Alys R. Clark. 2017. "Feeding Your Baby in Utero: How the Uteroplacental Circulation Impacts Pregnancy." *Physiology (Bethesda, Md.)* 32 (3): 234-245. doi:10.1152/physiol.00033.2016. https://www.ncbi.nlm.nih.gov/pubmed/28404739.

26. James, Joanna L., Rojan Saghian, Rebecca Perwick, and Alys R. Clark. 2018. "Trophoblast Plugs: Impact on Utero-Placental Haemodynamics and Spiral Artery Remodelling." *Human*

Reproduction (Oxford) 33 (8): 1430-1441. doi:10.1093/humrep/dey225. https://www.ncbi.nlm.nih.gov/pubmed/29955830.

27. James, Joanna L., Guy S. Whitley, and Judith E. Cartwright. 2011. "Shear Stress and Spiral Artery Remodelling: The Effects of Low Shear Stress on Trophoblast-Induced Endothelial Cell Apoptosis." *Cardiovascular Research* 90 (1): 130-139. doi:10.1093/cvr/cvq396. https://www.ncbi.nlm.nih.gov/pubmed/21156824.

28. Kaviany, M. 1995. *Principles of Heat Transfer in Porous Media*. Second edition.. ed. New York, NY: New York, NY : Springer New York 1995.

29. Khaled, A. A. and K. Vafai. 2003. *The Role of Porous Media in Modeling Flow and Heat Transfer in Biological Tissues*. Vol. 46 Elsevier BV. doi:10.1016/s0017-9310(03)00301-6.

30. Khankin, Eliyahu V., Nga Ling Ko, Maurizio Mandalà, S. Ananth Karumanchi, and George Osol. 2021. *Normalization of Wall Shear Stress as a Physiological Mechanism for Regulating Maternal Uterine Artery Expansive Remodeling during Pregnancy*. Vol. 3 Wiley. doi:10.1096/fba.2021-00019.

31. Khong, T. Y., F. De Wolf, W. B. Robertson, and I. Brosens. 1986. "Inadequate Maternal Vascular Response to Placentation in Pregnancies Complicated by Pre-Eclampsia and by Small-for-Gestational Age Infants." *British Journal of Obstetrics and Gynaecology; Br J Obstet Gynaecol* 93 (10): 1049-1059.

32. Krenz, Gary S. and Christopher A. Dawson. 2003. "Flow and Pressure Distributions in Vascular Networks Consisting of Distensible Vessels." *American Journal of Physiology - Heart and Circulatory Physiology; Am J Physiol Heart Circ Physiol* 284 (6): 2192-2203. doi:10.1152/ajpheart.00762.2002.

33. Li, John K. -J. 2004. *Dynamics of the Vascular System*. River Edge, NJ; London: River Edge, NJ; London : World Scientific Publishing Co. 2004.

34. Lin, Mabelle, Benjamin Mauroy, Joanna L. James, Merryn H. Tawhai, and Alys R. Clark. 2016. "A Multiscale Model of Placental Oxygen Exchange: The Effect of Villous Tree Structure on Exchange Efficiency." *Journal of Theoretical Biology; J Theor Biol* 408: 1-12. doi:10.1016/j.jtbi.2016.06.037.

35. Lloyd-Davies, Claire, Sally L. Collins, and Graham J. Burton. 2021. "Understanding the Uterine Artery Doppler Waveform and its Relationship to Spiral Artery Remodelling." *Placenta (Eastbourne)* 105: 78-84. doi:10.1016/j.placenta.2021.01.004. https://dx.doi.org/10.1016/j.placenta.2021.01.004.

36. Malhotra, Atul, Beth J. Allison, Margie Castillo-Melendez, Graham Jenkin, Graeme R. Polglase, and Suzanne L. Miller. 2019. *Neonatal Morbidities of Fetal Growth Restriction: Pathophysiology and Impact*. Vol. 10 Frontiers Media SA. doi:10.3389/fendo.2019.00055.

37. McCowan, Lesley M., Francesc Figueras, and Ngaire H. Anderson. 2018. "Evidence-Based National Guidelines for the Management of Suspected Fetal Growth Restriction: Comparison, Consensus, and Controversy." *American Journal of Obstetrics and Gynecology* 218 (2): S855-S868. doi:10.1016/j.ajog.2017.12.004. https://dx.doi.org/10.1016/j.ajog.2017.12.004.

38. Meekins, J. W., R. Pinjenborg, M. Hanssens, I. R. McFadyen, and A. Van Asshe. 1994. "A Study of Placental Bed Spiral Arteries and Trophoblast Invasion in Normal and Severe Pre-Eclamptic Pregnancies." *British Journal of Obstetrics and Gynaecology; Br J Obstet Gynaecol* 101 (8): 669-674.

39. Milner, Julia and Jane Arezina. 2018. *The Accuracy of Ultrasound Estimation of Fetal Weight in Comparison to Birth Weight: A Systematic Review*. Vol. 26 SAGE Publications. doi:10.1177/1742271x17732807.

40. Mo, Larry Y. L., Peter A. J. Bascom, Knox Ritchie, and Lesley M. E. Mccowan. 1988. *OOriginal Contribution*. Vol. 14.

41. Namani, Ravi, Yoram Lanir, Lik Chuan Lee, and Ghassan S. Kassab. 2020. "Overview of Mathematical Modeling of Myocardial Blood Flow Regulation." *American Journal of Physiology. Heart and Circulatory Physiology* 318 (4): H966-H975. doi:10.1152/ajpheart.00563.2019. https://www.ncbi.nlm.nih.gov/pubmed/32142361.

42. Osol, George, Gerard Celia, Natalia Gokina, Carolyn Barron, Edward Chien, Maurizio Mandala, Leonid Luksha, and Karolina Kublickiene. 2008. "Placental Growth Factor is a Potent Vasodilator of Rat and Human Resistance Arteries." *American Journal of Physiology - Heart and Circulatory Physiology; Am J Physiol Heart Circ Physiol* 294 (3): 1381-1387. doi:10.1152/ajpheart.00922.2007.

43. Osol, George, Nga Ling Ko, and Maurizio Mandalà. 2019. *Plasticity of the Maternal Vasculature during Pregnancy*.

44. ———. *Plasticity of the Maternal Vasculature during Pregnancy*. doi:10.1146/annurev-physiol-020518-.

45. Osol, George and Maurizio Mandala. 2009. "Maternal Uterine Vascular Remodeling during Pregnancy." *Physiology; Physiology (Bethesda)* 24 (1): 58-71. doi:10.1152/physiol.00033.2008.

46. Palmer, Susan K., STACY Zamudio, CAROLYN Coffin, STEVE Parker, ELIZABETH Stamm, and LORNA G. Moore. 1992. "Quantitative Estimation of Human Uterine Artery Blood Flow and Pelvic Blood Flow Redistribution in Pregnancy." *Obstetrics and Gynecology (New York.1953); Obstet Gynecol* 80 (6): 1000-1006.

47. Pettersson, Mass Per. 2015. *Polynomial Chaos Methods for Hyperbolic Partial Differential Equations : Numerical Techniques for Fluid Dynamics Problems in the Presence of Uncertainties*, edited by Gianluca Iaccarino, Jan Nordström Cham : Springer. 2015.

48. Rai, Anshita and James C. Cross. 2014. *Development of the Hemochorial Maternal Vascular Spaces in the Placenta through Endothelial and Vasculogenic Mimicry*. Vol. 387 Elsevier BV. doi:10.1016/j.ydbio.2014.01.015.

49. Roberts, V. H. J., T. K. Morgan, P. Bednarek, M. Morita, G. J. Burton, J. O. Lo, and A. E. Frias. 2017. *Early First Trimester Uteroplacental Flow and the Progressive Disintegration of Spiral Artery Plugs: New Insights from Contrast-Enhanced Ultrasound and Tissue Histopathology*. Vol. 32 Oxford University Press (OUP). doi:10.1093/humrep/dex301.

50. Rupnow, Heidi L., Terrance M. Phernetton, Cynthia E. Shaw, Mary L. Modrick, Ian M. Bird, and Ronald R. Magness. 2001. "Endothelial Vasodilator Production by Uterine and Systemic Arteries. VII. Estrogen and Progesterone Effects on eNOS." *American Journal of Physiology - Heart and Circulatory Physiology; Am J Physiol Heart Circ Physiol* 280 (4): 1699-1705. doi:10.1152/ajpheart.2001.280.4.H1699.

51. Saghian, Rojan, Gib Bogle, Joanna L. James, and Alys R. Clark. 2019. *Establishment of Maternal Blood Supply to the Placenta: Insights into Plugging, Unplugging and Trophoblast Behaviour from an Agent-Based Model*. doi:10.6084/m9.

52. Saghian, Rojan, Joanna L. James, Merryn H. Tawhai, Sally L. Collins, and Alys R. Clark. 2017. "Association of Placental Jets and Mega-Jets with Reduced Villous Density." *Journal of Biomechanical Engineering* 139 (5). doi:10.1115/1.4036145. http://dx.doi.org/10.1115/1.4036145.

53. Schaaps, Jean-Pierre, Vassilis Tsatsaris, Frederic Goffin, Jean-François Brichant, Katty Delbecque, Malek Tebache, Laurent Collignon, Maria Christina Retz, and Jean-Michel Foidart. 2005. "Shunting the Intervillous Space: New Concepts in Human Uteroplacental Vascularization." *American Journal of Obstetrics and Gynecology* 192 (1): 323-332. doi:10.1016/j.ajog.2004.06.066. https://dx.doi.org/10.1016/j.ajog.2004.06.066.

54. Schnauer, Laura. 2021. "Make Womb, an Investigation of Vascular Adaptation to Pregnancy."The University of Auckland.

55. Soares, M. J., D. Chakraborty, M. A. Karim Rumi, T. Konno, and S. J. Renaud. 2011. "Rat Placentation: An Experimental Model for Investigating the Hemochorial Maternal-Fetal Interface." *Placenta (Eastbourne); Placenta* 33 (4): 233-243. doi:10.1016/j.placenta.2011.11.026.

56. Sørensen, A., D. Peters, E. Fründ, G. Lingman, O. Christiansen, and N. Uldbjerg. 2013. "Changes in Human Placental Oxygenation during Maternal Hyperoxia Estimated by Blood Oxygen Level-dependent Magnetic Resonance Imaging (BOLD MRI)." *Ultrasound in Obstetrics & Gynecology; Ultrasound Obstet Gynecol* 42 (3): 310-314. doi:10.1002/uog.12395.

57. Talbert, D. G. 1995. "Uterine Flow Velocity Waveform Shape as an Indicator of Maternal and Placental Development Failure Mechanisms: A Model-based Synthesizing Approach." *Ultrasound in Obstetrics & Gynecology; Ultrasound Obstet Gynecol* 6 (4): 261-271. doi:10.1046/j.1469-0705.1995.06040261.x.

58. Tuma, Ronald, Walter Durán, and Klaus Ley. 2008. *Microcirculation*. 2nd ed.. ed. Amsterdam; Boston: Amsterdam; Boston : Elsevier/Academic Press 2008.

59. Williams, Mandy, Sue Turner, Emily Butler, and Jason Gardosi. 2018. *Fetal Growth Surveillance – Current Guidelines, Practices and Challenges*. Vol. 26 SAGE Publications. doi:10.1177/1742271x18760657.

60. World Health Organization. 2011. *WHO Recommendations for Prevention and Treatment of Pre-Eclampsia and Eclampsia* Geneva : World Health Organization. http://www.who.int/iris/handle/10665/44703.

61. Zhang, X-Y, M. N. Trame, L. J. Lesko, and S. Schmidt. 2015. "Sobol Sensitivity Analysis: A Tool to Guide the Development and Evaluation of Systems Pharmacology Models." *CPT: Pharmacometrics and Systems Pharmacology; CPT Pharmacometrics Syst Pharmacol* 4 (2): 69-79. doi:10.1002/psp4.6.

Appendix A: Channel Function Mathematical Proof

The following proof was based on principles outlined by Khaled at el. (Khaled and Vafai 2003).

Consider a clear central channel, radius $r = r_1$ with a porous medium surrounding it to have total tube radius $r = r_2$. The governing equations for blood flow velocity in tube are

$$(1) \qquad \frac{1}{r}\frac{\partial}{\partial r}\left(r\frac{\partial v_1}{\partial r}\right) = \frac{1}{\mu}\frac{\partial p}{\partial x} \ , \quad ,0 < r < r_1$$

$$(2) \qquad \frac{1}{r}\frac{\partial}{\partial r}\left(r\frac{\partial v_2}{\partial r}\right) - \frac{\mu}{k\mu'}v_2 = \frac{1}{\mu'}\frac{\partial p}{\partial x} \ , \quad ,r_1 < r < r_2$$

where r is the coordinate in the radial direction, x is the coordinate in the axial direction, v_1 are velocities in each portion of the tube, p is pressure, μ is viscosity, μ' is an effective viscosity, K is permeability of the porous medium.

Assuming that $\frac{\partial p}{\partial x}$ is linear, and $\frac{\partial p}{\partial x} = -\frac{\Delta p}{L}$.

Solve

$$(3) \qquad \frac{1}{r}\frac{\partial}{\partial r}\left(r\frac{\partial v_1}{\partial r}\right) = \frac{1}{\mu}\frac{\Delta p}{L} \ , \quad ,0 < r < r_1$$

$$(4) \qquad \frac{1}{r}\frac{\partial}{\partial r}\left(r\frac{\partial v_2}{\partial r}\right) - \frac{\mu}{k\mu'}v_2 = \frac{1}{\mu'}\frac{\Delta p}{L} \ , \quad ,r_1 < r < r_2.$$

These equations are subject to boundary conditions:

1) finite velocity at $r = 0$,
2) no slip (zero velocity) at $r = r_2$, and
3) continuity of velocity and shear (1st derivative of velocity) at $r = r_1$.

1. Solving Equation 3

Let $\alpha = \frac{1}{\mu}\frac{\Delta p}{L}$

$$(5) \qquad \frac{1}{r}\frac{\partial}{\partial r}\left(r\frac{\partial v_1}{\partial r}\right) = -\alpha \ , \quad ,0 < r < r_1$$

$$(6) \qquad \frac{\partial}{\partial r}\left(r\frac{\partial v_1}{\partial r}\right) = -r\alpha \ ,$$

$$(7) \qquad r\frac{\partial v_1}{\partial r} = \left(\frac{r^2}{2}\right)\alpha + c_1 \ ,$$

$$(8) \qquad \frac{\partial v^1}{\partial r} = -\frac{r}{2}\alpha + \frac{c_1}{r} \ ,$$

$$(9) \qquad v_1 = -\frac{r^2}{4}\alpha + c_1\ln(r) + c_2 \ .$$

Then, apply the condition that velocity needs to be finite.

at $r = 0$ and set $c1 = 0$ so,

$$(10) \qquad v_1 = -\frac{r^2}{4}\alpha + c_2 \ .$$

2. Solving Equation 4

Let $\beta = 1\,\Delta p$, $\gamma = \frac{\mu}{\mu'}$ and $\delta = \frac{\gamma}{k}$ such that

$$\frac{1}{r}\frac{\partial}{\partial r}\left(r\frac{\partial v_2}{\partial r}\right) - \delta v_2 + \beta = 0\,, \tag{11}$$

Note that $\beta = \gamma\alpha$, and $\beta/\delta = k\alpha$

$$\frac{1}{r}\left(\frac{\partial v_2}{\partial r} + r\frac{\partial^2 v_2}{\partial r}\right) - \delta v_2 + \beta = 0\,, \tag{12}$$

$$\frac{\partial^2 v_2}{\partial r^2}\left(\frac{1}{r}\frac{\partial v_2}{\partial r}\right) - \delta v_2 + \beta = 0\,, \tag{13}$$

The solution to this equation is,

$$v_2(r) = c_3 I_0\left(\sqrt{\delta r}\right) + c_4 K_0\left(\sqrt{\delta} r\right) + \frac{\beta}{\delta}, \tag{14}$$

where I_0 and K_0 are the modified Bessel functions of zeroth order of first and second kind, respectively.

Note that K_0 is infinite at $r = 0$.

Recalling that $\beta/\delta = k\alpha$,

$$v_2(r) = c_3 I_0\left(\sqrt{\delta r}\right) + c_4 K_0\left(\sqrt{\delta} r\right) + k\alpha, \tag{15}$$

3. Applying Boundary Conditions

First, apply no-slip at $r = r_2$.

$$c_3 I_0\left(\sqrt{\delta r_2}\right) + c_4 K_0\left(\sqrt{\delta} r_2\right) = -k\alpha, \tag{16}$$

Next, continuity of velocity at $r = r_1$.

$$-\frac{r_1^2}{4}\alpha + c_2 = c_3 I_0\left(\sqrt{\delta r_1}\right) + c_4 K_0\left(\sqrt{\delta} r_1\right) + k\alpha, \tag{17}$$

Finally, continuity of first derivative of velocity at $r = r_1$.

$$c_3\left(\sqrt{\delta I_1}\right)\left(\sqrt{\delta r_1}\right) - c_4\sqrt{\delta K_1}\left(\sqrt{\delta} r_1\right) = -\frac{r_1}{2}\alpha, \tag{18}$$

Note these Bessel functions are now first order.

Rearranging equation 16,

$$\frac{c_3 I_0\left(\sqrt{\delta r_2}\right)}{K_0\left(\sqrt{\delta r_2}\right)} + c_4 = +k\alpha\frac{1}{K_0(\sqrt{\delta r_2}}\ , \tag{19}$$

And equation 18,

$$\frac{c_3\ I_1\left(\sqrt{\delta I_2}\right)}{K_0\left(\sqrt{\delta r_2}\right)} - c_4 = -\frac{r_1}{2}\alpha\frac{1}{\sqrt{\delta K_1}\left(\sqrt{\delta} r_1\right)}\,, \tag{20}$$

Adding these two equations together gives,

$$\frac{c_3(I_1\sqrt{\delta I}_1)}{K_1(\sqrt{\delta r_1})}+\frac{I_0(\sqrt{\delta}r_2)}{K_0(\sqrt{\delta}r_2)}=\frac{k\alpha 1}{K_0(\sqrt{\delta r_2})}-\frac{r}{2}\alpha\frac{1}{\sqrt{\delta K_1(\sqrt{\delta r_1})}}\ , \tag{21}$$

And

$$c_3=\frac{-k\alpha\frac{1}{K_0(\sqrt{\delta r_2})}-\frac{r_1}{2}\alpha\frac{1}{\sqrt{\delta K_1}(\sqrt{\delta}r_1)}}{\left(\frac{I_1(\sqrt{\delta}r_1)}{K_1(\sqrt{\delta}r_1)}+\frac{I_0(\sqrt{\delta}r_2)}{K_0(\sqrt{\delta}r_2)}\right)}\ , \tag{22}$$

$$c_3=\alpha\frac{(-k\frac{1}{K_0(\sqrt{\delta r_2})}-\frac{r_1}{2}\alpha\frac{1}{\sqrt{\delta K_1}(\sqrt{\delta}r_1)})}{\left(\frac{I_1(\sqrt{\delta}r_1)}{K_1(\sqrt{\delta}r_1)}+\frac{I_0(\sqrt{\delta}r_2)}{K_0(\sqrt{\delta}r_2)}\right)}\ , \tag{23}$$

$$c_3=\frac{\alpha}{2\sqrt{\delta}}\frac{(\frac{-k2\sqrt{\delta}}{K_0(\sqrt{\delta r_2})}-\frac{r_1}{K_1(\sqrt{\delta}r_1)})}{\left(\frac{I_1(\sqrt{\delta}r_1)}{K_1(\sqrt{\delta}r_1)}+\frac{I_0(\sqrt{\delta}r_2)}{K_0(\sqrt{\delta}r_2)}\right)}, \tag{24}$$

$$c_3=\frac{\alpha}{2\sqrt{\delta}}\frac{(-2k\sqrt{\delta K_1}(\sqrt{\delta r_1})-r_1K_0(\sqrt{\delta r_2})}{(K_0(\sqrt{\delta r_2})I_1(\sqrt{\delta r_1})+K_1(\sqrt{\delta r_1})I_0(\sqrt{\delta r_2}))}\ . \tag{25}$$

Substituting this definition for c_3 into equation 16 to gives a definition for c_4.

$$c_4K_0(\sqrt{\delta r_2})=-k\alpha-c_3I_0(\sqrt{\delta r_2})\ , \tag{26}$$

$$c_4K_0(\sqrt{\delta r_2})=-k\alpha-\frac{\alpha}{2\sqrt{\delta}}\frac{(-2k\sqrt{\delta K_1}(\sqrt{\delta r_1})-r_1K_0(\sqrt{\delta r_2})}{\left(K_0(\sqrt{\delta r_2})I_1(\sqrt{\delta r_1})+K_1(\sqrt{\delta r_1})I_0(\sqrt{\delta r_2})\right)}\ I_0(\sqrt{\delta r_2}) \tag{27}$$

$$c_4K_0(\sqrt{\delta r_2})=-\frac{\alpha}{2\sqrt{\delta}}\left[2\sqrt{\delta k}\frac{(-2k\sqrt{\delta K_1}(\sqrt{\delta r_1})-r_1K_0(\sqrt{\delta r_2})}{\left(K_0(\sqrt{\delta r_2})I_1(\sqrt{\delta r_1})+K_1(\sqrt{\delta r_1})I_0(\sqrt{\delta r_2})\right)}\ I_0(\sqrt{\delta r_2})\right] \tag{28}$$

$$c_4K_0(\sqrt{\delta r_2})=-\frac{\alpha}{2\sqrt{\delta}}\left[\frac{2\sqrt{\delta k}\left(K_0(\sqrt{\delta r_2})I_1(\sqrt{\delta r_1})+K_1(\sqrt{\delta r_1})I_0(\sqrt{\delta r_2})\right)+\left(-2k\sqrt{\delta K_1}(\sqrt{\delta r_1})-r_1K_0(\sqrt{\delta r_2})\right)}{\left(K_0(\sqrt{\delta r_2})I_1(\sqrt{\delta r_1})+K_1(\sqrt{\delta r_1})I_0(\sqrt{\delta r_2})\right)}\right] \tag{29}$$

$$c_4K_0(\sqrt{\delta r_2})=-\frac{\alpha}{2\sqrt{\delta}}\left[\frac{2\sqrt{\delta k}K_0(\sqrt{\delta r_2})I_1(\sqrt{\delta r_1})-r_1K_0(\sqrt{\delta r_2})I_0(\sqrt{\delta r_2})}{\left(K_0(\sqrt{\delta r_2})I_1(\sqrt{\delta r_1})+K_1(\sqrt{\delta r_1})I_0(\sqrt{\delta r_2})\right)}\right] \tag{30}$$

$$c_4=-\frac{\alpha}{2\sqrt{\delta}}\left[\frac{2\sqrt{\delta k}I_1(\sqrt{\delta r_1})-r_1K_0(\sqrt{\delta r_2})I_0(\sqrt{\delta r_2})}{\left(K_0(\sqrt{\delta r_2})I_1(\sqrt{\delta r_1})+K_1(\sqrt{\delta r_1})I_0(\sqrt{\delta r_2})\right)}\right] \tag{31}$$

and then into equation (17) to get c_2.

$$c_2=-\frac{\alpha}{2\sqrt{\delta}}\left[\frac{2k\sqrt{\delta}K_1(\sqrt{\delta r_1})-r_1K_0(\sqrt{\delta r_2})I_0(\sqrt{\delta r_1})}{\left(K_0(\sqrt{\delta r_2})I_1(\sqrt{\delta r_1})+K_1(\sqrt{\delta r_1})I_0(\sqrt{\delta r_2})\right)}\right]-\frac{\alpha}{2\sqrt{\delta}}\left[\frac{2\sqrt{\delta k}I_1(\sqrt{\delta r_1})-r_1I_0(\sqrt{\delta r_2})K_0(\sqrt{\delta r_1})}{\left(K_0(\sqrt{\delta r_2})I_1(\sqrt{\delta r_1})+K_1(\sqrt{\delta r_1})I_0(\sqrt{\delta r_2})\right)}\right]+ k\propto+\frac{r_1^2}{4}\propto \tag{32}$$

$$v_1=\ -\frac{r^2}{4}\alpha+c_2\ . \tag{33}$$

$$v_2=\ \alpha(\ \bar{c}\ I_0(\sqrt{\delta r})+\overline{c_4}K_0(\sqrt{\delta r})+k \tag{34}$$

With,

$$\overline{c_2}=\frac{1}{2\sqrt{\delta}}\left[\frac{-2k\sqrt{\delta}K_1(\sqrt{\delta r_1})-r_1K_0(\sqrt{\delta r_2})I_0(\sqrt{\delta r_1})}{\left(K_0(\sqrt{\delta r_2})I_1(\sqrt{\delta r_1})+K_1(\sqrt{\delta r_1})I_0(\sqrt{\delta r_2})\right)}\right]-\frac{1}{2\sqrt{\delta}}\left[\frac{2\sqrt{\delta k}I_1(\sqrt{\delta r_1})-r_1I_0(\sqrt{\delta r_2})K_0(\sqrt{\delta r_1})}{\left(K_0(\sqrt{\delta r_2})I_1(\sqrt{\delta r_1})+K_1(\sqrt{\delta r_1})I_0(\sqrt{\delta r_2})\right)}\right]+ k+\frac{r_1^2}{4} \tag{35}$$

$$\overline{c_3}=\frac{1}{2\sqrt{\delta}}\frac{(-2k\sqrt{\delta K_1}(\sqrt{\delta r_1})-r_1K_0(\sqrt{\delta r_2})}{(K_0(\sqrt{\delta r_2})I_1(\sqrt{\delta r_1})+K_1(\sqrt{\delta r_1})I_0(\sqrt{\delta r_2}))} \tag{36}$$

$$\overline{c_4}=-\frac{1}{2\sqrt{\delta}}\left[\frac{2\sqrt{\delta k}I_1(\sqrt{\delta r_1})-r_1K_0(\sqrt{\delta r_2})I_0(\sqrt{\delta r_2})}{\left(K_0(\sqrt{\delta r_2})I_1(\sqrt{\delta r_1})+K_1(\sqrt{\delta r_1})I_0(\sqrt{\delta r_2})\right)}\right] \tag{37}$$

4. Flow in clear channel

Flow in the clear channel is defined as

$$Q_1 = 2\pi\int_0^{r_1} rv_1(r)dr = 2\pi\alpha\int_0^{r_1} r\left(-\frac{r^2}{4}+\overline{c_2}\right)dr\,. \tag{38}$$

$$Q_1 = 2\pi\alpha\int_0^{r_1} -\frac{r^3}{4}+\overline{c_2}rdr \tag{39}$$

$$Q_1 = 2\pi\alpha\left[-\frac{r^4}{16}+\overline{c_2}\frac{r^2}{2}\right]_0^{r_1} \tag{40}$$

$$Q_1 = 2\pi\alpha\left(-\frac{r_1^4}{16}+\overline{c_2}\frac{r_1^2}{2}\right) \tag{41}$$

$$Q_1 = \frac{2\pi\Delta p}{\mu L}\left(\overline{c_2}\frac{r_1^2}{2}-\frac{r_1^4}{16}\right) \tag{42}$$

c_2 is known so Q_1 can be calculated.

5. Flow in porous surrounds

Flow in the porous surrounds is

$$Q_2 = 2\pi\int_0^{r_1} rv_2(r)dr = 2\pi\alpha\int_{r_1}^{r_2} r\left(\overline{c_3}I_0(\sqrt{\delta r})+\overline{c_4}K_0(\sqrt{\delta r})+k\right)dr\,. \tag{43}$$

$$Q_2 = 2\pi\alpha\left[\frac{\overline{c_3}rI_1(\sqrt{\delta r})}{\sqrt{\delta}}-\frac{\overline{c_4}rK_1(\sqrt{\delta r})}{\sqrt{\delta}}+k\frac{r^2}{2}\right]_{r_1}^{r_2} \tag{44}$$

$$Q_2 = \frac{2\pi\Delta p}{\sqrt{\delta}\mu L}\left(\overline{c_3}\left(r_2I_1(\sqrt{\delta r_2})-r_1I_1(\sqrt{\delta r_1})\right)-\overline{c_4}(r_2K_1\sqrt{\delta r_2})-r_1K_1(\sqrt{\delta r_1})+k\frac{r_2^2-r_1^2}{2}\right) \tag{45}$$

6. Total flow and resistance

The total flow through the tube $(Q_T\ )$ is

$$QT = Q1 + Q2, \tag{46}$$

and resistance is

$$R = \frac{\Delta P}{Q_1+Q_2}=\frac{1}{\bar{Q}_1+\bar{Q}_2} \tag{47}$$

Where,

$$\bar{Q}_1 = \frac{2\pi}{\mu L}\left(\bar{c}_2\frac{r_1^2}{2}-\frac{r_1^4}{16}\right) \tag{48}$$

and

(49) $$\bar{Q}_2 = \frac{2\pi}{\mu L}\Big(\bar{c}_3 \Big(r_2 I_1(\sqrt{\delta r_2}) - r_1 I_1(\sqrt{\delta r_1})\Big) - \bar{c}_4(r_2 K_1\sqrt{\delta r_2}) - r_1 K_1(\sqrt{\delta r_1}) + k\,\frac{r_2^2 - r_1^2}{2}\Big)$$

with

(50) $$\bar{c}_2 = \frac{1}{2\sqrt{\delta}}\left[\frac{-2k\sqrt{\delta}K_1(\sqrt{\delta r_1}) - r_1 K_0(\sqrt{\delta r_2}) I_0(\sqrt{\delta r_1})}{\big(K_0(\sqrt{\delta r_2}) I_1(\sqrt{\delta r_1}) + K_1(\sqrt{\delta r_1}) I_0(\sqrt{\delta r_2})\big)}\right] - \frac{1}{2\sqrt{\delta}}\left[\frac{2\sqrt{\delta k} I_1(\sqrt{\delta r_1}) - r_1 I_0(\sqrt{\delta r_2}) K_0(\sqrt{\delta r_1})}{\big(K_0(\sqrt{\delta r_2}) I_1(\sqrt{\delta r_1}) + K_1(\sqrt{\delta r_1}) I_0(\sqrt{\delta r_2})\big)}\right] + k + \frac{r_1^2}{4}$$

(51) $$\bar{c}_3 = \frac{1}{2\sqrt{\delta}} \frac{(-2k\sqrt{\delta K_1}(\sqrt{\delta r_1}) - r_1 K_0(\sqrt{\delta r_2})}{(K_0(\sqrt{\delta r_2}) I_1(\sqrt{\delta r_1}) + K_1(\sqrt{\delta r_1}) I_0(\sqrt{\delta r_2}))}$$

(52) $$\bar{c}_4 = -\frac{1}{2\sqrt{\delta}}\left[\frac{2\sqrt{\delta k} I_1(\sqrt{\delta r_1}) - r_1 K_0(\sqrt{\delta r_2}) I_0(\sqrt{\delta r_2})}{\big(K_0(\sqrt{\delta r_2}) I_1(\sqrt{\delta r_1}) + K_1(\sqrt{\delta r_1}) I_0(\sqrt{\delta r_2})\big)}\right]$$

Letting ϵ be the porosity of the porous medium, and Dp be trophoblast diameter then

(53) $$k = \frac{D_p^2 \epsilon^3}{180(1-\epsilon)^2}$$

and

(54) $$\gamma = \frac{1}{1 + 2.5(1-\varepsilon)}$$